AD-A284 257

KINETIC MODELS
OF
SOOT FORMATION

Final Technical Report

June 1991 to May 1994

DTIC
S ELECTE D
SEP 07 1994
F

Prepared by
M. B. Colket, III,
R. J. Hall,
and
M. D. Smooke

United Technologies Research Center
East Hartford, CT 06108

UTRC Report No. UTRC94-28

94-29079

For
Air Force Office of Scientific Research
Bolling Air Force Base
Washington, D. C. 20332

Contract No. F49620-91-C-0056

Reproduced From
Best Available Copy

J. M. Tishkoff
Program Manager
July 20, 1994

This document has been approved
for public release and sale; its
distribution is unlimited.

DTIC QUALITY INSPECTED 3

MECHANISTIC MODELS
OF
SOOT FORMATION

Final Technical Report

June 1991 to May 1994

Prepared by
M. B. Colket, III,
R. J. Hall,
and
M. D. Smooke

United Technologies Research Center
East Hartford, CT 06108

UTRC Report No. UTRC94-28

For
Air Force Office of Scientific Research
Bolling Air Force Base
Washington, D. C. 20332

Contract No. F49620-91-C-0056

J. M. Tishkoff
Program Manager
July 20, 1994

Accesion For
NTIS CRA&I ☑
DTIC TAB ☐
Unannounced ☐
Justification ....
By ....
Distribution /
Availability Codes

Dist	Avail and / or Special
A-1	

DTIC QUALITY INSPECTED 3

UTRC 94-28

MECHANISTIC MODELS OF SOOT FORMATION

Final Technical Report

Table of Contents

LIST OF TABLES iii

LIST OF FIGURES iii

SUMMARY 1

I. INTRODUCTION 1

II. RESULTS 2

A. Kinetics of Toluene Pyrolysis. 2

B. Soot Formation Modeling in Diffusion Flames 8

III. LIST OF PUBLICATIONS 13

IV. MEETING INTERACTIONS AND PRESENTATIONS 13

V. RECORD OF INVENTIONS 13

VI. REFERENCES 14

Appendix A. Reaction Mechanisms for Toluene Pyrolysis A-1

Appendix B. Predictions of Soot Dynamics in Opposed Jet Diffusion Flames B-1

Appendix C. Radiative Dissipation in Planar Gas-Soot Mixtures C-1

Appendix D. Modeling of Soot Aerosol Formation in Opposed Jet Diffusion Flame (abstract) D-1

Appendix E. Predictions of Soot Formation in Counterflow Diffusion Flames (abstract) E-1

List of Figures

1. Diagram of Integrated Soot Formation Model and Flame Code 9
2. Configuration of Opposed-Jet, Laminar, Diffusion Flame 10
3. Predictions of Soot Production with Spatial Evolution of Size Classes 11
4. Experimental Soot Distributions in Opposed-Jet Methane Flame 12

List of Tables

1. Proposed Mechanism for Toluene Pyrolysis 3
2. Thermodynamic Properties of Selected Species 6

UTRC 94-28

MECHANISTIC MODELS OF SOOT FORMATION

Final Technical Report

SUMMARY

The overall objectives of this work are to (1) refine and update an existing soot formation model and (2) incorporate this soot model into a code describing a laminar, opposed-jet diffusion flame. In the third year of this contract, a detailed chemical kinetic mechanism for the pyrolysis of toluene and the formation of polyaromatic hydrocarbons has been developed. This chemical kinetic model is consistent with shock tube data with mass spectral identification of intermediate species. These data were obtained in the first year of this program. This kinetic analysis provides a better understanding of how aromatic rings decompose and how polyaromatic species grow. In a related effort, the previously developed soot formation code, based on a sectional aerosol model for predicting soot inception, growth, and oxidation in a premixed flame has been fully integrated into an opposed-jet, diffusion flame code. The new code includes effects due to radiation from both gaseous species and particulates as well as scavenging of species by soot. The code treats particle transport including thermophoresis. Predictions from a low strain rate, lightly-sooting, methane-fueled, opposed-jet, diffusion flame are included in this report. Perturbation studies demonstrate the importance of fully integrating soot production, radiation, and scavenging in order to reasonably predict bulk parameters such as temperature as well as species concentrations, sooting levels, and radiation loads.

I. Introduction

The overall goal of this three year effort is to incorporate a soot model into a code for a laminar, opposed-jet, diffusion flame. Specific objectives necessary to reach this goal are: (1) identify reduced kinetic mechanisms which adequately describe ring formation and growth processes, (2) obtain and interpret new data on polyaromatic hydrocarbons (PAH) formed during hydrocarbon pyrolysis, (3) refine and update an existing soot formation model, (4) incorporate a radiation model into a code describing a laminar, opposed-jet diffusion flame, and (5) incorporate the soot model into the flame code. In the annual reports for the first two years of this program [1,2], results and progress related to much of the above were discussed. In particular, (1) a simplified kinetic sequence describing the dominant paths for benzene formation and destruction was developed and verified by comparison to experiment, (2) new experimental data on toluene pyrolysis were obtained with a focus on the identification of key intermediate species via mass spectrometry, (3) temperature-dependent thermodynamic parameters were determined for many intermediate hydrocarbon species and those for PAHs were obtained from the literature or calculated using known correlations, (4) the soot formation code for a premixed flame was modified to include effects due to soot aging, (5) a band radiation model was developed to treat radiation from flames with varying degrees of optical thickness, (6) predictions from the sectional model for soot formation were compared with predictions from global soot formation models and limitations of these global models were identified, and (7) the sectional soot formation model was added to the opposed jet diffusion flame code, although debugging of the combined codes was incomplete.

In this final report, these efforts are summarized by a manuscript describing a detailed chemical kinetic mechanism for toluene pyrolytic decay and PAH formation and a paper specifying the combined soot formation and diffusion flame codes. These manuscripts are mostly self-explanatory so only some of the highlights are reviewed here. In the case of the toluene paper, however, some details on the chemical kinetic mechanism and thermodynamic data could not be included in the publication due to space limitations; consequently, this information is included here for completeness.

II. Results

II. A. Kinetics of Toluene Pyrolysis

Reaction mechanisms and kinetics for toluene decomposition and PAH formation are proposed based on literature results and new experimental data obtained from the single-pulse shock tube (SPST). These results are described in Appendix A of this report. The detailed reaction mechanism is reproduced in Table 1 and the thermodynamic data required for the kinetic estimations and calculations of reverse reaction rates are provided in Table 2.

Key results from this study are the identification of a low energy path for the decomposition of benzyl radical based on product distribution, theoretical arguments, and evidence obtained by shock heating similar chemical systems, specifically cyclopentadiene, norbornadiene, and mixtures of cyclopentadiene and acetylene. The stability of benzyl, an aromatic radical, is resonantly enhanced and the products of its decomposition have eluded researchers for many years. Evidence for and specifics of this new proposal are reviewed here.

Two low temperature products observed during toluene pyrolysis coincident with early formation of acetylene (presumably a decomposition product of benzyl or phenyl) are cyclopentadiene (cpd) and benzyl-cyclopentadienyl (b-cpd). The latter product is almost entirely formed during the quenching process via the recombination of the two stable radicals, benzyl and cyclopentadienyl. Traces of several other C_5 species at masses 66 and 68 were observed at levels typically 5 to 10 times below those of cpd. The presence of the C_5 compounds supports arguments for decomposition of benzyl radical into a C_5-species. Cpd is preferred since cyclopentadienyl offers the lowest energy path for

TABLE 1
PROPOSED MECHANISM FOR TOLUENE PYROLYSIS
log k = log A- E/R/T/2.303, units: cc- mole- sec- kcal

Reactions	Forward Rate Constant		Reverse Rate Constant	
	Log A	**E**	**Log A**	**E**
1 C_7H_8=benzyl+H	15.45	88.9	14.24	-0.2
2 C_7H_8=phenyl+CH_3	16.00	97.0	12.92	-0.8
3 C_7H_8+H=benzyl+H_2	14.10	8.4	13.50	23.7
4 C_7H_8+CH_3=CH_4+benzyl	12.20	11.1	13.08	27.1
5 C_6H_6=phenyl+H	16.76	116.0	14.46	6.4
6 C_6H_6+H=phenyl+H_2	14.40	16.0	12.71	10.7
7 C_6H_6+CH_3=phenyl+CH_4	13.30	16.0	13.10	11.5
8 C_7H_8+H=C_6H_6+CH_3	13.08	5.1	12.30	17.0
9 2benzyl=bibenzyl	12.70	0.5	14.93	60.0
10 H+bibenzyl→stilbene+H_2+H	13.70	5.0	0.00	0.0
11 H+bibenzyl→C_8H_8+phenyl+H_2	13.70	13.0	0.00	0.0
12 stilbene+H→phenanthrene+H_2+H	14.40	16.0	0.00	0.0
13 stilbene+CH_3→phenanthrene+CH_4+H	13.30	16.0	0.00	0.0
14 stilbene=phenanthrene+H_2	8.00	40.0	8.37	45.5
15 2phenyl=$C_{12}H_{10}$	12.50	0.0	15.96	107.5
16 phenyl+C_6H_6=$C_{12}H_{10}$+H	12.00	7.0	13.16	4.8
17 C_2H_2+phenyl=$C_6H_5C_2H$+H	12.00	5.0	13.81	6.6
18 $C_{12}H_{10}$+H=$C_{12}H_9$+H_2	14.40	16.0	13.04	10.5
19 $C_{12}H_9$+C_2H_2=phenanthrene+H	12.30	5.0	16.42	55.8
20 phenyl+C_7H_8=DPM+H	11.70	7.0	11.80	8.2
21 DPM+H→fluorene+H+H_2	14.40	16.0	0.00	0.0
22 DPM=fluorene+H_2	8.00	32.0	10.24	18.3
23 fluorene+CH_3→anthracene+H_2+H	12.30	17.0	0.00	0.0
24 benzyl+C_7H_8=DMDP+H	12.48	28.0	12.19	3.3
25 benzyl+C_7H_8=DMDP1+H	12.30	28.0	12.02	3.3
26 DMDP1+H→dhanthracene+H+H_2	14.00	7.0	0.00	0.0
27 DMDP1=dhanthracene+H_2	8.00	40.0	9.67	10.7
28 dhanthracene=anthracene+H_2	12.36	43.8	12.02	52.2
29 anthracene=phenanthrene	12.90	65.0	12.73	67.0
30 phenanthrene+H=phenanthrenyl+H_2	14.40	16.0	13.45	11.3
31 phenanthrenyl+C_2H_2→pyrene+H	12.00	5.0	0.00	0.0
32 phenyl+$C_6H_5C_2H$→phenanthrene+H	12.00	5.0	0.00	0.0

TABLE 1 (continued)
PROPOSED MECHANISM FOR TOLUENE PYROLYSIS
log k = log A- E/R/T/2.303, units: cc- mole- sec- kcal

Reactions	Forward Rate Constant		Reverse Rate Constant	
	Log A	E	Log A	E
33 $C_6H_4C_2H+C_6H_5C_2H \rightarrow$pyrene+H	11.00	5.0	0.00	0.0
34 $H+C_7H_8=CH_3C_6H_4+H_2$	14.00	16.0	12.22	9.7
35 $CH_3C_6H_4$+benzyl=DMDP	12.18	0.0	14.29	86.0
36 H+DMDP=DPM+CH_3	13.08	5.1	11.60	22.4
37 $CH_3C_6H_4$+benzyl=DMDP1	12.18	0.0	14.29	86.0
38 $CH_3C_6H_4+C_7H_8$=DMDP+H	11.30	7.0	12.20	3.9
39 $C_7H_8+CH_3=CH_3C_6H_4+CH_4$	13.00	16.0	12.70	10.4
40 $CH_3C_6H_4+C_7H_8$=DMDP1+H	11.18	7.0	12.08	3.9
41 $CH_3C_6H_4+C_7H_8$=benzyl+C_7H_8	11.48	3.0	12.66	24.6
42 $CH_3C_6H_4+C_2H_2 \rightarrow$indene+H	12.00	5.0	0.00	0.0
43 indene+$CH_3 \rightarrow$naphthalene+H_2+H	12.30	17.00	0.00	0.0
44 phenyl+$C_7H_8=C_6H_6$+benzyl	12.20	11.1	13.29	31.7
45 $CH_3+C_7H_8$=xylene+H	11.31	17.0	12.91	4.3
46 $CH_3+CH_3C_6H_4$=xylene	13.30	0.0	17.30	98.0
47 benzyl+$CH_3=C_8H_{10}$	12.70	0.0	15.00	73.4
48 benzyl=c-$C_5H_5+C_2H_2$	13.78	70.0	11.57	8.3
49 benzyl=$C_4H_4+C_3H_3$	14.30	83.6	8.28	-15.6
50 phenyl=$C_4H_3+C_2H_2$	13.65	72.5	7.79	-25.8
51 $CH_3C_6H_4=C_4H_3+C_3H_4$	13.65	72.5	8.38	-22.1
52 C_3H_3+benzyl=naphthalene+2H	11.78	0.0	0.0	0.0
53 benzyl+c-C_5H_5=b-cpd	12.70	0.0	13.81	49.3
54 benzyl+C_5H_6=b-cpd+H	11.70	30.0	11.87	-0.3
55 C_7H_8+c-C_5H_5=b-cpd+H	11.70	40.0	11.59	0.2
56 $H+C_8H_{10}=C_6H_6+C_2H_5$	13.08	5.1	12.14	20.1
57 $H+C_8H_{10} \rightarrow C_8H_8+H_2+H$	14.40	8.4	0.00	0.0
58 $H+C_8H_8 \rightarrow C_6H_5C_2H+H_2+H$	14.84	14.5	0.00	0.0
59 $C_6H_5C_2H+H=C_6H_4C_2H+H_2$	14.40	16.0	13.18	10.7
60 $C_6H_4C_2H+C_2H_2$=naphthalenyl	12.00	5.0	16.54	96.2
61 naphthalene+H=naphthalenyl+H_2	14.40	16.0	12.77	10.5
62 naphthalenyl+$C_2H_2 \rightarrow$acenaphthylene+H	12.48	5.0	0.00	0.0
63 naphthalenyl+$C_2H_2=C_{10}H_7C_2H$+H	12.00	5.0	13.81	6.6

TABLE 1 (continued)

PROPOSED MECHANISM FOR TOLUENE PYROLYSIS

log k = log A- E/R/T/2.303, units: cc- mole- sec- kcal

Reactions	Forward Rate Constant		Reverse Rate Constant	
	Log A	E	Log A	E
64 $C_{10}H_7C_2H+H=C_{10}H_6C_2H+H_2$	14.40	16.0	13.49	10.7
65 $C_{10}H_6C_2H+C_2H_2$=phenanthrenyl	12.00	5.0	16.54	98.4
66 naphthalenyl+C_6H_6→pyrene+H+H_2	12.00	5.0	0.00	0.0
67 naphthalene+phenyl→pyrene+H+H_2	11.00	5.0	0.00	0.0
68 $H+C_8H_8=C_6H_6+C_2H_3$	13.08	5.1	12.36	10.9
69 $2CH_3=C_2H_6$	13.00	0.0	16.26	87.5
70 $C_2H_3+C_7H_8=C_2H_4+C_7H_7$	12.60	8.0	13.31	23.8
71 $C_3H_5+C_2H_2=C_5H_7$	12.00	8.0	13.03	19.5
72 $C_5H_7=C_5H_6+H$	10.30	5.0	13.23	2.1
73 $C_5H_6=H+c\text{-}C_5H_5$	15.30	81.0	14.36	1.5
74 $2c\text{-}C_5H_5$=bicpdyl	12.70	0.0	13.30	39.1
75 $H+C_5H_6=l\text{-}C_5H_7$	12.00	0.0	10.02	34.3
76 $l\text{-}C_5H_7+C_5H_6=C_5H_8+c\text{-}C_5H_5$	12.70	6.0	12.88	6.7
77 $C_5H_8+H=C_2H_4+C_3H_5$	13.00	8.0	12.09	31.0
78 $H+C_5H_6=H_2+c\text{-}C_5H_5$	12.48	8.0	12.15	32.9
79 $H+C_5H_6=C_2H_2+C_3H_5$	13.00	12.0	9.04	3.4
80 $H+C_5H_6=C_2H_4+C_3H_3$	12.70	18.0	8.70	10.4
81 $c\text{-}C_5H_5=C_2H_2+C_3H_3$	15.00	71.0	9.75	-3.2
82 $2C_3H_3$→phenyl+H	13.00	0.0	0.00	0..0
83 $CH_3+C_5H_6=CH_4+c\text{-}C_5H_5$	12.70	5.0	13.86	30.6
84 $C_3H_5+C_7H_8=C_3H_6$+benzyl	12.70	14.0	12.65	11.6
85 $CH_3CHCH+C_7H_8=C_3H_6$+benzyl	12.20	11.0	13.08	30.0

TABLE 2

THERMODYNAMIC PROPERTIES OF SELECTED SPECIES

Name	ΔH°_f	S°	C_p (cal/mole/K)				
	kcal/mole	cal/mole/K	300K	500K	800K	1000K	1500K
Toluene	12.0	76.7	24.8	40.6	55.9	62.4	71.6
Benzyl	47.8	73.5	26.2	40.8	54.5	60.2	68.2
Methylphenyl	71.4	81.7	24.6	38.7	52.6	58.4	67.0
Ethylbenzene	70.7	86.1	30.8	49.3	67.1	74.8	85.9
Styrene	35.2	82.5	29.4	45.9	60.9	67.8	77.5
Xylene	43.6	84.3	30.2	48.5	67.3	75.5	84.8
Bibenzyl	34.3	113.5	49.3	79.8	108.1	120.1	136.6
Trans-stilbene	56.0	108.3	48.0	73.7	102.0	113.6	128.1
Dimethyldiphenyl*	30.5	121.3	48.0	77.9	106.8	119.4	137.4
Diphenylmethane**	33.0	112.3	42.4	70.3	96.5	107.6	123.5
Benzylcyclopentadienyl	52.4	101.8	41.7	70.2	95.1	105.1	119.6
Biphenyl	43.6	93.7	39.7	64.4	87.0	96.0	108.2
Naphthalene	36.0	79.5	31.8	52.0	70.6	78.6	90.0
Indene	39.1	80.7	29.6	48.2	66.1	73.4	84.0
Fluorene	47.0	91.4	40.1	67.6	92.2	101.8	115.0
Acenaphthylene	61.7	87.2	38.0	60.7	81.0	89.1	100.7
Dihydroanthracene	58.4	100.6	47.3	76.7	103.9	115.1	130.6
Anthracene	52.1	94.0	44.4	72.4	97.3	107.2	121.3
Phenanthrene	50.0	94.5	44.9	72.7	97.3	107.2	121.3
Pyrene	55.2	96.5	48.9	79.7	106.7	117.4	132.3

* DMDP and DMDP1
** DPM

decomposition (64 kcal/mole). The mechanism for this process has not been described well. Thus, we explored the reverse process by comparing results from cpd pyrolysis with those of cpd/C_2H_2 pyrolysis. The rate of toluene formation was enhanced by about an order of magnitude in the presence of acetylene. Following a suggestion by Kiefer, the toluene formation was then compared with the reverse of the known elimination of acetylene from norbornadiene (nbde). Nbde should be an intermediate in the conversion between toluene and cpd plus acetylene:

$$\text{c-}C_5H_6 + C_2H_2 \Leftrightarrow \text{nbde} \Leftrightarrow \text{toluene.}$$

Rate constants for the formation of toluene by the above process were calculated from the experimental data and were compared to literature values for the reverse process. After reducing the reverse rate by a factor of four to account for decomposition of nbde into the reactants and isomerization to cycloheptatriene, the extrapolated rate for the addition reaction is more than a factor of two below the experimental value. More importantly, the temperature dependence of the rate constant of the published value for the reverse process (25 kcal/mole) is significantly lower than our experimental value of nearly 60 kcal/mole. Alternatively, we may be observing the radical addition/isomerization:

$$\text{c-}C_5H_5 + C_2H_2 \Leftrightarrow \text{norbornadienyl} \Leftrightarrow \text{benzyl.}$$

The possibility of the reverse of this process has been suggested previously. Thus, the observed temperature dependence would be due principally to the temperature dependence of cpd decomposition and formation of cyclopentadienyl. The activation energy for the decomposition of benzyl into cyclopentadienyl as listed in Table 1 (70 kcal/mole) is based on low barriers for the bridging process to form norbornadienyl and subsequent acetylene elimination. During the toluene experiments, a trace peak (at mass 92) was observed which eluted near the retention time for nbde, but insufficient mass was recovered for positive identification. To provide some further confirmation of these types of processes, nbde was pyrolyzed in the SPST. Even at the lowest temperatures tested, near 1100K, only traces of nbde remained after pyrolysis, while the products cpd, toluene, cycloheptatriene, and acetylene were observed. The rapid loss of nbde was consistent with known rates for nbde isomerization/decomposition. It is difficult to extract information from this latter study with nbde to confirm the proposed benzyl radical decomposition pathway.

Nevertheless, Reaction 48 was adopted as the preferred low temperature benzyl decomposition path. An energy diagram for this process is provided in Fig. 5 of Appendix A. The cpd and b-cpd production were used to help determine a rate for benzyl radical decomposition. Unfortunately, a sensitivity analysis indicates that the concentrations of these species are dependent on both the rates for decomposition of benzyl (Reaction 48) and for cyclopentadienyl radicals (Reaction 81). The rates suggested in Table 1 for these two reactions should be considered accurate to about a factor of three in the temperature range of 1300 to 1500K.

Other key conclusions from the toluene paper include identification of several ring growth processes. A key step not well recognized previously are four-centered reactions causing ring closure and direct H_2 elimination. Pathways involving sequential acetylene addition to aromatic species are not fast enough to explain the observed formation rates of PAH. In addition, aromatic isomerization reactions were demonstrated with half-lives at 1600K near 70 microseconds.

II. B. Soot Formation Modeling in Diffusion Flames

A model describing soot formation in an opposed jet diffusion flame has been developed by coupling the dynamical sectional equations for spheroid growth with the conservation equations and complex chemistry of counterflow diffusion flames. A schematic of the model indicating the fully integrated nature of the soot formation code and the flame model is provided in Fig. 1. A diagram of the opposed jet flame modeled in this study is shown in Fig. 2 and details of the model are described in Appendix B of this report. The particle kinetics include inception, surface growth and oxidation, and coalescence within the framework of the discrete size spectrum, or sectional representation. Model predictions demonstrate that the particle growth dynamics and transport (by thermophoresis, diffusion, and convection), gas phase chemistry, flame radiation, and flow hydrodynamics are all strongly coupled. Particle inception as well as surface growth and oxidation are all calculated from local conditions, including concentrations of key species. As part of this modeling effort, the benzene formation/decomposition mechanism was updated and a steady-state solution for predicting formation rates of polyaromatic species was developed. Scrubbing of gas phase species during growth and oxidation of the particles is included in the analysis. Non-adiabatic radiative loss by gas and particle emission is also coupled to the energy equation. In Figs. 3 and 4, soot volume fractions are plotted against the normalized coordinant, z', as defined in Fig. 2 and (mathematically) in Appendix B. As can be seen, predictions are qualitatively in good agreement with experimental data. (For details of the calculations and the experimental data see Appendix B and Ref. [3], respectively). Soot appears first just on the fuel-rich side of the peak temperature region, near the benzene/acetylene peak, and grows to a maximum near the stagnation plane. A strong coupling between thermal radiation and soot formation was observed since gas cooling reduces acetylene and benzene formation as well as the Arrhenius factors in inception and surface growth. Under high surface growth conditions, total soot production becomes less sensitive to soot inception rates but can strongly affect local concentrations of gaseous species such as acetylene. This depletion of acetylene will in turn reduce the rate of surface growth. Oxidation can significantly affect predictions of soot growth. The algorithm is highly efficient with accurate solutions of soot volume fractions obtained with only two or three size classes, although accurate solutions of average size and number density require 15 to 20 size classes.

Fig. 1 Diagram of Integrated Soot Formation Model and Flame Code

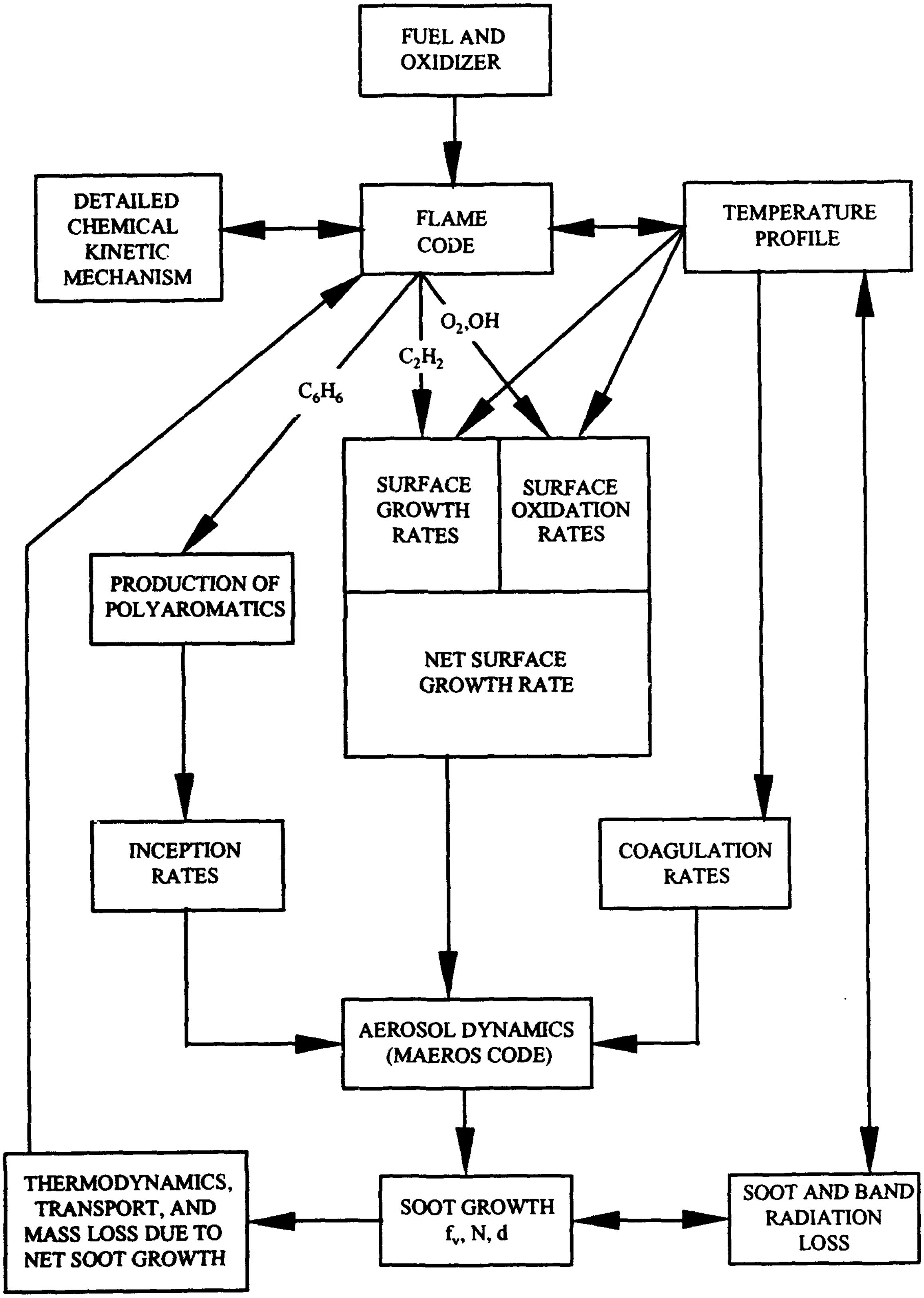
FUEL AND OXIDIZER
DETAILED CHEMICAL KINETIC MECHANISM
FLAME CODE
TEMPERATURE PROFILE
O_2,OH
C_2H_2
C_6H_6
SURFACE GROWTH RATES
SURFACE OXIDATION RATES
NET SURFACE GROWTH RATE
PRODUCTION OF POLYAROMATICS
INCEPTION RATES
COAGULATION RATES
AEROSOL DYNAMICS (MAEROS CODE)
THERMODYNAMICS, TRANSPORT, AND MASS LOSS DUE TO NET SOOT GROWTH
SOOT GROWTH f_v, N, d
SOOT AND BAND RADIATION LOSS

Fig. 2 Configuration of Opposed Jet, Laminar Diffusion Flame

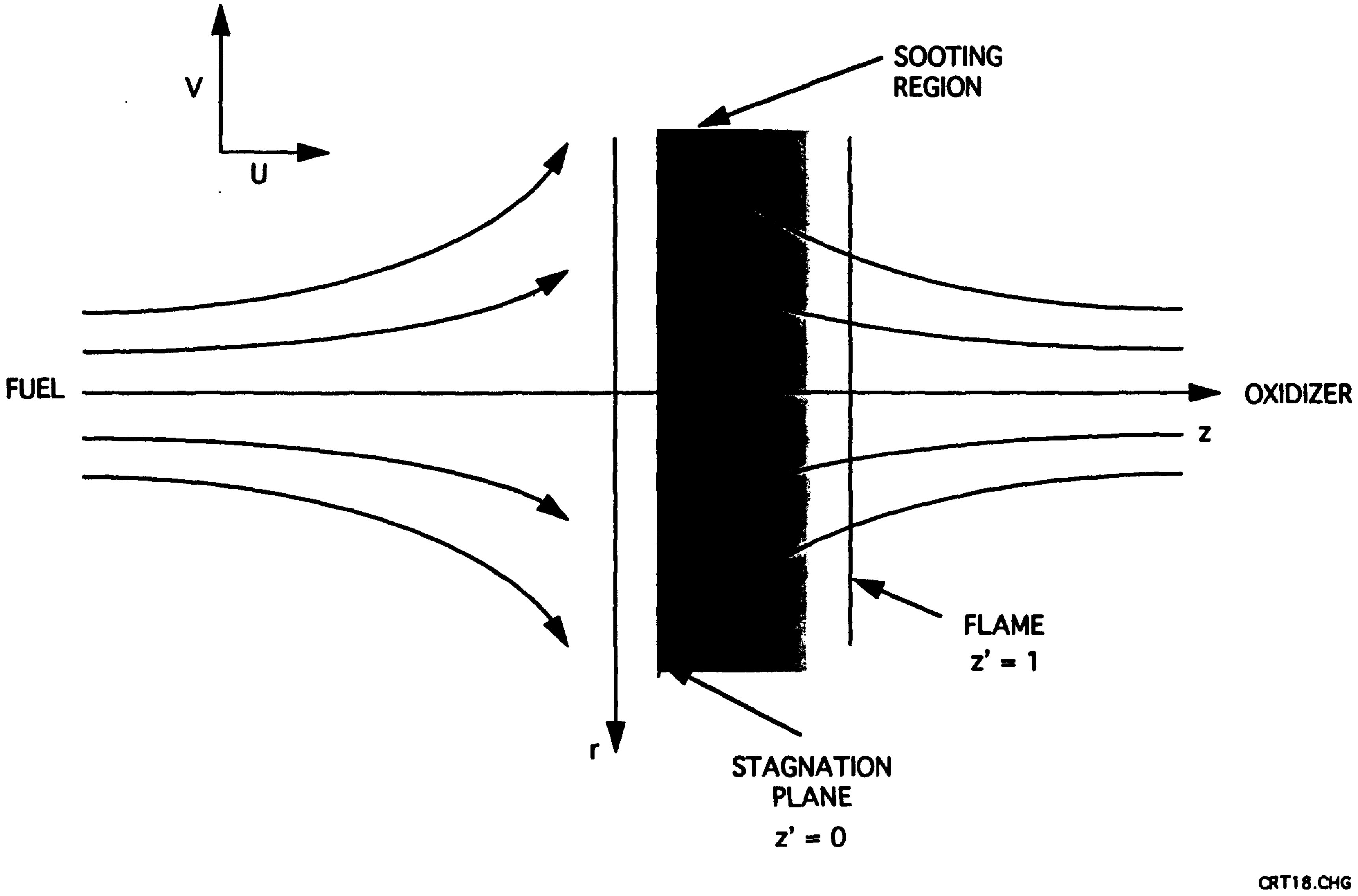
V
U
SOOTING
REGION
FUEL
OXIDIZER
z
FLAME
z' = 1
r
STAGNATION
PLANE
z' = 0
CRT18.CHG

Fig. 3 Predictions of Soot Production with Spatial Evolution of Size Classes

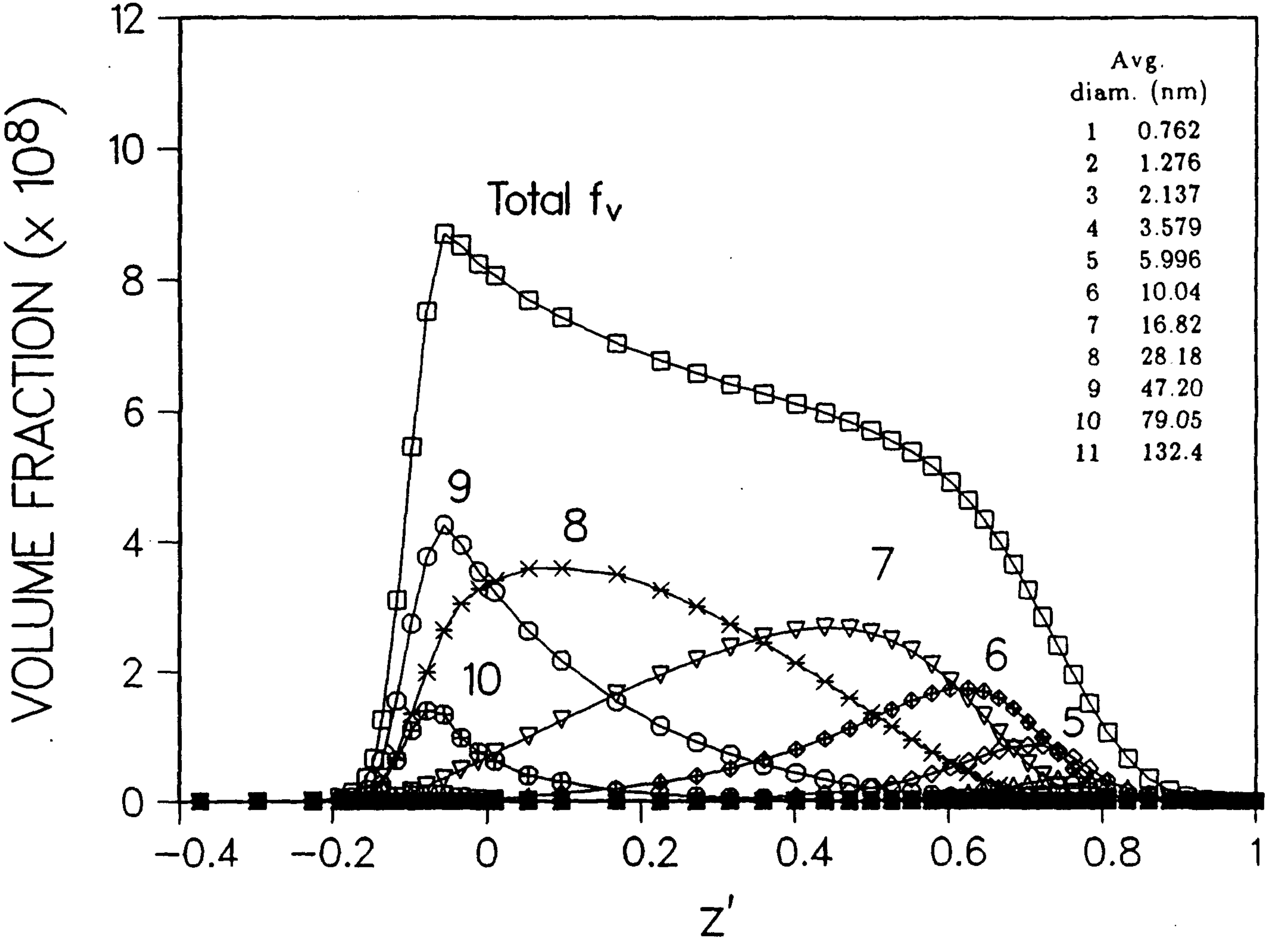

Fig. 4 Experimental Soot Distributions in Opposed-Jet, Methane Flame

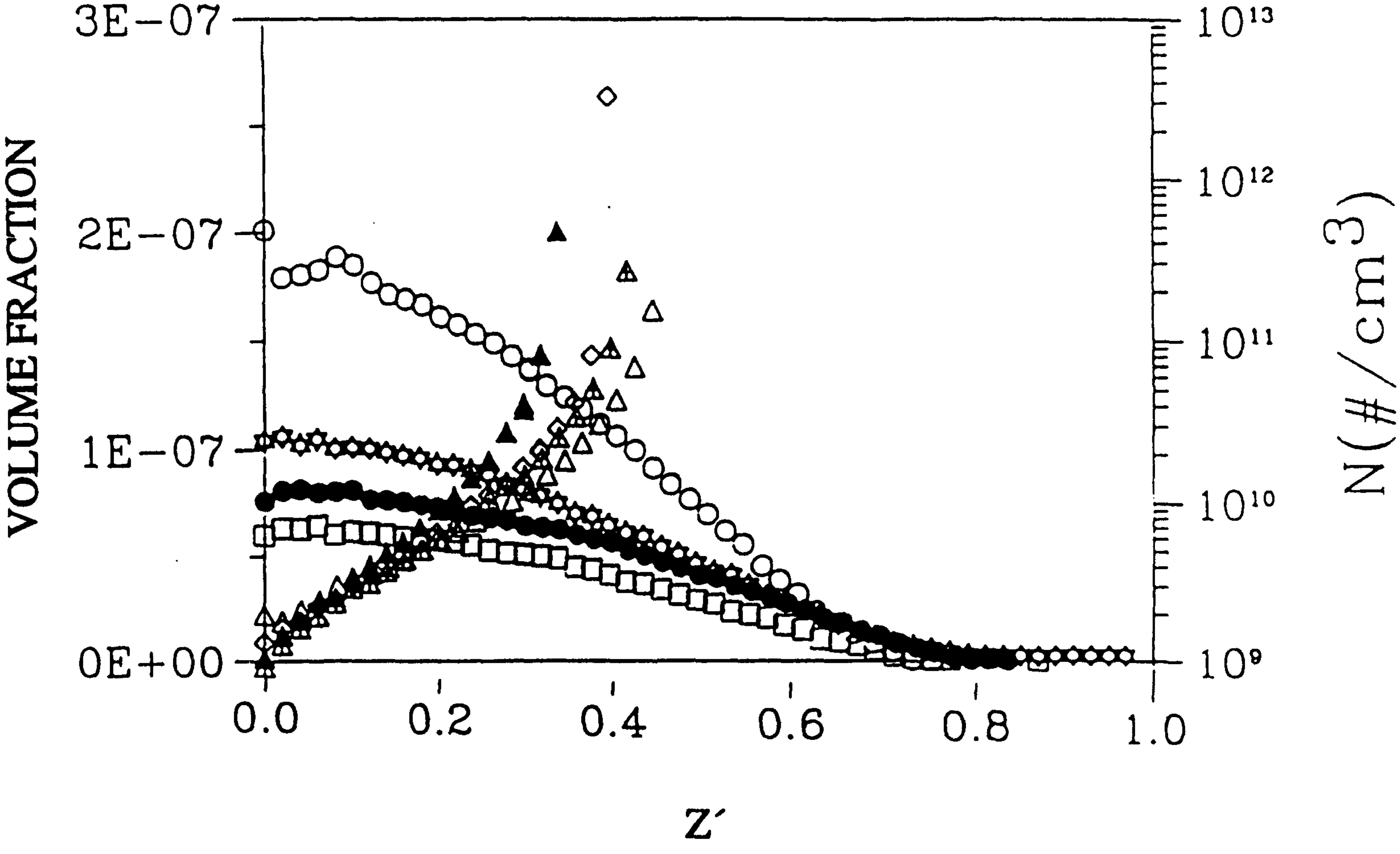

III. List of Publications

A manuscript entitled “Reaction Mechanisms For Toluene Pyrolysis” has been prepared by M. B. Colket and D. J. Seery and has been accepted for presentation at the 25th International Symposium on Combustion, July 31 - Aug. 5, 1994 in Irvine California and has been accepted for publication in the symposium volume. A copy of this paper is provided in Appendix A of this report.

A paper entitled “Predictions of Soot Dynamics in Opposed Jet Diffusion Flames” has been written by R. J. Hall, M. D. Smooke, and M. B. Colket. It has been submitted for publication in the special honorific volume for Professor I. Glassman of Princeton University as one of the Combustion, Science and Technology Book Series, published by Gordon and Breach, 1995, expected publication date. A copy of this paper is in Appendix B of this report.

A manuscript entitled "Radiative Dissipation in Planar Gas-Soot Mixtures" authored by R. J. Hall and has been published in the Journal of Quantitative Spectroscopy and Radiative Transfer, Vol. 51, No. 4, pp. 635-644, 1994. A copy of this paper is included in this report as Appendix C.

A review article describing state-of-the-art modeling of soot formation processes is in preparation. It is co-authored by I. Kennedy and M. Colket.

IV. Meeting Interactions and Presentations

On Oct. 25-27, 1993, M. Colket attended the Eastern States Section of the Combustion Institute at Princeton University.

On Oct. 28, 1993, M. Colket attended by special invitation a Colloquium on Combustion in honor of Professor Irvin Glassman, held at Princeton University.

On June 1-3, 1994, M. Colket attended the 16th Combustion Research Conference held at Granlibakken in Tahoe City, California under corporate funds. M. Colket was invited to this DOE, Basic Energy Sciences Contractor's Meeting to be an observer and participant.

V. Record Of Inventions

There were no inventions during this period.

VI. References

1. M. B. Colket and R. J. Hall, Mechanistic Models of Soot Formation, Annual Report, United Technologies Research Center, Report No. UTRC92-9, East Hartford, CT, July 2, 1992.

2. M. B. Colket, R. J. Hall and M. D. Smooke, Mechanistic Models of Soot Formation, Annual Report, United Technologies Research Center, Report No. UTRC93-28, East Hartford, CT, July 14, 1993.

3. C. Zhang, A. Atreya, and K. Lee, Twenty-Fourth Symposium (International) on Combustion, The Combustion Institute, Pittsburgh, p. 1049, 1992.

Appendix A.
Reaction Mechanisms for Toluene Pyrolysis

REACTION MECHANISMS FOR TOLUENE PYROLYSIS

by
M. B. Colket[*] and D. J. Seery

United Technologies Research Center

Twenty-Fifth International Symposium on Combustion
July 31 to Aug. 6, 1994
Irvine, California

[*] Correspondence should be addressed to:

Meredith B. Colket
United Technologies Research Center
Mail Stop 30
Silver Lane
E. Hartford, CT 06108

Phone: (203) 727-7481
Fax: (203) 727-2151

Subject Headings:	(1.2)	Detailed Reaction Mechanisms
	(1.5)	Thermal Decomposition
	(10.3)	Soot, PAH
	(E)	Experimental Data and Interpretation

Reaction Mechanisms for Toluene Pyrolysis

ABSTRACT

The rich chemistry occurring during the pyrolysis of toluene has been investigated by studying its decomposition in a single-pulse shock tube coupled with detailed chemical kinetic modeling to describe product formation. This work provides information on the initial decomposition steps of toluene and its primary radical benzyl as well as the detailed steps leading to the formation of polyaromatic hydrocarbons. Temperatures ranged from approximately 1200 to 1850K, for 1% toluene in argon, total pressures of approximately 10 atmospheres and residence times near 600 microseconds. Pyrolysis products were collected and analyzed using gas chromatography. Profiles of hydrogen and hydrocarbons ranging from methane to pyrene were obtained. This semi-quantitative data has been interpreted to help resolve many of the existing uncertainties involving the pyrolytic process. In particular, this work supports arguments for a low activation energy process for benzyl radical decomposition as evidenced by the low temperature formation of cyclopentadiene and the radical recombination product, benzyl-cyclopentadienyl. Also, the data support suggestions for an important role of the methylphenyl radical, specifically in the formation of isomers of dimethyldiphenyl and as a key intermediate in the production of anthracene. Minimal evidence for rapid toluene decomposition to phenyl and methyl was found. Importantly, the data support general mechanisms proposed for ring growth sequences, although an additional important step involving ring closure and direct H_2 elimination is suggested by the data. In addition, the data indicates rapid anthracene/phenanthrene isomerization above 1600 K.

INTRODUCTION

The pyrolysis of toluene and related chemistry have been studied by many uthors (1-13). The principal reason for the more recent studies has been that toluene is one of the smallest aromatic molecules implicated in both soot inception and soot growth. Most of these studies have been limited to the initial decomposition steps with little work on subsequent processes, particularly those involving polyaromatic hydrocarbon (PAH) growth mechanisms. Furthermore, there remains a substantial rift between European (9,12-13) and US (8,10-11) authors regarding the relative importance of the primary initiation steps in toluene decomposition and definitive evidence identifying benzyl radical reaction products is lacking.

It is the objective of this study to present some new data and interpretations which will clarify these primary uncertainties and provide new information on PAH formation.

Toluene pyrolysis studies were initiated in this laboratory using a single-pulse shock tube (SPST) more than 10 years ago (8). Only trace concentrations of odd carbon species (except for methane) were observed, yet proposed mechanisms included initial formation of C_5 and C_3 species from fragmentation of benzyl radicals. In addition, recovery of carbon was less than 25% near temperatures at which toluene decomposes rapidly (above 1500K). Subsequently, additional work was performed, including (1) pyrolyzing compounds such as allene, cyclopentadiene, norbornadiene, and phenylacetylene and (2) collection and identification of high molecular weight species (14) using a gas chromatograph/mass spectral detection. The allene work was described previously (8) and helped to identify rapid formation of benzene from C_3 species. In this paper, the recent results on the pyrolysis of toluene will be presented and interpreted.

EXPERIMENTAL APPARATUS AND PROCEDURES

Experiments were performed in a 3.5 cm single-pulse shock tube using hardware and procedures previously described (15). Modifications were made to the gas sampling and analysis systems to collect and more readily identify high molecular weight species. The modifications included higher sample line temperatures (150°C) and use of a thermal conductivity detector for hydrogen analysis and a mass selective detector for identification. A flame ionization detector was used for quantification. Concentrations of the larger PAH's reported in this study may be in error by as much as a factor of two due to uncertainties in collection efficiencies and calibration procedures. More than 50 individual peaks were identified as products and the more dominant are reported. Benzyl-cyclopentadienyl (b-cpd) was identified by its total mass (156) and two very strong peaks at 91 (benzyl) and 65 (cyclopentadienyl). The 7 isomers of dimethyldiphenyl were not individually identified. The data reported here are the combination of all the isomers (total, not average). Five isomers of diphenylmethane at 168 amu and four isomers of pyrene at 202 amu were similarly combined. The data presented in Figs. 1a to 4a were obtained from two separate series of experiments, although some of the data were averaged to clarify the figures.

DESCRIPTION OF RESULTS

Toluene (1% in argon) has been pyrolyzed at total pressures of about 10 atmospheres for approximately 600 microseconds. Final products for a series of individual runs are presented in Figs. 1a-4a for initial post-shock temperatures ranging from about 1200 to 2000K. Many features of these data have been reported in previous studies using a variety of experimental techniques (1,4-6,11,16). Methane, acetylene, diacetylene, and benzene are dominant low molecular weight products. Ethylene has been reported (11), but also observed here are vinylacetylene, propene, C_3H_4's and cyclopentadiene. Most of the high molecular weight species observed here have been reported previously (2,6 and 16). Of particular note is the new observation of b-cpd presumably formed due to the simultaneous presence of benzyl and cyclopentadienyl radicals. It should be recognized that some products (such as b-cpd) may have been formed at least in part during the quenching process in the SPST.

DISCUSSION

A detailed chemical kinetic mechanism has been constructed for comparison with these data. This mechanism is reproduced in Ref (17). Because of space limitations only key reactions and their associated rate constants are listed in Table 1. The reaction sequence was constructed initially from that reported by Brouwer, Muller-Markgraf, and Troe (12) but was modified substantially to include steps describing the formation of aromatics and other species. Also, reactions involving the methylphenyl radical as earlier suggested by Rao and Skinner (10) and by Pamidimukkala, Kern, Patel, Wei, and Kiefer (11) and related steps were included. The reaction sequence involving light species is similar to those reported by (16) and (18). Thermodynamic data for several aromatic species were obtained from the literature and unavailable thermodynamics were estimated using group additivity techniques. Thermodynamic data for selected (aromatic and polyaromatic) species are also provided in Ref (17). CHEMKIN II (20) and a modified version of the Sandia shock tube code (21) were used to perform the kinetic calculations. Modifications enabled inclusion of experimental pressure decays (along with temperature decays assuming isentropic, adiabatic expansion) to estimate the effects of the quenching process. Predictions are plotted in Figs. 1b-4b. In order to understand the behavior of this kinetic set, both a reaction path analysis and SENKIN (22) were used.

Identification of the decomposition pathways of toluene and its initial radicals remains a significant uncertainty in recent literature. Brouwer, et al. (12) suggest that $k_2 \approx 0.1k_1$, whereas Pamidimukkala, et al. (11) require $k_2 \approx 2.5k_1$ in order to interpret laser schlieren data. The primary formation of benzyl vs. phenyl leads to substantially different decomposition pathways. The conclusion by (11) that k_2 is faster than k_1

seems to be unusual in light of the endothermicities of the two reactions (about 88 and 102 kcal/mole for Reactions 1 and 2, respectively). The 14 kcal/mole differential represents two orders of magnitude in the Boltzmann term and would be difficult to overcome by differences in the A-factor. Tsang (23) has recently offered a possible interpretation that following Reaction 1, subsequent thermal equilibration and recombination of the products, H+benzyl$\Rightarrow(C_7H_8)^*$, leads to formation of a thermally excited toluene molecule with sufficient energy to decompose to any of a variety of products. At low pressures, this process might be likely since collisional deactivation is slow. For the high pressures in this study, the Tsang suggestion appears less likely.

At low temperatures (~1200 to 1300K in this study), benzene, methane, hydrogen, and bibenzyl are dominant products. The first two products could be the result of initiation by Reaction 2, but we favor Price's (4) interpretations that these products are due principally to the sequence 1,8,4, whereas, hydrogen and bibenzyl are formed from Reactions 3 and 9, respectively. Indeed, reaction pathway and sensitivity analysis support this interpretation, at least for the mechanism used in this study. In (11), contributions from Reaction 8 were not included, since this reaction is nearly thermally neutral and should not by itself influence the laser schlieren data.

Use of the high value for k_2 obtained by (11) led to substantial overpredictions for methane, ethane, benzene, and ethylbenzene, as well as further increasing the otherwise high prediction for diphenyl production (see Figs. 3a and 3b). Use of the alternative reaction set (12), with its high relative rate for initiation of toluene to benzyl + H leads to high acetylene predictions as shown in Fig. 1b. Much of this acetylene is lost to further molecular weight growth which is not accounted for by the limited mechanism of Table 1.

Two low temperature products coincident with the formation of acetylene (presumably a decomposition product of benzyl or phenyl) are cyclopentadiene (cpd) and benzyl-cyclopentadienyl (b-cpd). This latter product is almost entirely formed during the quenching process via the recombination of the two stable radicals, benzyl and cyclopentadienyl. Traces of several other C_5 species at masses 66 and 68 were observed at levels typically 5 to 10 times below those of cpd. The presence of the C_5 compounds supports arguments for decomposition of benzyl radical. Cpd is preferred since cyclopentadienyl offers the lowest energy path for decomposition (64 kcal/mole). The mechanism for this process has not been described well. Thus, we explored the reverse process by comparing results from cpd pyrolysis with those of cpd/C_2H_2 pyrolysis (24). The rate of toluene formation was enhanced by about an order of magnitude in the presence of acetylene. Following a suggestion (25), the toluene formation may arise from:

$$c\text{-}C_5H_6 + C_2H_2 \Leftrightarrow \text{norbornadiene} \Leftrightarrow \text{toluene} \qquad (A)$$

or

$$c\text{-}C_5H_5 + C_2H_2 \Leftrightarrow \text{norbornadienyl} \Leftrightarrow \text{benzyl} \qquad (B)$$

Known rates (26) for (A) do not account for the high temperature dependence (60 kcal/mole) of toluene formation observed in our cpd/C_2H_2 experiments. We favor (B) which had been suggested (27) for the reverse of benzyl decomposition. Norbornadiene was also shock-heated; only traces of the parent remained even at 1100K along with the products, cpd, toluene, cycloheptatriene, and acetylene, consistent with known isomerization and decomposition.

Consequently, Reaction 10 was adopted as the preferred low temperature benzyl decomposition path. A schematic representation of this process is depicted in Fig. 5. The cpd and b-cpd production were used to help determine a rate for benzyl radical decomposition. Unfortunately, a sensitivity analysis indicates that the concentrations of these species are dependent on both the rates for decomposition of benzyl (Reaction 10) and for cyclopentadienyl radicals (Reaction 13).The rates suggested in Table 1 for these two reactions should be considered accurate to about a factor of three in the temperature range of 1300 to 1500K. The activation energies used here (70 and 71 kcal/mole) are significantly higher than some values reported previously (44.7 and 40, respectively (12)).

In another decomposition path, norbornadienyl could isomerize to cycloheptatrienyl and subsequently decompose. Alternatively, cycloheptatriene could be formed directly from a thermally excited benzyl by bridging of the CH_2 group to the ortho position, followed immediately by ring enlargement and decomposition directly into two acetylenes and a propargyl radical. This overall process requires 142 kcal/mole and therefore appears unlikely.

As indicated in Table 1, an alternative mechanism for benzyl decomposition was included in part because of the results of (6,16 and 28) suggesting two competitive decomposition processes, and the observations of vinylacetylene in this study. Predictions of vinylacetylene were found to be nearly directly proportional to the rate constant selected for benzyl decomposition to C_4H_4+C_3H_3. The initial step for this process may be similar to that suggested by Rao and Skinner (29), although the final products suggested here differ than from the previous proposal. C_4H_3+C_3H_4 was not included since it is endothermic by 120 kcal/mole compared to about 60 and 100 kcal/mole for Reactions 10 and 11, respectively. The rate selected in Table 1 was selected principally by the peak production of vinylacetylene.

Other steps for decomposition of toluene/benzyl could involve the methylphenyl ($CH_3C_6H_4$) radical(s). Pamidumukkla, et al. suggested the formation of such radicals by H-abstraction from the ring. They then allowed its subsequent decomposition following rate kinetics of the phenyl radical. Although this is probably a low limit estimate of the decomposition rate constant, the use of this rate leads to a negligible contribution to overall ring fracture relative to the direct decomposition of benzyl radical.

Growth steps have been nearly ignored by most of the recent kinetic studies despite substantial documentation of PAH production at lower (2,3,5) as well as comparable temperatures (16). Brouwer, et al. included bibenzyl and trans-stilbene in their model; however, the SPST results indicate the spectrum of products is much richer. Some of these high molecular weight species are products of combining stable, long-lived radicals, such as benzyl, cyclopentadienyl, and indenyl, partially or wholly in the rarefaction wave. Condensed ring aromatics and other species such as diphenyl and diphenylmethane (dpm) are principally formed during the period of high temperature pyrolysis, although concentrations can be altered by about 10% as the reacting gases begin to cool.

Figure 3 indicates that although bibenzyl is the dominant high molecular weight species at low temperature (and presumably at early pyrolysis times), the combination of dmdp (dimethyldiphenyl) isomers and dpm isomers each attain nearly comparable levels. These high relative levels of dmdp are comparable to those obtained by Brooks, et al. (5). The dmdp production steps included in Table 1 are logical extensions of the reactions involving the methylphenyl radical, whose possible role in toluene pyrolysis was discussed (11). Some dmdp can also be formed by benzyl addition to toluene. Dpm could be formed by H-atom substitution on dmdp or benzyl radical addition to benzene.

As shown in Fig. 4a, several three-ringed species eventually attain levels similar to those of bibenzyl, including fluorene, anthracene, phenanthrene, and acenaphthylene. Two unusual features are apparent. Firstly, fluorene was produced at fairly high levels for the low temperature pyrolysis. Secondly, anthracene was initially produced at levels substantially greater than its more stable isomer, phenanthrene. Several attempts were made to model fluorene production. Following dpm production, abstraction of an ortho H-atom should lead to rapid ring closure and H-atom elimination. Unfortunately, unless an unreasonably low activation energy was assigned to the H-atom abstraction process, fluorene production was more than an order of magnitude too slow. As an alternative, a direct four-center elimination of H_2 and ring closure is proposed (see Fig. 6). The low pre-exponential (10^8 sec^{-1}) and the activation energy (32 kcal/mole) seem acceptable. Calculations (30) indicate that reorientation of dpm, so that the ortho H-atoms are within close proximity, requires only 5-10 kcal/mole. Previously, Badger and Spotswood (2) implicated recombination of phenyl and benzyl as a precursor to fluorene formation.

Low temperature production of anthracene led to unusually low phenanthrene/anthracene ratios; typically equilibrium levels had been attained in other SPST pyrolyses at elevated temperatures. In contrast the opposite trend was observed during phenylacetylene pyrolysis in the SPST. In Fig. 7, experimental and equilibrium phenanthrene/anthracene ratios are plotted as a function of temperature. The ratios from phenylacetylene pyrolysis are near 10 at low temperatures, but from toluene pyrolysis are about 0.5. As temperature increases above 1600K, the ratios are both driven to equilibrium levels near 2.5. To explain the disparate results at low temperatures, the reaction depicted in Fig. 6 is proposed. Anthracene is assumed to be formed from a specific isomer of dimethyldiphenyl, i.e. $C_6H_5CH_2C_6H_4CH_3$ or o-benzyltoluene, where the attached methyl group is located in the ortho position. Dihydroanthracene can be formed by abstraction of the benzyl H from the ortho methyl group, subsequent ring closure, and H-atom elimination, or by direct ring closure and H_2 elimination. Dehydrogenation of dihydroanthracene is assumed to occur at a rate comparable to that for dehydrogenation of 1,4-cyclohexadiene (26). Several authors have reported the early formation of anthracene (3,31). The proposed mechanism for formation of anthracene is similar to a previous suggestion (32). The facile conversion of o-benzyltoluene has been demonstrated by Errede and Cassidy (3) who found a 91% conversion of o-benzyltoluene to anthracene.

The rapid formation of phenanthrene during the phenylacetylene pyrolysis presumably is due to phenyl addition to phenylacetylene followed by a cyclization process. This sequence is likely similar to the conversion of cis-stilbene to phenanthrene plus H_2.

The fastest step for forming naphthalene is assumed to be Reaction 14, isomerization of the recombination product of benzyl and propargyl. There is little previous evidence for this step, but more conventional processes (i.e., sequential addition of acetylene to phenyl (33) and methyl addition to indene) did not result in reasonable naphthalene production rates. A variety of steps have been included in an attempt to describe pyrene formation. By far the most important is phenyl addition to naphthalene (or naphthalenyl addition to benzene) followed by a four-centered H_2 elimination and ring closure to form fluoranthene (see Fig. 6). Subsequently, fluoranthene may isomerize to pyrene or one of the other isomers at mass 202.

CONCLUSIONS

Single-pulse shock tube pyrolysis of toluene and detailed chemical kinetic modeling has been used to clarify several uncertain features of the decomposition path and PAH growth processes. Initiation of the reaction occurs principally by decomposition of toluene to benzyl+H. Primary C-C cleavage also occurs, more slowly. Benzyl radical decomposition to acetylene plus cyclopentadienyl radical was estimated to have a rate constant of 6×10^{13} exp(-70000/RT) sec^{-1} in support of (12), but 4 times above the revised determination (13) at 1400K. Formation of norbornadienyl is proposed as an intermediate in this decomposition process. The large concentrations of dimethyldiphenyl isomers are consistent with earlier results (2) and strongly support the suggestion (12) of the importance of the methylphenyl radical. Mechanisms and associated rate constants for formation of fluorene and anthracene are proposed and evidence for the anthracene⇔phenanthrene isomerization is presented. An estimated rate constant 8×10^{12} exp(-65000/RT) sec^{-1} is suggested. Ring growth steps follow similar paths and rates as indicated in previous studies (33) except that additional possible processes have been identified. Firstly, four-centered, concerted reactions involving direct H_2 elimination and ring closure with rate constants of 10^8 exp(-E/RT) sec^{-1}, where

30<E<40 kcal/mole, are suggested. Secondly, phenyl addition to naphthalene leading to fluoranthene formation and isomerization to pyrene is indicated by the data.

ACKNOWLEDGMENTS

This work has been supported in part by the Air Force Office of Scientific Research (AFSC) under contract nos. F49620-85-C-0012, F49620-88-C-0051, and F49620-91-C-0056. The encouragement by J. Tishkoff is greatly appreciated. This work would not have been performed without the able technical assistance of D. Kocum of United Technologies Research Center. Detailed technical discussions with H. Palmer, J. Kiefer, R. D. Kern, J. Troe, T. Just, M. Frenklach and W. Tsang have been instrumental in directing this research.

REFERENCES

1. Szwarc, M., J. Chem. Phys. 16:128 (1948).
2. Badger, G. M. and Spotswood, T. M., J. Chem. Soc. 4220 (1960).
3. Errede, L. A. and Cassidy, J. P., J. Am. Chem. Soc. 82:3653 (1960).
4. Price, S. J., Can. J. Chem. 40:1310 (1962).
5. Brooks, C. T., Cummins, C. P. R. and Peacock, S. J., Trans. Far. Soc. 67:3265 (1971).
6. Smith, R. D., J. Phys. Chem. 83:1553 (1979).
7. Astholtz, D. C., Durant, J. and Troe, J., Eighteenth Symposium (International) on Combustion, The Combustion Institute, Pittsburgh, 1981, pp. 885-891.
8. Colket, M. B. and Seery, D. J., Presented at Twentieth Symposium (International) on Combustion, Ann Arbor, MI, 1984.
9. Braun-Unkoff, M., Frank, P. and Just, Th., Twenty Second Symposium (International) on Combustion, The Combustion Institute, Pittsburgh, 1988, pp. 1053-1061.
10. Rao, S. V. and Skinner, G. B., J. Phys. Chem. 88:4362 (1984).
11. Pamidimukkala, K. M., Kern, R. D., Patel, M. R., Wei, H. C. and Kiefer, J. H., J. Phys. Chem. 91:2148 (1987).
12. Brouwer, L. D., Muller-Markgraf, W. and Troe, J., J. Phys. Chem. 92: 4905 (1988).
13. Hippler, H. Reihs, C. and Troe, J., Z. Phys. Chem. Neue Fo. 167:1 (1990).
14. Colket, M. B., Hall, R. J., Sangiovanni, J. J. and Seery, D. J., The Determination of Rate-Limiting Steps During Soot Formation, United Technologies Research Center report no UTRC89-13, 1989.
15. Colket, M. B., Twenty First Symposium (International) on Combustion, The Combustion Institute, Pittsburgh, 1986, pp. 851-864.
16. Smith, R. D., Combust. Flame 35:179 (1979).
17. Colket, M. B., Hall, R. J., and Smooke, M. D., Mechanistic Models of Soot Formation, United Technologies Research Center report no. UTRC94-xx, 1994.
18. Kiefer, J. H., Mitchell, K.I., Kern, R. D. and Yong, J. N., J. Phys. Chem. 92:677 (1988).
19. Wu, C. H. and Kern, R. D., J. Phys. Chem. 91:6291 (1987).

20. Kee, R. J. Rupley, F. M. and Miller, J. A., "CHEMKIN II: A Fortran Chemical Kinetics Package for the Analysis of Gas-Phase Chemical Kinetics," Sandia Report SAND89-8009 (1989).

21. Mitchell, R. E. and Kee, R. J., "A General -Purpose Computer Code for Predicting Chemical Kinetic Behavior Behind Incident and Reflected Shocks," Sandia Report SAND82-8205 (1982).

22. Lutz, A. E., Kee, R. J. and Miller, J. A., "SENKIN: A Fortran Program for Predicting Homogeneous Gas Phase Chemical Kinetics with Sensitivity Analysis," Sandia Report SAND87-8248 (1991).

23. Tsang, W., Chemical and Physical Processes in Combustion, paper no. 19, Princeton Univ. pp. 121-124 (1993).

24. Colket, M. B., Hall, R. J., Sangiovanni, J. J. and Seery, D. J., The Determination of Rate-Limiting Steps During Soot Formation, United Technologies Research Center Report Nos. UTRC90-23 and UTRC91-21, 1990 and 1991.

25. Kiefer, J. H., personal communication.

26. Benson, S. W. and O'Neal, H. E., "Kinetic Data on Gas Phase Unimolecular Reactions," National Bureau of Standards, 1970.

27. Golden, D., personal communication.

28. Muller-Markgraf, W. and Troe, J., Twenty First Symposium (International) on Combustion, The Combustion Institute, Pittsburgh, 1986, pp. 815-824.

29. Rao, S. V., and Skinner, G. B. , Twenty First Symposium (International) on Combustion, The Combustion Institute, Pittsburgh, 1986, pp. 809-814.

30. Montgomery, J. A., personal communication.

31. Hurd, C. D., Levetan, R. V. and Macon, A. R., J. Am. Chem. Soc., 84: 4515 (1962).

32. Hurd, C. D., Macon, A. R., Simon, J. I. and Levetan, R. V., J. Am. Chem. Soc. 84:4509 (1962).

33. Frenklach, M., Clary, D. W., Gardiner, W. C. and Stein, S. E., Twentieth Symposium (International) on Combustion, The Combustion Institute, Pittsburgh, 1984, pp. 887-901.

LIST OF FIGURES

1a. Formation of Aliphatic Products During SPST Pyrolysis of 1% Toluene at 10 atmospheres and 600 microseconds.

1b. Model Predictions of Aliphatic Products During Pyrolysis of Toluene

2a. Formation of Single-Ringed Species During Pyrolysis of Toluene

2b. Model Predictions of Single-Ringed Species During Pyrolysis of Toluene

3a. Formation of Two-Ring Aromatics During Pyrolysis of Toluene

3b. Model Predictions of Two-Ring Aromatics During Pyrolysis of Toluene

4a. Formation of PAH Hydrocarbons During Pyrolysis of Toluene

4b. Model Predictions of PAH Hydrocarbons During Pyrolysis of Toluene

5. Low Temperature Route for Decomposition of Benzyl Radical

6. Proposed Paths for PAH Production

7. Experimental and Equilibrium Phenanthrene/Anthracene Ratios as a Function of Temperature. + Ratios determined from pyrolysis of phenylacetylene; Δ Ratios determined during pyrolysis of toluene; —— Equilibrium ratio; - - - Predictions from chemical kinetic model.

TABLE 1

PROPOSED MECHANISM FOR TOLUENE PYROLYSIS

logk = logA- E/R/T/2.303, units: cc- mole- sec- kcal

	Forward Rate Constant		Reverse Rate Constant	
Reactions	LogA	E	LogA	E
1 C_7H_8=benzyl+H	15.45	88.9	14.24	-0.2
2 C_7H_8=phenyl+CH_3	16.00	97.0	12.92	-0.8
3 C_7H_8+H=benzyl+H_2	14.10	8.4	13.50	23.7
4 C_7H_8+CH_3=CH_4+benzyl	12.20	11.1	13.08	27.1
5 C_6H_6=phenyl+H	16.76	116.0	14.46	6.4
6 C_6H_6+H=phenyl+H_2	14.40	16.0	12.71	10.7
7 C_6H_6+CH_3=phenyl+CH_4	13.30	16.0	13.10	11.5
8 C_7H_8+H=C_6H_6+CH_3	13.08	5.1	12.30	17.0
9 2benzyl=bibenzyl	12.70	0.5	14.93	60.0
10 benzyl=c-C_5H_5+C_2H_2	13.78	70.0	11.57	8.3
11 benzyl=C_4H_4+C_3H_3	14.30	83.6	8.28	-15.6
12 benzyl+c-C_5H_5=b-cpd	12.70	0.0	13.81	49.3
13 c-C_5H_5=C_2H_2+C_3H_3	15.00	71.0	9.75	-3.2
14 C_3H_3+benzyl=naphthalene+2H	11.78	0.0	0.0	0.0
15 naphthalenyl+C_6H_6→pyrene+H+H_2	12.00	5.0	0.00	0.0
16 naphthalene+phenyl→pyrene+H+H_2	11.00	5.0	0.00	0.0
17 DPM=fluorene+H_2	8.00	32.0	10.24	18.3
18 o-benzyltoluene=dhanthracene+H_2	8.00	40.0	9.67	10.7
19 anthracene=phenanthrene	12.90	65.0	12.73	67.0

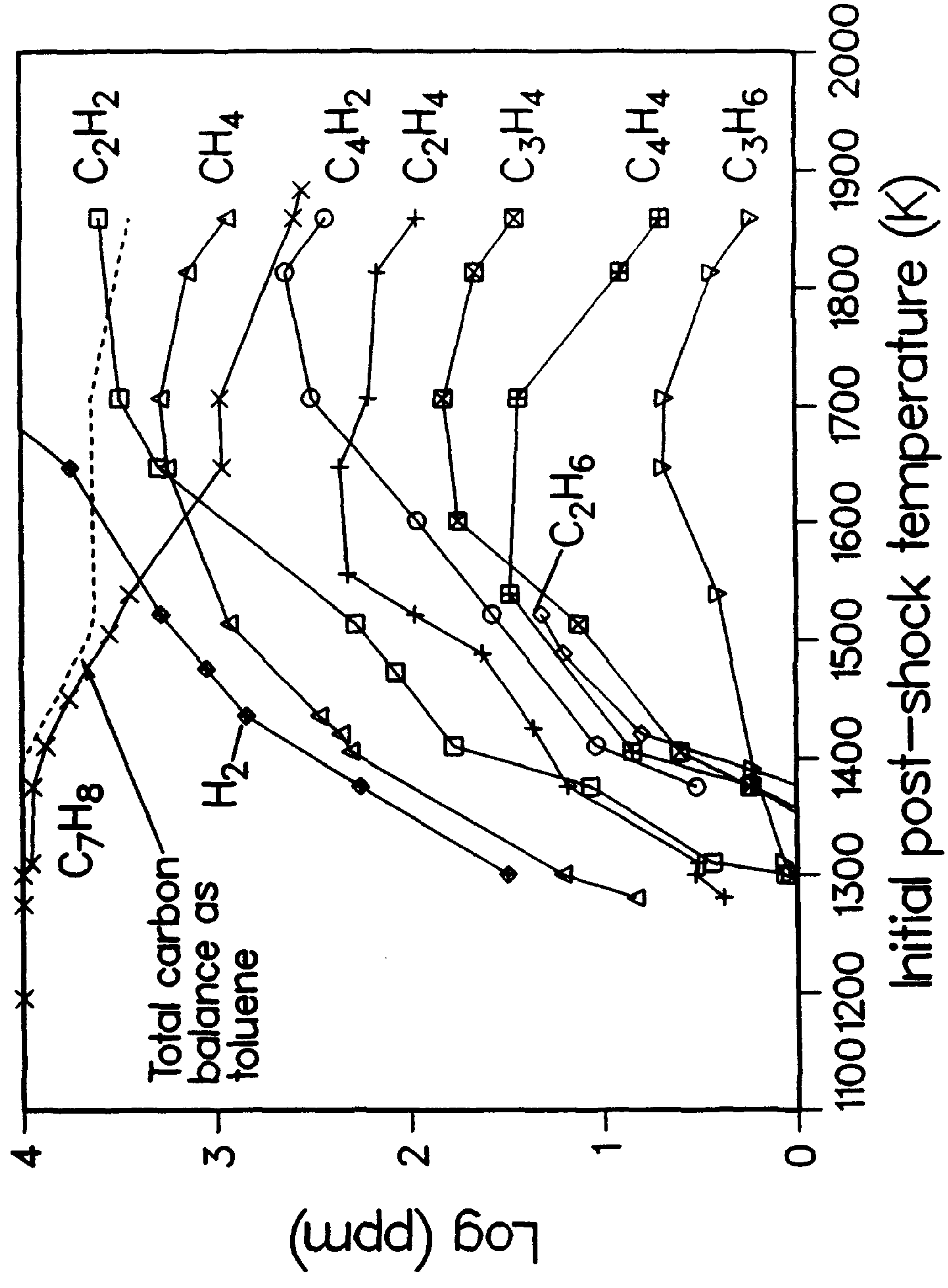

C_2H_2
CH_4
C_4H_2
C_2H_4
C_3H_4
C_4H_4
C_3H_6
C_2H_6
C_7H_8
H_2
Total carbon balance as toluene
Log (ppm)
0
1
2
3
4
1100
1200
1300
1400
1500
1600
1700
1800
1900
2000
Initial post-shock temperature (K)

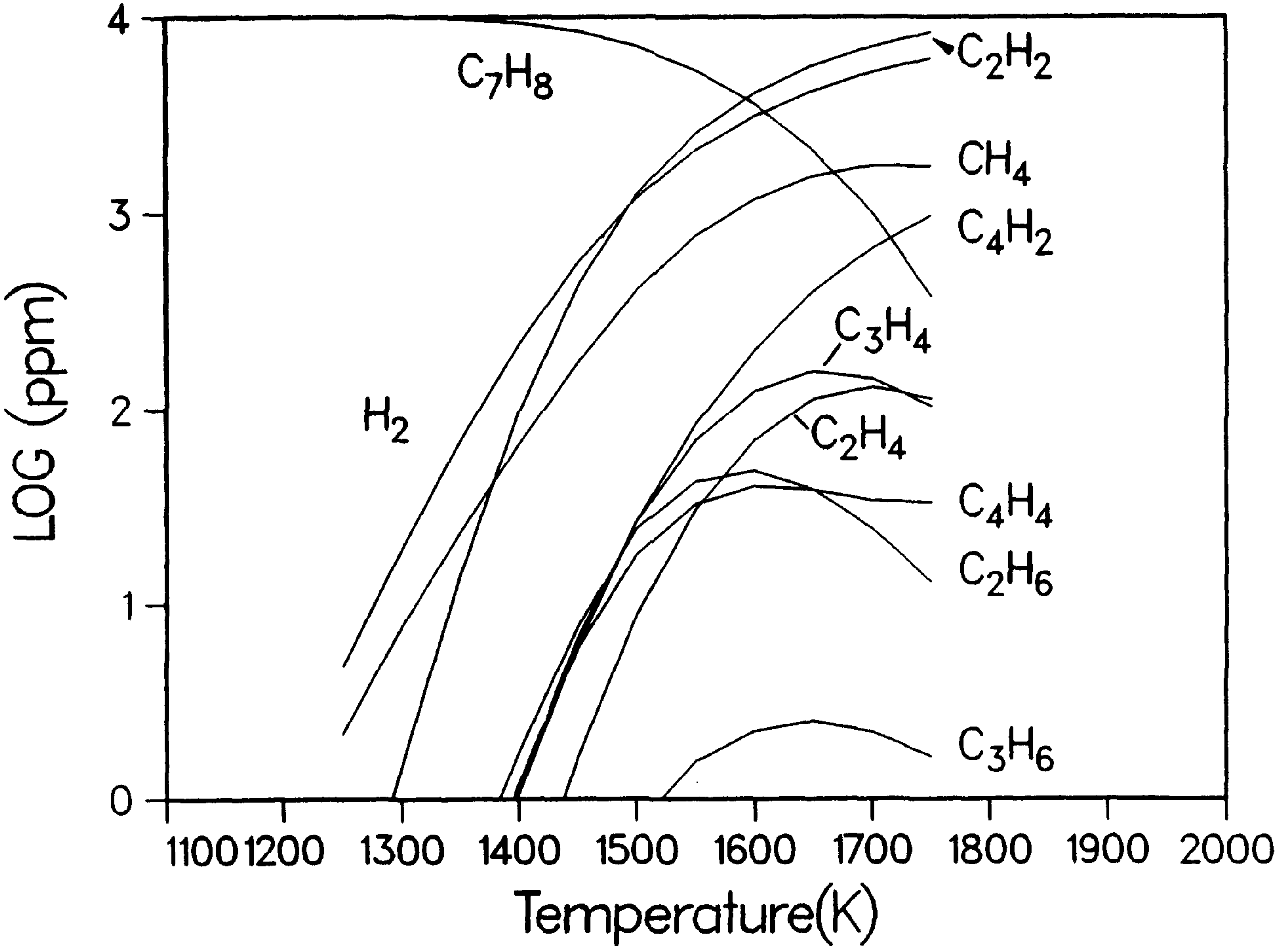
4
3
2
1
0
LOG (ppm)
1100
1200
1300
1400
1500
1600
1700
1800
1900
2000
Temperature(K)
C_7H_8
H_2
C_2H_2
CH_4
C_4H_2
C_3H_4
C_2H_4
C_4H_4
C_2H_6
C_3H_6

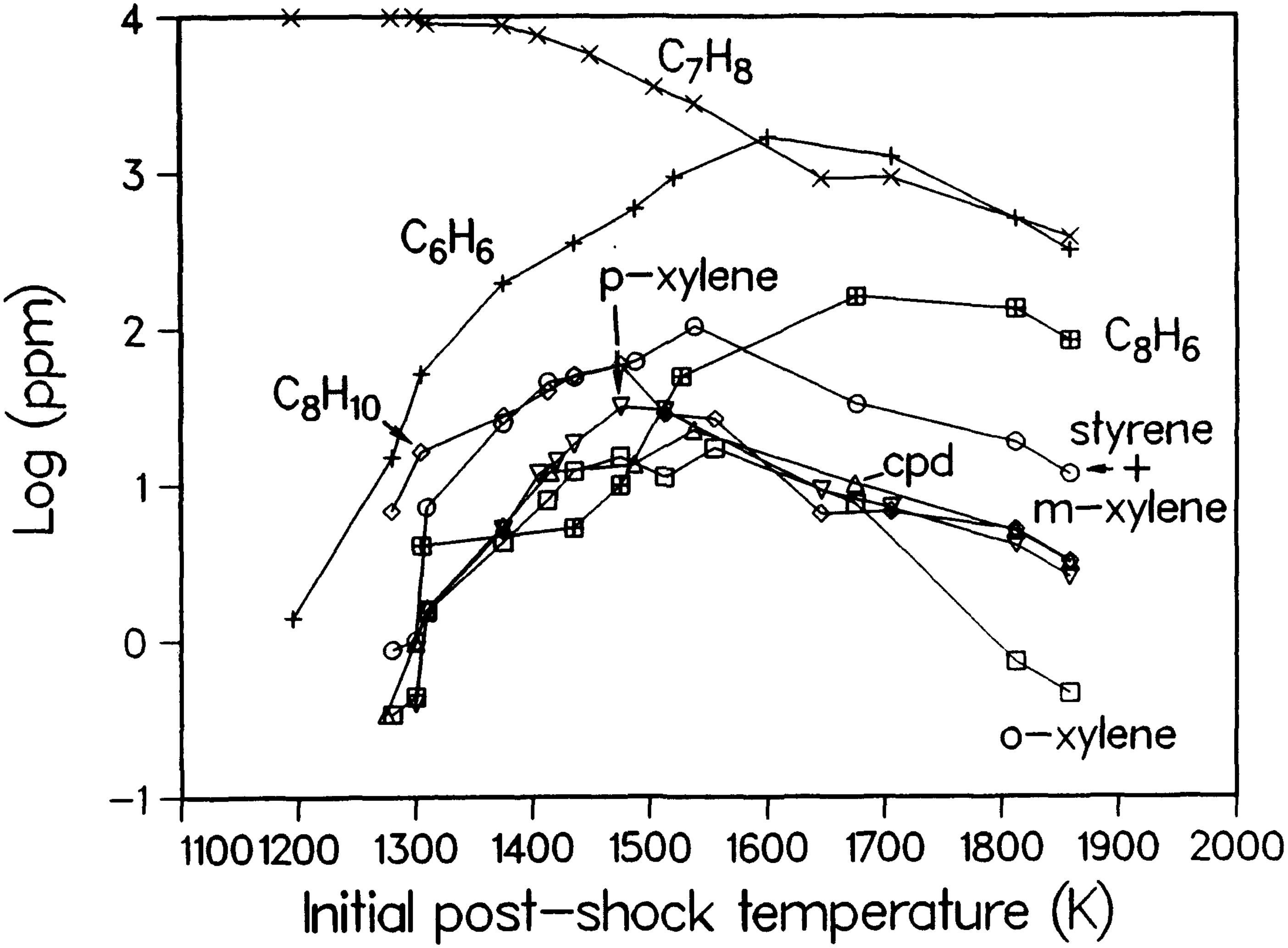
C$_7$H$_8$
C$_6$H$_6$
p−xylene
C$_8$H$_6$
C$_8$H$_{10}$
styrene
+
cpd
m−xylene
o−xylene
4
3
2
1
0
−1
Log (ppm)
1100
1200
1300
1400
1500
1600
1700
1800
1900
2000
Initial post−shock temperature (K)

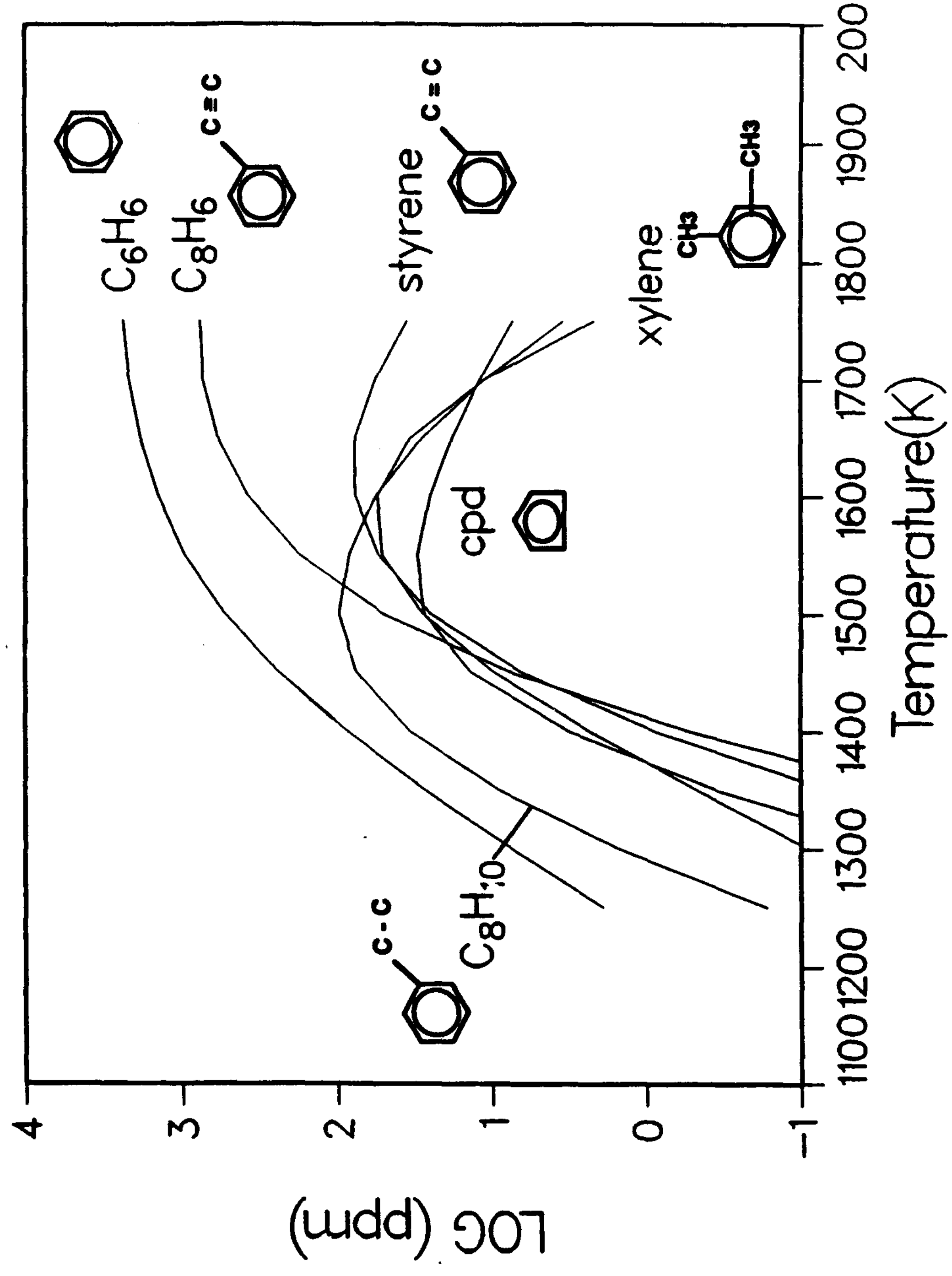
LOG (ppm)
4
3
2
1
0
−1
Temperature(K)
1100
1200
1300
1400
1500
1600
1700
1800
1900
2000
C_6H_6
C_8H_6
C≡C
styrene
C=C
cpd
xylene
CH3
CH3
C_8H_{10}
C-C

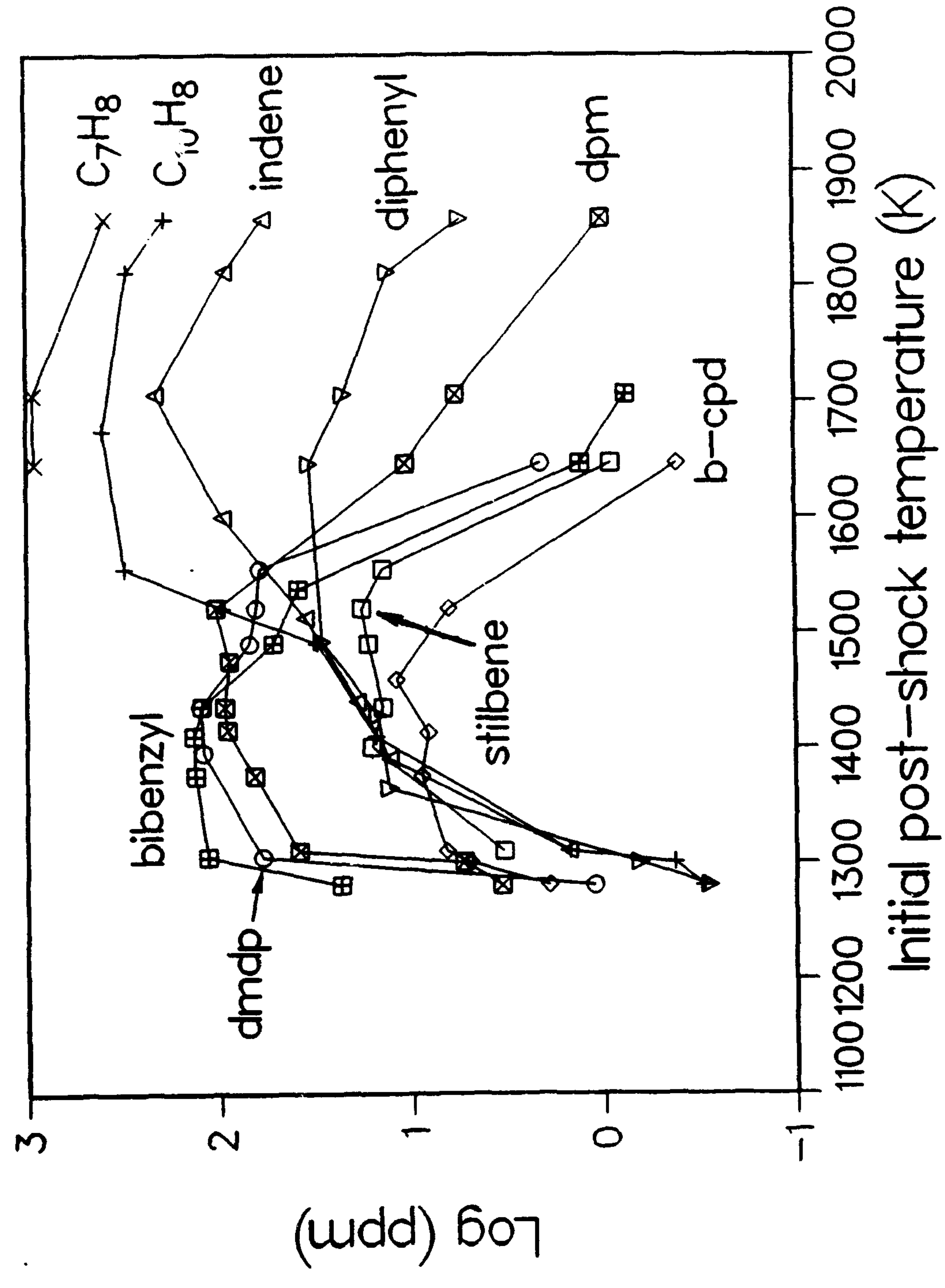

Log (ppm)
3
2
1
0
−1
Initial post−shock temperature (K)
1100
1200
1300
1400
1500
1600
1700
1800
1900
2000
C_7H_8
$C_{10}H_8$
indene
diphenyl
dpm
b−cpd
stilbene
bibenzyl
dmdp

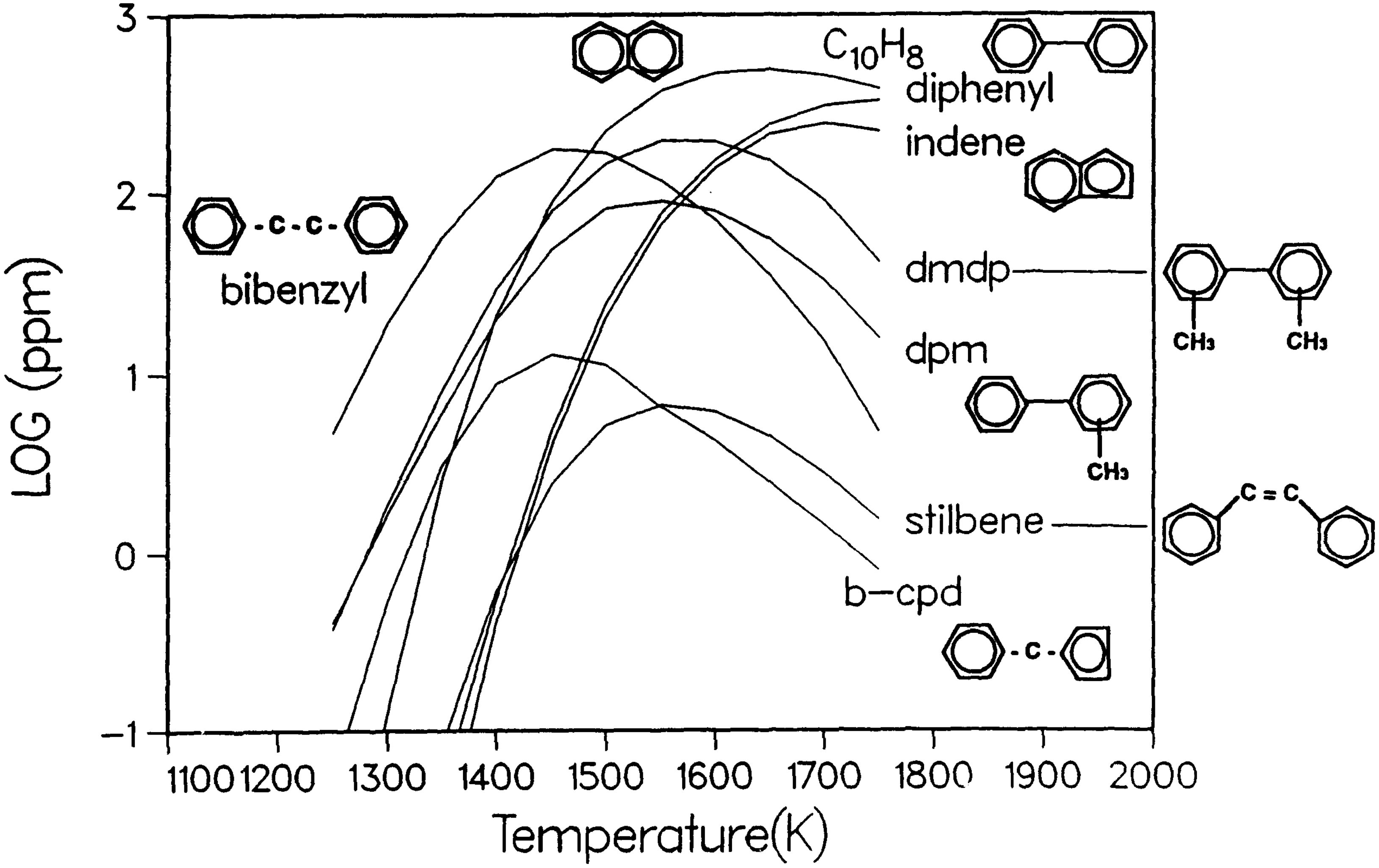
3
2
1
0
−1
LOG (ppm)
1100
1200
1300
1400
1500
1600
1700
1800
1900
2000
Temperature(K)
bibenzyl
$C_{10}H_8$
diphenyl
indene
dmdp
dpm
stilbene
b–cpd
-c-c-
CH₃
CH₃
CH₃
C = C
-c-

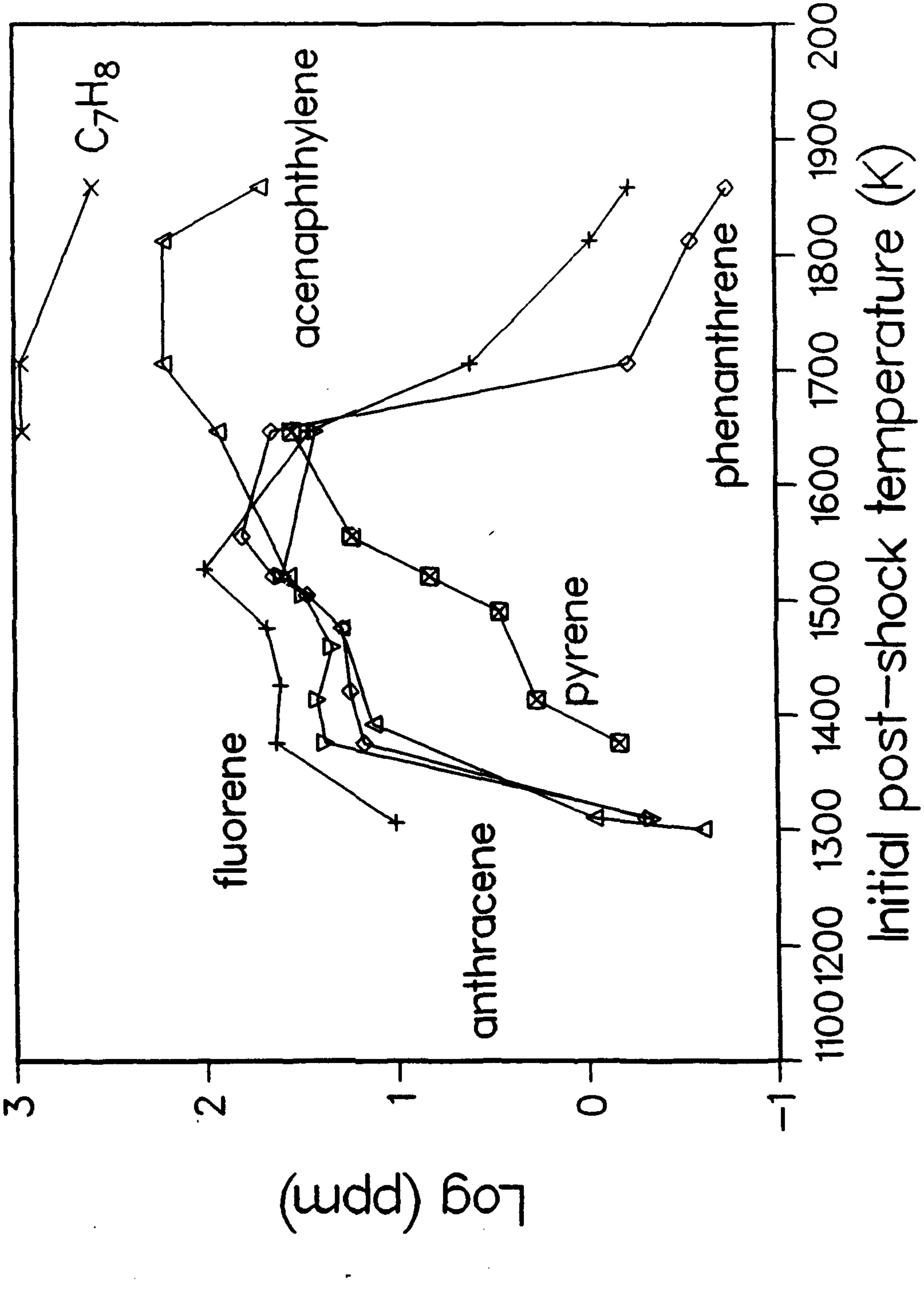
C_7H_8
acenaphthylene
phenanthrene
pyrene
fluorene
anthracene
Log (ppm)
3
2
1
0
−1
Initial post−shock temperature (K)
1100
1200
1300
1400
1500
1600
1700
1800
1900
2000

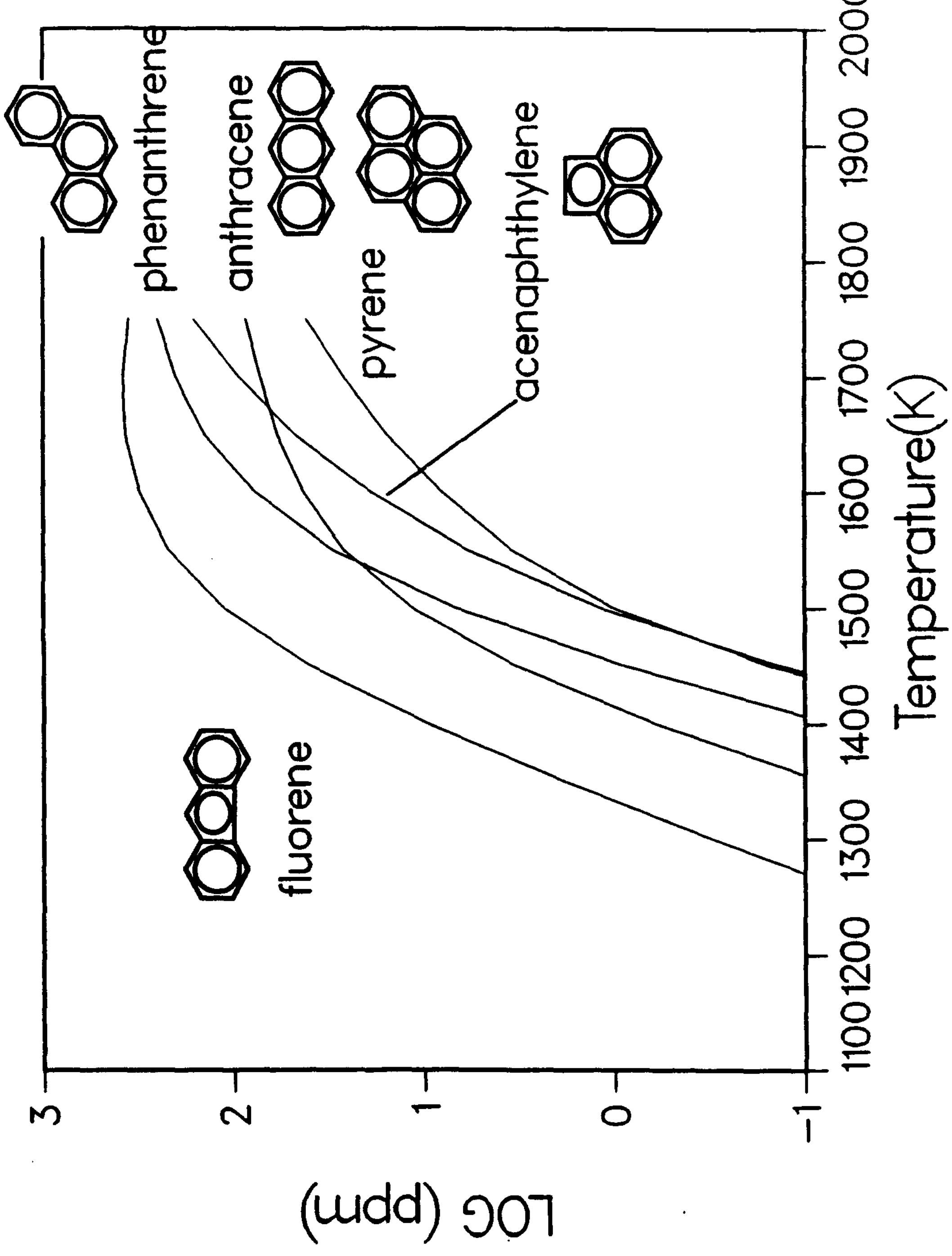
LOG (ppm)
3
2
1
0
−1
1100
1200
1300
1400
1500
1600
1700
1800
1900
2000
Temperature(K)
phenanthrene
anthracene
pyrene
acenaphthylene
fluorene

LOW TEMPERATURE ROUTE FOR DECOMPOSITION OF BENZYL RADICAL

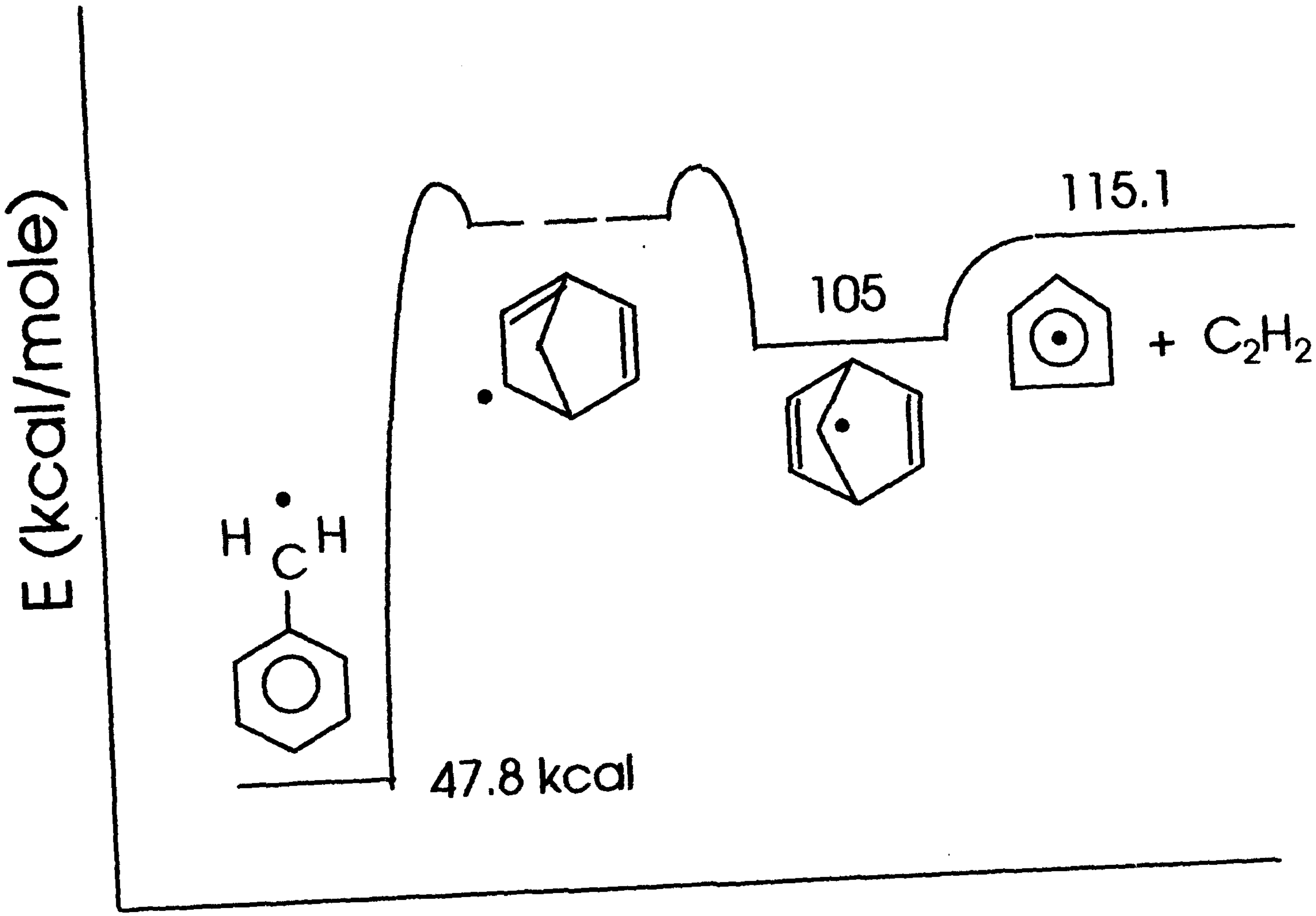
E (kcal/mole)
H C H
47.8 kcal
105
115.1
+ C_2H_2

PROPOSED PATHS FOR PAH PRODUCTION

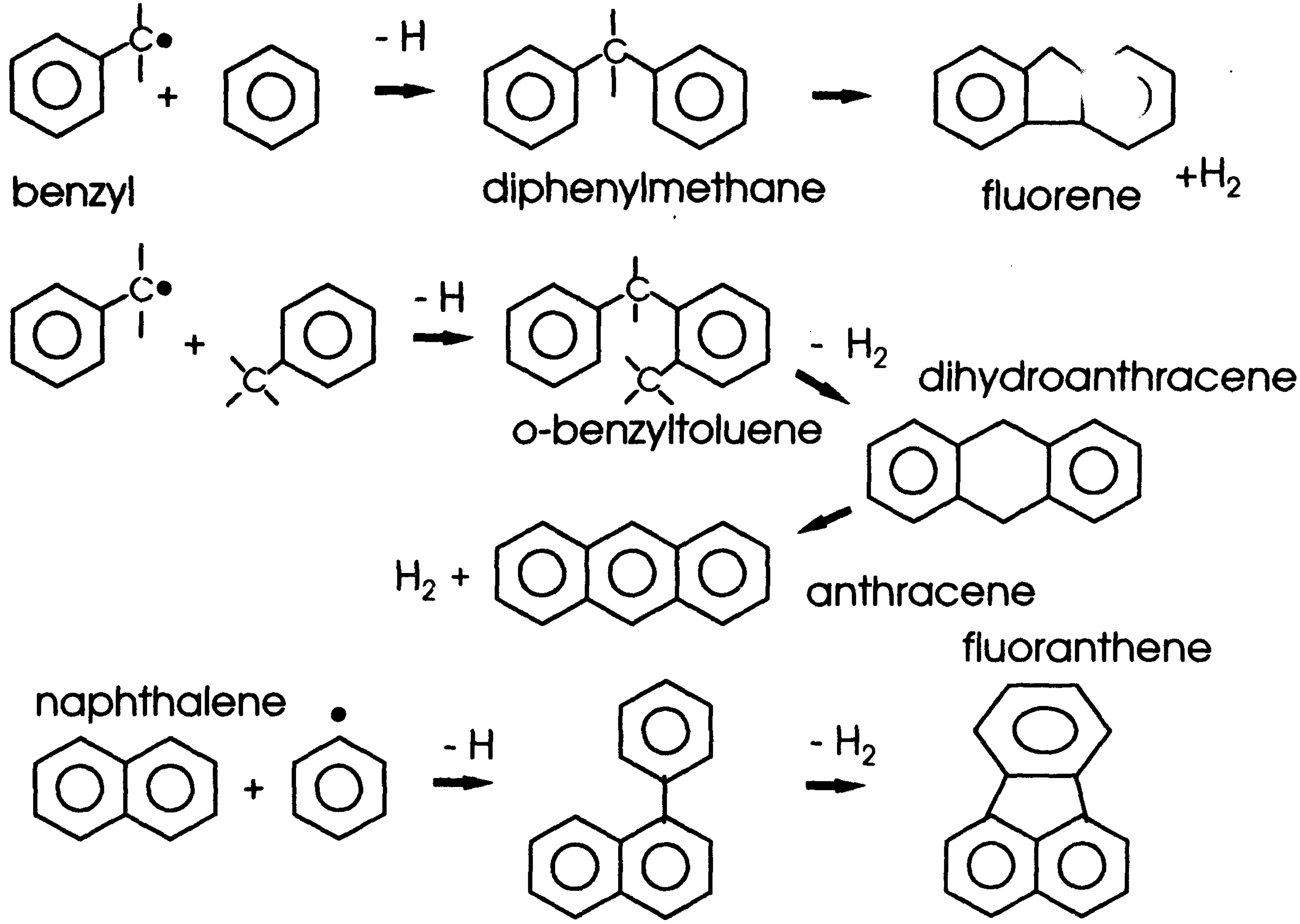
benzyl
- H
diphenylmethane
fluorene
+H2
- H
o-benzyltoluene
- H2
dihydroanthracene
H2 +
anthracene
naphthalene
- H
- H2
fluoranthene

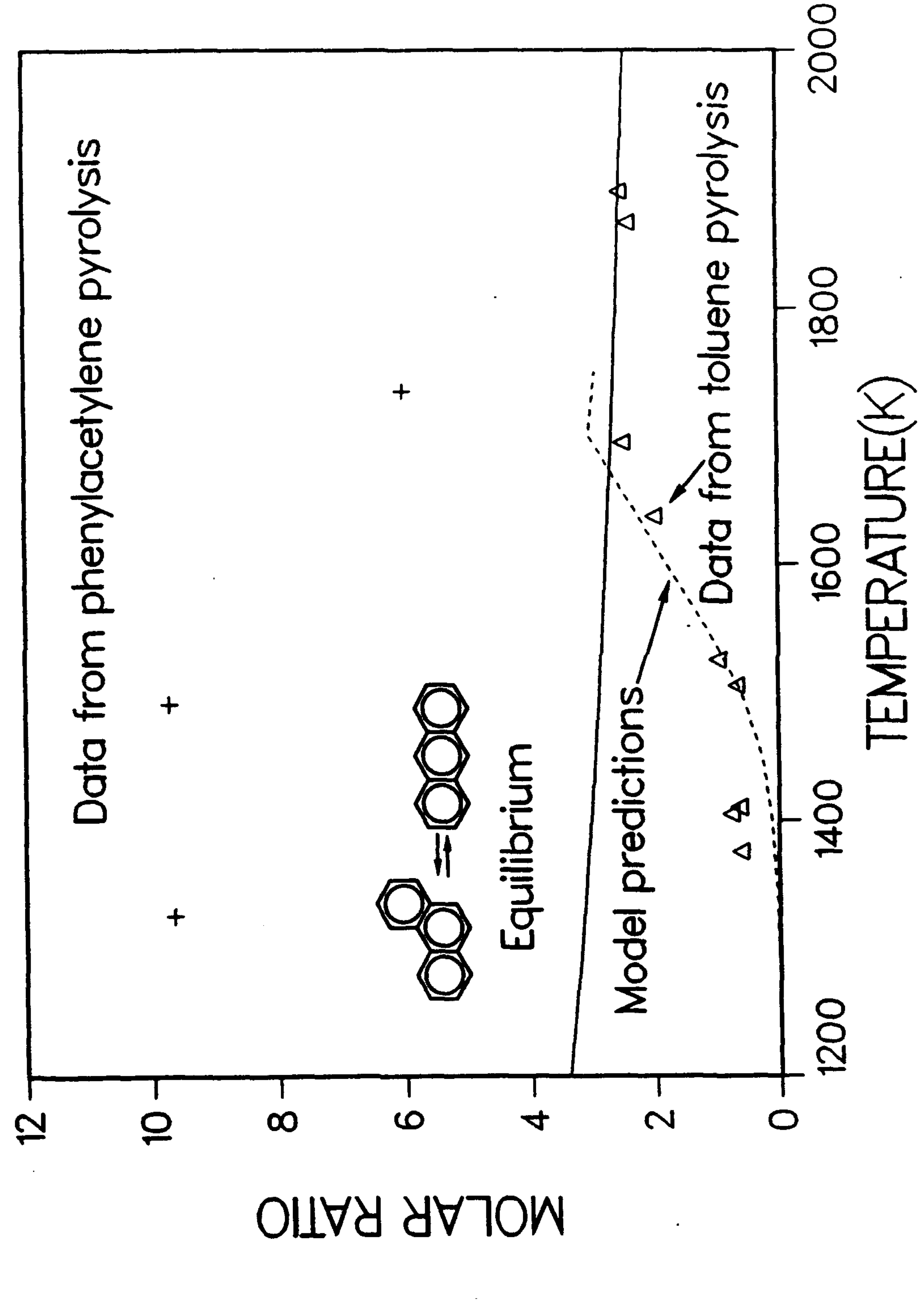
Data from phenylacetylene pyrolysis
Equilibrium
Model predictions
Data from toluene pyrolysis
MOLAR RATIO
0
2
4
6
8
10
12
TEMPERATURE(K)
1200
1400
1600
1800
2000

TABLE 1

PROPOSED MECHANISM FOR TOLUENE PYROLYSIS

logk = logA- E/R/T/2.303, units: cc- mole- sec- kcal

	Forward Rate Constant	
Reactions	LogA	E
1 C_7H_8=benzyl+H	15.45	88.9
2 C_7H_8=phenyl+CH_3	16.00	97.0
3 C_7H_8+H=benzyl+H_2	14.10	8.4
4 C_7H_8+CH_3=CH_4+benzyl	12.20	11.1
5 C_6H_6=phenyl+H	16.76	116.0
6 C_6H_6+H=phenyl+H_2	14.40	16.0
7 C_6H_6+CH_3=phenyl+CH_4	13.30	16.0
8 C_7H_8+H=C_6H_6+CH_3	13.08	5.1
9 2benzyl=bibenzyl	12.70	0.5
10 benzyl=c-C_5H_5+C_2H_2	13.78	70.0
11 benzyl=C_4H_4+C_3H_3	14.30	83.6
12 benzyl+c-C_5H_5=b-cpd	12.70	0.0
13 c-C_5H_5=C_2H_2+C_3H_3	15.00	71.0
14 C_3H_3+benzyl=naphthalene+2H	11.78	0.0
15 naphthalenyl+C_6H_6→pyrene+H+H_2	12.00	5.0
16 naphthalene+phenyl→pyrene+H+H_2	11.00	5.0
17 DPM=fluorene+H_2	8.00	32.0
18 o-benzyltoluene=dhanthracene+H_2	8.00	40.0
19 anthracene=phenanthrene	12.90	65.0

Appendix B.
Predictions of Soot Dynamics in Opposed Jet Diffusion Flames

Submitted to be considered for publication in the
Combustion Science and Technology Book Series,
March, 1994

PREDICTIONS OF SOOT DYNAMICS IN OPPOSED JET DIFFUSION FLAMES

By

R. J. Hall, UTRC, East Hartford, CT

M. D. Smooke, Yale University, New Haven, CT

and

M. B. Colket, UTRC, East Hartford, CT

Abstract

Dynamical equations for spheroid growth have been coupled to conservation equations for opposed jet diffusion flames with complex chemistry and transport to provide an analytical tool for studies of soot formation. The aerosol dynamical equations use the discrete size spectrum, or sectional method with inception, surface growth/oxidation, and coalescence. Particle transport by thermophoresis and diffusion is included. Particle inception is based on an expression involving calculated local concentrations of acetylene and benzene derived from complex chemical mechanisms. Surface growth occurs at a rate that is governed by temperature and local concentration of acetylene, and oxidation by concentrations of oxygen and hydroxyl radical. Thermal radiation by particles and gas phase species is represented by a sink term in the hydrodynamic energy equation. Scrubbing of gas phase species by particle growth and particle thermochemistry are also treated. The result is a strongly coupled gas-particulate system; computations demonstrate the complex interaction between gaseous species, soot production, temperature and radiation and exclusion of any of the above effects can lead to significant errors. Comparisons of model predictions with experimental data for methane flames are presented, and show excellent qualitative agreement. Extensive parametric variations exhibiting the importance of strain rate, thermal radiation, particulate scrubbing of gaseous species, thermophoresis, and oxidation will be presented.

Nomenclature

a	Strain rate
A	Particle surface area (per particle)
A_T	Total particle surface area per unit volume
c_p, c_{pk}	Gas mixture heat capacity; species k heat capacity
C	Constant in expression for soot radiative power density
D	Particle diameter
D	Diffusion coefficient
f_v	Soot volume fraction
G	Net surface growth; Sectional surface growth coefficients
h_k	Gas species k enthalpy of formation
I_b	Planck function evaluated at band center
J	Reduced pressure gradient in radial direction
k	Boltzmann's constant
k_{HW}	Harris-Wiener surface growth rate
K_a, K_b, K_z, K_T	Rate parameters in Nagle, Strickland-Constable oxidation rate expression
$m, \overline{m}$	Particle mass; average particle mass per section
M	Number of particle sections
n	Sectional number density distribution function
N	Species or sectional number density
N_A	Avogadro's number
P	Partial pressure
PR	Van der Waals coalescence enhancement factor
q_r	Net radiative flux
Q	Sectional mass density
R	Specific surface growth or oxidation rate
R_g	Gas constant
S	Mass source/sink rate
t	Time
T	Gas temperature
u	Radial flow velocity
v	Axial flow velocity
v_T	Thermophoretic velocity of sections
v_{Dl}	Diffusive velocity of section l
V	Axial mass flux
V_{ky}	Diffusive velocity of gas species k
V_{edge}	Fuel stream mass flux
V_{wall}	Oxidizer stream mass flux
$\overline{V}$	Thermal collisional velocity of sections
$\dot{w}$	Molar production rate
$W, \overline{W}$	Species molecular weight; average molecular weight

r	Radial coordinate
z	Axial coordinate
Y	Mass fraction of species or section

Greek symbols

α	Integrated band intensity; thermal accommodation coefficient, Frenklach-Wang surface growth steric factor
$\beta, \overline{\beta}$	Coalescence collision frequency; inter-sectional average collisional frequency
δ	Dirac delta function
λ	Thermal conductivity
μ	Gas viscosity
ν	Stoichiometric coefficient in gas-solid scavenging analysis
ξ	Mixture fraction
ρ, ρ_s, ρ_i	Gas density; soot specific density; density of i-th gasesous species
χ'	Parameter in Nagle, Strickland-Constable oxidation rate expression

I. Introduction

A. Effects of soot formation in flames

Many of the effects of soot formation have been discussed in detail in a great number of technical and review papers (see, e.g. Wagner, 1979; Haynes and Wagner, 1981; Glassman, 1988; Smith, 1981; and Barfknecht, 1983). These articles have discussed pollution (including carcinogens) plume visibility, component lifetimes, and radiation. More recently, as combustion models have advanced, the significant importance of soot formation to flame modeling has also been recognized.

The two most obvious and acknowledged flame processes affected by soot are radiation and emissions. Fractional energy losses from radiation as high as twenty to thirty percent (Markstein, 1984; Hall and Bonczyk, 1991) are not unusual for coflow diffusion flames. Emissions have long been known to effect visibility of combustion exhaust and, most recently, signicant health effects of combustion-generated soot have been highlighted in a New York Times front page article (July 19, 1993). The depression of temperature due to radiative losses can in turn effect flame length (Bhattacharjee and Grosshandler, 1988) and other temperature-dependent processes such as formation of other pollutants, particularly NOx. A secondary but potentially important effect in a strongly sooting flame is the fuel/soot thermochemistry which can vary dramatically depending on fuel-type. Also, soot particles formed in a pyrolytic region can then be transported into an oxidizing zone where oxidation processes are much slower than the kinetics of gas-phase oxidation thus altering the heat release rates and the temperature profiles. In flames in which substantial fractions of fuel carbon are converted to soot, this local extraction of fuel carbon can lead to an alteration of the effective local equivalence ratio of the gas-pahse species leading to a shift in the local H_2/H_2O and CO/CO_2 conversion fractions and hence local heat release. Thus, for flames in which flame-front chemistry controls pollutant production (e.g. prompt NO) these many temperature-perturbing effects of soot formation may be non-trivial.

B. Brief review of soot formation modeling

During the past several years, there has been a dramatic increase in attempts at modeling soot formation in premixed and both laminar and turbulent diffusion flames. By necessity, however, as flame geometry and structure increases in complexity the assumptions regarding the soot model become more simplified. So far, reasonable agreements have been obtained for many of the flames examined. These excellent results should be considered a major success story in combustion modeling. For laminar, premixed flames, Frenklach and coworkers (1985, 1987, 1988 and 1990) are using the most sophisticated soot model which includes detailed reaction chemistry up to and including large PAH structures, perhaps the most realistic inception concepts, detailed growth and oxidation steps, and conventional aerosol dynamics including size-dependent processes. This approach has been very successfull at predicting sooting limits in premixed flames (Markatou, et al, 1993). Colket and Hall (1994) have used generally similar approaches for premixed flames although a sectional model has been used to simplify the aerosol equations. In addition, they related the inception species current to the benzene current using the method of characteristics. Although this assumption overestimates inception and is physically unrealistic, it allows for a great simplification in the gas-phase kinetics while still treating the general features of the stability of aromatics and its importance to soot production.

For more complex flames greater simplifications have been utilized, although there is some concern for extrapolation of these models to significantly different conditions, i.e use of practical fuels, high inlet temperatures, high pressures, etc. These more global models use simpler inception concepts and assume a monodisperse size distribution with two dynamical equations, one for the particle number density and the other for the volume fraction. Specific concerns include the use by Kennedy, et al. (1990) of empirical specific soot growth rates (expressed as a function of mixture fractions) obtained for the same fuel (ethylene) in an opposed jet diffusion flame operating at the same ambient conditions as for their model of coflow laminar and turbulent diffusion flames. Predictions were found to be essentially independent of assumed inception rates. Others assume inception is proportional to the acetylene concentration and a surface growth rate proportional to the square root of the surface area. Sivathanu and Gore (1993) have shown this approach provides good results for coflow diffusion flames while Fairweather, et al. (1992) and Leung, et al. (1991) have incorporated these assumptions into a flamelet/p.d.f. code for turbulent jets. Extrapolation of these assumptions to ambient conditions far outside the range of tested conditions is probably uncertain. Typically for these codes, radiative loss fractions are assumed. As Sivathanu and Gore have shown, however, there can be a strong coupling to radiation. In their study, changes in the radiative-loss fraction of just 15% were found to effect dramatically temperatures and hence soot kinetics. Consequently, predictions of soot volume fractions were altered by as much as an order of magnitude.

C. Objectives of this work

The objectives of this work are to develop a code which fully integrates detailed gas-phase chemical kinetics with known processes involved with soot production in flames, including inception, growth, oxidation, agglomeration, radiation, thermochemistry, scavenging, and transport. We have selected a laminar, opposed jet flame code (Smooke, Puri, and Seshadri, 1986) for modification. An advantage of such a configuration is that, once the gas-phase chemistry is defined, solutions could be obtained for a variety of flames of differing fuel type and ambient conditions from which 'empirical' growth rates, etc. could be determined as input to codes describing more complex flame geometries. It is not the purpose of this study to identify specific or recommended flame chemistry for formation of aromatics (or PAHs), or for selecting valid inception or growth models. Rather, it is an objective of this study to develop a tool (computer code) which is general enough such that a variety of such models/concepts could be examined and, consequently, sensitivities to uncertainties of such processes can be estimated.

This manuscript describes details of the code and assumptions used in its development. In addition, perturbation effects due to inclusion/exclusion of various phenomena such as oxidation, species scavenging (by soot) and radiation from soot or from gas-phase species are examined. Methane is assumed to be the fuel for these studies. Since methane is a relatively lightly sooting fuel, many of the effects described herein are probably low limit estimates. As part of this effort a kinetic analysis comparing various routes to the formation of benzene in a methane fired system has been performed in order to minimize additional reactions and species required to model benzene formation and destruction. The major conclusions of this investigation are included.

II. Description of Model

A. Problem formulation - opposed jet diffusion flame code

To model the combined gas phase/soot-laden counterflow diffusion flame (Figure 1), we utilize the elliptic form of the two-dimensional conservation equations in cylindrical coordinates for the gas phase together with sectional species equations. The complexity of the entire system is reduced (Smooke and Giovangigli, 1992) by seeking a similarity solution of the form $u = rU(z)$, $v = v(z)$, $Y_k = Y_k(z)$, $k = 1, 2, \ldots K, K+1, \ldots, K+M$, $T = T(z)$, where x and y denote the independent radial and axial spatial coordinates, respectively; T, the temperature; Y_k, the mass fraction of the k^{th} gas phase species or the $(k-K)^{th}$ soot size class and u and v the radial and axial components of the velocity. If we substitute the expressions for the two velocities into the continuity and the momentum equations, we find that the reduced pressure gradient in the radial direction is constant, i.e., $\frac{1}{r}\frac{\partial P}{\partial r} = J$, where P denotes the pressure. If we use this result, together with the similarity assumptions, we find that the two-dimensional set of governing equations can be reduced to a nonlinear two-point boundary value problem in the axial direction. The governing equations for mass, momentum, chemical species, soot size classes and energy can be written in the form

$$\frac{dV}{dz} + 2\rho U = 0 \tag{1}$$

$$\frac{d}{dz}\left(\mu\frac{dU}{dz}\right) - V\frac{dU}{dz} - \rho U^2 - J = 0 \tag{2}$$

$$-\frac{d}{dz}(\rho Y_k V_{ks}) - V\frac{dY_k}{dz} + (\dot{w}_k^g + \dot{w}_k^s)W_k = 0, \quad k = 1, 2, \ldots, K \tag{3}$$

$$-\frac{d}{dz}(\rho Y_k(v_T + v_{D_k})) - V\frac{dY_k}{dz} + \dot{Q}_k = 0, \quad k = K+1, K+2, \ldots, K+M \tag{4}$$

$$\frac{d}{dz}\left(\lambda\frac{dT}{dz}\right) - c_p V\frac{dT}{dz} - \sum_{k=1}^{K}\rho Y_k V_{k_s} c_{pk}\frac{dT}{dz} - \sum_{k=1}^{K}(\dot{w}_k^g + \dot{w}_k^s)W_k h_k + \frac{dq_r}{dz} = 0 \tag{5}$$

and

$$\rho = \frac{P\overline{W}}{R_g T} \tag{6}$$

where $V = \rho v$, and, in addition to the variables already defined, ρ denotes the mass density; W_k, the molecular weight of the k^{th} species; $\overline{W}$, the mean molecular weight of the mixture;

R_g, the universal gas constant; λ, the thermal conductivity of the mixture; c_p, the constant pressure heat capacity of the mixture; c_{pk}, the constant pressure heat capacity of the k^{th} species; $\dot{w}_k^g$, the molar rate of production of the k^{th} species per unit volume due to gas phase chemistry, $\dot{w}_k^s$, the molar rate of production of the k^{th} species per unit volume due to scrubbing/replenishment by the soot growth/oxidation processes; $\dot{Q}_k$ the rate of change of section k due to aerosol processes; h_k, the specific enthalpy of the k^{th} species; μ the viscosity of the mixture; V_{ky}, the diffusion velocity of the k^{th} species in the y direction; v_T and v_{D_k} the thermal and mass diffusion velocities of the k^{th} soot size class and $\frac{\partial q_r}{\partial y}$ the divergence of the the net radiative flux which in the optically thin limit is given by (Hall, 1993 and 1994)

$$\frac{dq_r}{dy} = Cf_vT^5 + 4\pi \sum_{ik} \alpha_{ik}\, \rho_k I_{bik} \qquad (7)$$

where the *ik* summation is taken over the optically active bands *i* of the k^{th} gas phase species and where C is a constant that is a function of the soot index of refraction. At low strain rates, ~5-20% conversion of flame enthalpy release to radiative loss can occur (Vranos and Hall, 1993; Hall, 1994), leading to gas temperature reductions large enough to affect soot formation, as will be seen. Soot contributions to the density and heat capacity are usually small and have been ignored. Thermal equilibrium between the gas and the particulate phases has also been assumed. The form of the chemical production rates and the gas phase diffusion velocities can be found in detail in Giovangigli and Darabiha (1988).

The boundary conditions and solution algorithm for the resulting two point, boundary value problem posed by Equations 1-7 are discussed in Appendix A.

B. Gas-phase chemistry

Except for the aromatic fomation/destruction chemistry, the methane reaction set used in this study is identical to that used previously (Smooke, et al., 1992) to examine methane coflow flames. This reaction mechanism includes a relatively small C_2-reaction chemistry set. Several reactions and species have been added to this mechanism to include formation and destruction of benzene. The added reactions are listed in Table I. The entire mechanism contains 33 species and 102 elementary reactions. The benzene kinetics were based on an evaluation of benzene formation mechanisms (Colket and Smooke, 1993) during oxidative pyrolysis of methane in a single-pulse shock and a recent proposal (Bittker, 1991) for the oxidation of benzene. In the shock tube study, six different steps forming benzene were compared including several $C_4 + C_2$ reactions. By far, the most dominant step was the propargyl-propargyl recombination recently suggested to be the predominant benzene forming step during allene pyrolysis (Kern, et al., 1988) and in acetylene flames (Miller and Melius, 1992). Modeling using this reaction predicted benzene profiles in reasonable agreement with the single-pulse shock tube data on benzene production during partial oxidation of methane.

TABLE I
SET OF REACTIONS AND RATE COEFFICIENTS DESCRIBING BENZENE FORMATION AND DESTRUCTION

$\log k = \log A + n\log T - E/R/T/2.303$ *

	REACTIONS	FORWARD RATE CONSTANT		REVERSE RATE CONSTANT	
		LogA	E	LogA	E
1	$C_3H_4+H=C_2H_2+CH_3$	13.60	2.4	12.28	12.6
2	$C_3H_4+H=C_3H_3+H_2$	12.00	1.5	11.02	22.4
3	$CH_3+C_3H_4=C_3H_3+CH_4$	12.30	7.7	12.83	29.5
4	$2C_3H_3=>C_6H_5+H$	13.00	0.0	0.00	0.0
5	$C_6H_6+H=C_6H_5+H_2$	14.40	16.0	12.67	10.5
6	$C_6H_5+H=C_6H_6$	13.70	0.0	16.03	109.9
7	$C_6H_5+CH_4=C_6H_6+CH_3$	12.48	5.0	12.69	9.6
8	$C_6H_5=\text{l-}C_6H_5$	13.65	72.5	10.02	8.6
9	$\text{l-}C_6H_5=>2C_2H_2+C_2H$	14.00	36.0	0.00	0.0
10	$C_6H_5+O_2=>\text{c-}C_5H_5+CO+O$	12.32	7.5	0.00	0.0
11	$\text{c-}C_5H_6=H+\text{c-}C_5H_5$	15.30	81.0	14.32	1.2
12	$H+\text{c-}C_5H_6=H_2+\text{c-}C_5H_5$	12.48	8.0	12.10	32.5
13	$H+\text{c-}C_5H_6=C_2H_4+C_3H_3$	12.70	18.0	8.62	14.1
14	$CH_3+\text{c-}C_5H_6=CH_4+\text{c-}C_5H_5$	12.70	5.0	13.83	30.4
15	$\text{c-}C_5H_5=C_2H_2+C_3H_3$	14.00	74.0	8.69	3.6
16	$C_6H_6+OH=C_6H_5+H_2O$	13.33	4.6	12.27	14.4
17	$C_6H_6+O=\text{c-}C_5H_5+CO+H$	13.44	4.9	11.23	1.1
18	$\text{c-}C_5H_5+O=>C_2H_3+C_2H_2+CO$	13.70	0.0	0.00	0.0
19	$C_6H_5+OH=>\text{c-}C_5H_5+CO+H$	13.00	0.0	0.00	0.0

* NOTES:

Units for A: cc, moles, sec.

Units for E: kcal/mole.

“ = ” represents forward and reverse directions included in model.

“ - ” represents forward direction only included in model.

With this mechanism, profiles of gas-phase species were calculated using the conventional version of the opposed-jet flame code. Calculated values are shown in Figures 2 and 3 for two different strain rates. Species are plotted versus a the normalized coodinate used by Zhang, et al. (1992):

$$z' = \frac{z - z_{stag}}{z_{fl} - z_{stag}} \tag{8}$$

where y_{fl} is the location of the peak flame temperature and y_{stag} is the location of the stagnation plane. These predictions can be compared with those obtained by Zhang, et al. The benzene profile (both shape and magnitude) as well as most other species profiles are predicted well by the kinetics model, although acetylene concentrations appear to be overpredicted. Since the local temperature for benzene formation is about 1400-1500K in the flame, while benzene production in the shock tube occurred at temperatures of 1700-1800K, it is concievable that an alternative benzene formation mechanism may be contributing in the flame system. Consequently, a test was performed by including all benzene steps (see Colket and Smooke, 1993) and appropriate steps for the formation and destruction of the intermediate species. Using this larger reaction set, virtually no change in the benzene production was observed, while if the propargyl recombination step was removed, peak benzene profiles were reduced by more than two orders of magnitude. The importance of this reaction to benzene production in a methane system has also been found by Lindstedt and Skevis (1994).

Besides the reduced oxidation sequence for decomposing benzene, an important step in defining the benzene profile is the thermal decomposition of the phenyl radical. Changes in this rate constant led to nearly comparable changes in the peak concentration of benzene.

C. Soot Inception

A variety of assumptions for soot inception have been made in the literature. These include inception based on acetylene concentrations, benzene production, as well as production of polyaromatic structures of different sizes. In order to minimize complications to the reaction chemistry while attempting to approach the use of a more realistic inception process, simplified steady-state assumptions were used to estimate the formation of two- and three-ringed aromatic species. Consider, for example, the two sequences:

$$\begin{array}{lll} C_2H_2 + C_6\dot{H}_5 \leftrightarrow C_8H_6 + H & [20] & K_{eq,20} = 10^{-1.81}e^{+805/T} \\ H + C_8H_6 \leftrightarrow C_8\dot{H}_5 + H_2 & [21] & K_{eq,21} = 10^{1.69}e^{-2667/T} \\ C_2H_2 + C_8\dot{H}_5 \rightarrow C_{10}\dot{H}_7 & [22] & k_{22} = 10^{12}e^{-2516/T}\ \mathrm{cc/mole/sec} \end{array} \tag{9}$$

or

$$2C_2H_2 + C_6\dot{H}_5 \rightarrow C_{10}\dot{H}_7 + H_2 \quad \text{(overall)}$$

and

$$\begin{array}{rlll} C_6H_6 + C_6\dot{H}_5 \leftrightarrow C_{12}H_{10} + H & [23] & K_{eq,23} = 10^{-1.16}e^{-1107/T} & \\ H + C_{12}H_{10} \leftrightarrow C_{12}\dot{H}_9 + H_2 & [24] & K_{eq,24} = 10^{1.36}e^{-2768K} & \\ C_2H_2 + C_{12}\dot{H}_9 \rightarrow C_{14}H_{10} + H & [25] & k_{25} = 10^{12.3}e^{-2516/T} \text{ cc/mole/sec} & \end{array} \tag{10}$$

or

$$C_2H_2 + C_6H_6 + C_6\dot{H}_5 \rightarrow C_{14}H_{10} + H + H_2 \quad \text{(overall)}$$

Assuming steady state values of $C_8\dot{H}_5$, C_8H_6, $C_{12}H_{10}$, and $C_{12}\dot{H}_9$ and that $H_2 << C_2H_2$, the rate of production of the polyaromatic species can be estimated to be

$$\frac{d[C_{10}\dot{H}_7]}{dt} = K_{eq,20}K_{eq,21}k_{eq,22}\frac{[C_2H_2]^2}{[H_2]}[C_6\dot{H}_5] \tag{11}$$

and

$$\frac{d[C_{14}H_{10}]}{dt} = K_{eq,23}K_{eq,24}k_{eq,25}\frac{[C_2H_2]}{[H_2]}[C_6H_6][C_6\dot{H}_5] \tag{12}$$

or using the rate and equilibrium 'constants', these expressions become

$$\frac{d[C_{10}\dot{H}_7]}{dt} = 10^{11.88}e^{(-4378/T)}\frac{[C_2H_2]^2}{[H_2]}[C_6\dot{H}_5] \tag{13}$$

and

$$\frac{d[C_{14}H_{10}]}{dt} = 10^{12.50}e^{(-6390/T)}\frac{[C_2H_2]}{[H_2]}[C_6H_6][C_6\dot{H}_5] \tag{14}$$

where the gas phase concentrations and temperatures can be evaluated at local conditions. With the further assumptions that inception is limited by the formation of polyaromatics and oxidation/decomposition of such species can be neglected, the inception rate, S_i, in grams/cc/sec was initially assigned to

$$S_i = 127 \times \frac{d[C_{10}\dot{H}_7]}{dt} + 178 \times \frac{d[C_{14}H_{10}]}{dt} \tag{15}$$

where the constants (molecular weights) are provided to convert from molar to mass units. As will be indicated later, soot production using this rate was small and the inception rate for most of this study was assumed to be eight times that calculated from the sum of the above terms. For all cases examined in this study, surface growth (Equation 1b), was the dominant term.

The 'requirement' for an augmented inception rate could be due in part to several other model uncertainties. For example, the rate of naphthalene and phenanthrene formation as calculated by Eqn. (15) could itself be low. The recent results by Colket and Seery (1994) and Lindstedt and Skevis (1994) suggesting that other steps contribute significantly to PAH growth support this argument. Alternatively, the rate of surface growth could be in error. Kennedy and coworkers had to utilize an empirical surface growth rate term since the HW expression inadequately described the rate of soot growth in their flames. A high inception rate could be required to offset a low surface growth rate. Also, inaccuracies in the kinetics set could be in part responsible. Either the benzene concentration is underpredicted, or the oxygen concentration is overpredicted by the kinetics model. It seems unlikely that the benzene concentration is that poorly predicted. The substantial non-zero concentration of oxygen on the fuel side (see Figures 2 and 3) seems unusual, although comparable behavior of oxygen was observed using more complete methane oxidation mechanism (Glarborg, et al., 1986) as well. With a lower level of oxygen in the soot growth region or a shifting of the oxygen profile away from the fuel rich region, predicted soot concentrations can be substantially increased without augmenting the inception rate.

Because of the potential uncertainties in the model, the reader is reminded that the focus of this paper is the description of the model and the demonstration that soot formation is a result of complex interactions between chemical and physical phenomena causing perturbations to local temperatures and gas-phase species.

D. Soot Growth Model(s)

Several procedures for calculating the rate of surface growth of soot particles were considered. These include the Harris and Weiner (1983) expression (HW), the Frenklach and Wang (1990) procedure (FW) and a modification (MODFW) of the FW method (Colket and Hall, 1994). In this study, the multiplicative parameter, α, required for the FW procedure is assigned a value of 1.0, although this value may be an order of magnitude too high near the high temperatures in a diffusion flame. For most of the results presented here, the HW expression

$$\frac{d[m]}{dt} = k_{HW}\ A\ P_{C_2H_2} \tag{16}$$

has been used. A is the surface area of the soot particle and $P_{C_2H_2}$ is the partial pressure of acetylene in atmospheres. Using an overall activation energy for the soot growth process of 31.8 kcal/mole (Hura and Glassman, 1988) and Harris and Weiner's measured rate at 1650K of 3×10^{-3} grams/sec/cm^2/atm, k_{HW} is determined to be 47 exp(-16004/T) gram/sec/cm^2/atm. Ageing (Dash, 1985) which reduces particle surface growth rates with increasing time was not included in this problem.

E. Soot Dynamics

1. Aerosol Model

The growth of soot spheroids has been modeled as a classical aerosol dynamics problem, involving the division of the size range of interest into discrete intervals or classes with a logarithmic transformation of the size range, and then deriving a source for the size class mass densities with terms representing inception, surface growth (or oxidation), and coagulation (coalescence). The sectional analysis is discussed by Gelbard and Seinfeld (1980) and Gelbard, Tambour, and Seinfeld (1980), and uses certain algorithms of the well-known MAEROS program (Gelbard, 1982). It is assumed that surface growth and coalescence have the free molecule form, and that the spheroids consist of the single component, carbon.

In the sectional analysis, it is assumed that the boundaries of the sections vary linearly on a log scale. Thus, if we have M sections, with diameter minima and maxima D(0) and D(M), respectively, the sectional boundaries will be given by

$$D_\ell = D(0)\left(\frac{D(M)}{D(0)}\right)^{(\ell/M)} \tag{17}$$

Section ℓ ($1 \leq \ell \leq M$) will thus have the boundaries m(ℓ-1) and m(ℓ) in particle mass where

$$m = \rho_s \, \frac{\pi D^3}{6} \tag{18}$$

and the soot density ρ_s is taken to be that of solid carbon, 1.8 g/cc. If n_ℓ(m,t) represents the number density per unit mass of particles within a section, the total mass Q_ℓ within the section is given by the integral

$$Q_\ell = \int_{m_{\ell-1}}^{m_\ell} m \; n_\ell(m,t) \; dm \tag{19}$$

Choosing, as in Gelbard, the form

$$n_\ell(m,t) = \frac{Q_\ell}{m^2} \, \Delta_\ell \tag{20}$$

where

$$\begin{gathered} \Delta_\ell = \left(\ell n \, \frac{m_\ell}{m_{\ell-1}}\right)^{-1} = (X_\ell - X_{\ell-1})^{-1} \\ X = \ell n(m) \end{gathered} \tag{21}$$

results in the following expression for the total number density of particles in class ℓ

$$N_\ell = \int_{m_{\ell-1}}^{m_\ell} n_\ell(m,t)\ dm = Q_\ell\ \Delta_\ell \left(\frac{1}{m_{\ell-1}} - \frac{1}{m_\ell}\right) = \frac{Q_\ell}{\overline{m}_\ell} \tag{22}$$

where the average particle mass $\overline{m}_\ell$ in section ℓ is given by

$$\begin{aligned} \overline{m}_\ell &= \frac{\int_{m_{\ell-1}}^{m_\ell} m\ n_\ell(m,t)dm}{\int_{m_{\ell-1}}^{m_\ell} n_\ell(m,t)dm} \\ &= \Delta_\ell^{-1} \left(\frac{1}{m_{\ell-1}} - \frac{1}{m_\ell}\right)^{-1} \end{aligned} \tag{23}$$

The per particle rate of growth due to surface mass addition and oxidation has been assumed, as discussed, to be proportional to particle surface area (free molecule or large Knudsen number form)

$$\frac{dm}{dt} = G'(t)A = G(t)m^{2/3} \tag{24}$$

where A is the particle surface area, and the specific growth rate has the overall form

$$\begin{aligned} G'(t) = (&\text{Growth rate by acetylene or other growth species addition} \\ &- \text{oxidation rate by } O_2,\ OH)/\text{unit surface area.} \end{aligned} \tag{25}$$

$$\text{or} \quad G'(t) = R_G - R_{O_2} - R_{OH}$$

The mass addition term R_G (see Eqn. 16) has been derived for several kinetic models of the surface growth process, as discussed in the preceding section. Oxidation of soot by OH radicals is assumed to proceed at a gas kinetic collision frequency multiplied by a collision probability of 0.13 (Neoh, Howard, and Sarofim, 1981). Thus, with N_{OH}, and N_A representing the OH number density and Avogadro's number, respectively, the OH oxidation is

$$\begin{aligned} R_{OH} &= (0.13) \times N_{OH}\sqrt{\frac{R_g T}{2\pi W_{OH}}} \times \frac{12}{N_A} \\ &= 16.7\ \frac{P_{OH}}{\sqrt{T}} \end{aligned} \tag{26}$$

where P_{OH} is the OH partial pressure in atmospheres, and the specific growth rate is in c.g.s. units. For oxidation by O_2, the Nagle & Strickland-Constable (1963) expression is used. For an O_2 partial pressure P_{O_2} in atmospheres, the specific oxidation rate is thus

$$R_{O_2} = 12 \times (\frac{K_a P_{O_2} \chi'}{(1 + K_z P_{O_2})} + K_b P_{O_2} (1 - \chi')) \tag{27}$$

where K_a, K_b, K_z, K_T, and χ' are as given by Nagle & Strickland-Constable.

At atmospheric pressure, the coalescence rates, β for flames are in the free-molecule regime, and thus given by

$$\beta(m, m') = PR\ (m, m') \frac{\pi}{4} (D_m + D_{m'})^2\ \overline{V}_{mm'}$$

with

$$\overline{V}_{mm'} = \sqrt{\frac{8kT}{\pi} \left(\frac{1}{m} + \frac{1}{m'} \right)} \tag{28}$$

and provision is made for a Van-der Waals enhancement factor PR. For collision partners of low and similar mass, theory predicts enhancements of the gas kinetic rate by as much as 2.2 (Harris and Kennedy, 1988); we use a nominal value of 1.5 for all interactions. In principle, it should be possible to include the mass dependence of the PR in the sectional $\overline{\beta}$ calculation.

The dynamic balance equation for the Q_ℓ can be represented as

$$\begin{aligned} \frac{dQ_\ell}{dt} = \frac{1}{2} \sum_{i=1}^{\ell-1} \sum_{j=1}^{\ell-1} {}^1\overline{\beta}_{i,j,\ell}\ Q_i Q_j - Q_\ell \sum_{i=1}^{\ell-1}\ {}^2\overline{\beta}_{i,\ell}\ Q_i \\ - \frac{1}{2}\ {}^3\overline{\beta}_{\ell,\ell} Q_\ell^2 - Q_\ell \sum_{i=\ell+1}^{M}\ {}^4\overline{\beta}_{i,\ell}\ Q_i \\ + {}^1G_\ell\ Q_\ell \\ + {}^2G_{\ell+\ell_N}\ Q_{\ell+\ell_N} - {}^2\ G_\ell\ Q_\ell + \delta_{\ell 1} S_l(t) \end{aligned} \tag{29}$$

$$\begin{aligned} \ell_N &= -1 & \quad G(t) > 0 \\ &= +1 & \quad G(t) < 0 \end{aligned}$$

where the $\overline{\beta}$ represent sectional coagulation coefficients, ${}^1G_\ell$ are intra-sectional growth coefficients, ${}^2G_\ell$ are inter-sectional growth coefficients, and S_l (see Eqn. 15) is a particle inception rate (mass units) for the initial size class. The value of the index ℓ_n is determined by whether the net growth is positive or negative, and it is understood that the term containing it will not be present for ℓ=1 for net growth, and will not be present for ℓ=M for net oxidation (G(t) greater or less than zero, respectively). Implicit is the assumption of complete particle coalescence after collision, with no aggregate or chain formation.

Because in the free molecule regime, both the surface growth and coagulation rates are factorable into products of functions of mass times functions of time, a considerable simplification of the task of calculating sectional coefficients is made possible because the mass-dependent calculations need be performed only once, with the time dependence imposed during the course of the integration (e.g. $\overline{\beta} = \overline{\beta}^{(0)} \sqrt{T}$). With the general functional form for the surface growth, the intra-sectional growth coefficients can be calculated analytically as

$$ {}^1G_\ell = 3\Delta_\ell G(t)\left(\frac{1}{m_{\ell-1}^{1/3}} - \frac{1}{m_\ell^{1/3}}\right) \tag{30}$$

and the inter-sectional coefficients are related to these by

$$\begin{aligned} {}^2G_\ell &= {}^1G_\ell \, \frac{\overline{m}_{\ell+1}}{\overline{m}_{\ell+1} - \overline{m}_\ell} & \qquad G(t) > 0 \\ {}^2G_\ell &= {}^1G_\ell \, \frac{\overline{m}_{\ell-1}}{\overline{m}_{\ell-1} - \overline{m}_\ell} & \qquad G(t) > 0 \end{aligned} \tag{31}$$

The inter-sectional coefficients are derived from a number- and mass-conserving algorithm due to Warren and Seinfeld (1985). If some other dependence of surface growth on A is assumed (e.g. $\propto \sqrt{A}$; Fairweather, et al, 1992) a different but easily derived expression for the ${}^1G_\ell$ would be needed. The sectional coalescence coefficients ($\overline{\beta}$) are calculated from the free-molecule collision frequencies, (β) using standard numerical quadratures.

With the solution for the Q_ℓ, a number of aerosol properties can be evaluated. The soot volume fraction will be given by

$$ f_v = \frac{1}{\rho_s} \sum_\ell Q_\ell \tag{32}$$

and its rate of change by

$$ \dot{f}_v = \frac{1}{\rho_s} \sum_\ell {}^1G_\ell Q_\ell = \frac{1}{\rho_s} G'(t) A_T \tag{33}$$

where A_T is the total particle surface area per unit volume (defined below). The moments of the diameter distribution are expressible as

$$< D^n >= \frac{\sum_\ell \int D^n(m) n_\ell(m,t) dm}{\sum_\ell \int n_\ell(m,t) dm} \tag{34}$$

For comparisons with particle diameters obtained from laser light scattering measurements, typically derived by ratioing scattering and extinction, the optical diameter D_{63} is appropriate. This is

$$\begin{aligned} D_{63} &= \left(\frac{< D^6 >}{< D^3 >} \right)^{1/3} \\ &= \left(\left(\frac{6}{\pi \rho_s} \right) \frac{\sum_\ell Q_\ell \Delta_\ell (m_\ell - m_{\ell-1})}{\sum_\ell Q_\ell} \right)^{1/3} \end{aligned} \tag{35}$$

In similar fashion, the total surface area of the particles is given in terms of the Q_ℓ by

$$\begin{aligned} A_T &= \sum_\ell \int_{m_{\ell-1}}^{m_\ell} \pi D^2(m) n_\ell(m,t) dm \\ &= 3\pi \left(\frac{6}{\pi \rho_s} \right)^{2/3} \sum_\ell \Delta_\ell \, Q_\ell \left(\frac{1}{m_\ell^{1/3}} - \frac{1}{m_{\ell-1}^{1/3}} \right) \end{aligned} \tag{36}$$

The soot volume fraction is a quantity of great interest because it is usually the most important soot size/density parameter affecting radiative transfer. It corresponds to the first moment of the suspended mass distribution; the MAEROS algorithm gives a good representation of this moment with a modest number of size classes. The summation over intrasectional growth coefficients leading to the time rate of change of volume fraction will be useful because it permits calculation of the scrubbing or scavenging of gas phase species by particle growth. The analysis described here is not suitable for use at high pressures, because continuum effects could become significant. In such a case, growth and transport coefficients would be determined by interpolation, which would not seriously impair the code's efficiency. The code could also readily accommodate a multicomponent particle analysis (for example, carbon and hydrogen).

2. Transport/Conservation Equations for Particle Sections

The species conservation equation for the n_ℓ in the standard counterflow coordinates (Figure 1) is,

$$\frac{1}{r} \frac{\partial}{\partial r} (r n_\ell u) + \frac{\partial}{\partial z} \left(n_\ell (v + v_T - \frac{D}{n_\ell} \frac{\partial n_\ell}{\partial z}) \right) = \dot{n}_\ell \tag{37}$$

where v_T is the thermophoretic velocity and D the particle diffusion coefficient, respectively. Equation (37) is multiplied by m and integrated over m as in Equation (19), yielding (using $\frac{1}{r}\frac{\partial}{\partial r}(\rho u r) + \frac{\partial}{\partial z}(\rho v) = 0$, and introducing the sectional mass fractions $Y_\ell = \rho Q_\ell$):

$$\rho u \frac{\partial Y_\ell}{\partial r} + \rho v \frac{\partial Y_\ell}{\partial z} + \frac{\partial}{\partial z}\int_{m_{\ell-1}}^{m_\ell} m\left[n_\ell V_T - D\frac{\partial n_\ell}{\partial z}\right] dm = \dot{Q}_\ell \qquad (38)$$

At this point, something must be known about the dependences of v_T and D on particle mass. In the assumed large Knudsen number limit, we have (Waldman, 1966; Friedlander, 1977; Gomez and Rosner, 1994).

$$v_T = \frac{-3}{4}\,(1 + \pi\ \alpha/8)^{-1}\,\left(\frac{\mu}{\rho}\right)\frac{1}{T}\frac{dT}{dz}$$

$$\begin{aligned} D &= \frac{3}{2}\,\frac{kT}{D^2\,\rho\sqrt{\frac{2\pi\ R_g T}{W}}}\,(1 + \pi\ \alpha/8)^{-1} \\ &= \frac{D'}{\rho m^{2/3}} \end{aligned} \qquad (39)$$

where μ is the gas viscosity, and both quantities have an accomodation coefficient α that is near unity. It is seen that v_T is independent of particle size, and D is proportional to $m^{(-2/3)}$. Thus, Equation 38 can be shown to be equal to (in similarity form)

$$-\frac{d}{dz}\,(\rho Y_\ell\,(v_T + v_{D_\ell})) - V\,\frac{dY_\ell}{dz} + \dot{Q}_\ell = 0 \qquad (40)$$

where a mass-weighted mean diffusion coefficient for the size class

$$D_\ell = \frac{\frac{3}{2}D'\left[m_{\ell-1}^{-2/3} - m_\ell^{-2/3}\right]}{\rho \ell n\left(\frac{m_\ell}{m_{\ell-1}}\right)} \qquad (41)$$

and diffusion velocity

$$V_{D_\ell} = -\frac{1}{\rho Y_\ell}\,D_\ell\,\frac{\partial(\rho Y_\ell)}{\partial z} \qquad (42)$$

are employed. The $\dot{Q}_\ell$ yrtm in Equation 40 is the time rate of change due to aerosol dynamical processes, and can be expressed in terms of the Y_ℓ as

$$
\begin{aligned}
\dot{Q}_\ell = \frac{1}{2}\,\rho^2 \sum_i \sum_j {}^{(1)}\overline{\beta}_{ij\ell}\, Y_i Y_j \; - \; \rho^2 Y_\ell \sum_i {}^{(2)}\overline{\beta}_{i\ell} Y_i \\
-\frac{\rho^2}{2}\, {}^{(3)}\beta_{\ell\ell} Y_\ell^2 - \rho^2 Y_\ell \sum_i {}^{(4)}\beta_{i\ell} Y_i + \rho\, {}^{(1)}G_\ell Y_\ell \\
+\rho\, {}^{(2)}G_{\ell+\ell n} Y_{\ell+\ell n} - \rho\, {}^{(2)}G_\ell Y_\ell + \delta_{\ell 1}\, S(r)
\end{aligned}
\tag{43}
$$

where the growth and coagulation coefficients are as derived in the previous section.

F. Scavenging of Gas Phase Species by Particulates

Soot growth and oxidation will deplete local concentrations of growth species like acetylene and benzene, as well as the oxidating species oxygen and hydroxyl radical. It is not strictly correct to assume the soot growth processes represent a perturbation on the gas phase chemistry. Scavenging of these species by particle processes is accounted for in the following way. Because $\rho_s\, \dot{f}_v$ (Equation 33) represents the rate of change of carbon density due to surface growth and oxidation, the quantities

$$
\begin{aligned}
S_G &= \left(\frac{R_G}{R_G - R_{O_2} - R_{OH}}\right) \rho_s\, \dot{f}_v \\
S_{O_2} &= \left(\frac{R_{O_2}}{R_G - R_{O_2} - R_{OH}}\right) \rho_s\, \dot{f}_v \\
S_{OH} &= \left(\frac{R_{OH}}{R_G - R_{O_2} - R_{OH}}\right) \rho_s\, \dot{f}_v
\end{aligned}
\tag{44}
$$

represent sources and sinks of solid carbon.

For the Harris-Weiner growth rate assumed in the sample calculations to follow, the chemical equation can be represented by

$$
C_2H_2 + \text{soot} \rightarrow [\text{soot} + 2C(s)] + H_2 \tag{45}
$$

and for the oxidative processes

$$
\begin{aligned}
O_2 + \text{soot} &\rightarrow [\text{soot} - C(s)] + O + CO \\
OH + \text{soot} &\rightarrow [\text{soot} - C(s)] + H + CO
\end{aligned}
\tag{46}
$$

Stoichiometric coefficients ($\nu_K^{(G)}$, ...) can be assigned to the participating species, and molar rates of change calculated from

$$W_k \dot{w}_k^s = \nu_k^{(G)} S_G + \nu_k^{(O_2)} S_{O_2} + \nu_k^{(OH)} S_{OH} \qquad (47)$$

In a similar way, an overall chemical equation can be written for the assumed inception process, and gaseous species depletion rates calculated from the inception rate S_i (Equation 15).

III. Computational Results

Sample calculations were performed for room temperature, opposed jets of undiluted methane and air at one atmosphere. Plug flow boundary conditions (Kee, et al., 1988) are employed for velocity profiles in these calculations. These boundary conditions provide a reasonable approximation for some experimental flame conditions (Chelliah, et. al., 1990). Table II gives the base case flow parameters, and default values of other growth parameters. Fifteen sections were chosen for base calculations because accurate soot number densities and average sizes were desired; it will be shown, however, that accurate total volume fractions can be achieved with far fewer sections. The aim of these sample calculations is to demonstrate the capabilities of the program, and to undertake systematic variations that yield more understanding of the complex interactions of parameters important to soot formation. There is still considerable uncertainty surrounding the proper treatment of inception and surface growth, and the focus at this time is on qualitative comparisons.

Table II
Base Case Parameters

V_{edge} = -0.0105 gm/cm^2/sec (Y_{N2} = .77, Y_{O2} = .23)
V_{wall} = .0208 gm/cm^2/sec (Y_{CH4} = 1.0)
$T_{edge} = T_{wall}$ = 298 K
a = 17.2 sec^{-1}
T_{max} = 2000 K
M = 15
PR = 1.5
Surface Growth = HW

Calculated gas phase species profiles for the base case are shown in Figure 2. The major growth and oxidative species are shown, as well as species like CO and H_2 that can be formed from growth and oxidation. Oxygen diffuses to the fuel side of the flame, and is present at levels sufficient to affect soot growth, as will be discussed. The effect of increasing strain rate by roughly a factor of five is shown in Figure 3. While acetylene is not strongly affected, the shorter residence times lead to reduced benzene, as seen. In the absence of thermal radiation, peak temperatures would decrease monotonically with increasing strain rate. With radiation included, peak temperatures are relatively flat over the range of strain rates considered here (13 to 78 sec^{-1}). The higher spatial gradients in the high strain rate case lead to much higher oxygen concentrations.

The calculated evolution of the total volume fraction and the profiles of the sections are shown in Figure 4. The average size of the sections is shown in nanometers. Evolution toward larger mass particles occurs due to surface growth and coalescence. The low sections appear in the vicinity of the acetylene peak, but never acquire an appreciable fraction of the soot mass. Most of the soot growth occurs in a narrow range between about 0.5 to 0.8 in the normalized flow coordinate. Falling temperature, acetylene, and benzene concentrations give rise to rapid reductions in surface growth rates as the stagnation plane is approached. As the particles grow, convection and thermophoresis push them in the direction of the stagnation plane. At the stagnation plane, thermophoresis causes some spilling of large particles to the fuel side of the plane, but convection pushes them back. A balance between convection and thermophoresis leads to a peak on the fuel side of the stagnation plane. The population of bins above $M = 10$ is negligible and is not shown. Cases with high volume fractions present in the largest bin should be rerun with an increased setting for the upper limit of the soot size range. For extremely low values of strain rate where residence times are long and coalescence has much time to promote particles to large sizes, adjustment sometimes has to be made. As will be discussed, Figure 4 represents exactly the form of the soot volume fraction distribution that is observed in experiments.

Figure 5 shows the evolution of the soot mass distribution, with particle mass as the independent variable, with distance from the flame. As the distribution evolves toward the stagnation plane, it takes on the form of a self- preserving distribution, but always has some degree of bimodality, with a secondary peak arising from inception. A self-preserving form is indicative of a coalescence- dominated dynamical process (Friedlander, 1977). Coalescence plays an important role in determining soot yield because, although it is mass-conserving, it is destructive of surface area, and thus reduces the contributions of surface growth. Previous calculations (Colket, et. al., 1991) indicated that these distributions were close to self-preserving form for 0.12 - 1.0 atmosphere premixed flames.

Figure 6 displays the velocity, velocity gradient, and temperature profiles for the base case. The strain rate, following Chelliah, et. al. (1990), has been taken from the one-half velocity gradient at the stagnation plane. These flames are relatively thick, affording the long residence times needed for soot formation and significant radiation effects.

Division of the source and sink terms for growth and oxidation by the total soot surface area leads to specific rates for these processes in units of cm/sec, shown in Figure 7. The Harris-Weiner (HW), Frenklach-Wang (FW), and modified Frenklach-Wang (MODFW) surface growth rates have been discussed previously. When these are compared with oxidation, it is apparent that only the Harris-Weiner expression results in significant net surface growth. The MODFW expression for growth is never in excess of oxidation, and the FW expression ($\alpha = 1$)is only marginally so in a restricted region. Near the flame front (peak temperature regime), the FW mechanism predicts significant growth rates because of increased temperature and the rise in concentrations of H-atoms. However, oxidation rates (by OH and O_2) by far dominate this growth expression. Calculations including Soret diffusion did not alter the H-atom profile enough to change any of these conclusions.

Inclusion of radiation from gas bands and soot depresses peak temperature by about 70 K for the base strain rate. This is a cooling effect of about 3.5%, and probably represents about 7% conversion of flame enthalpy to radiation, the variation of the latter with temperature being nonlinear (Vranos and Hall, 1993). This is large enough to perturb significantly the soot growth species benzene and acetylene, as shown in Figure 8. The consequence of this is a marked sensitivity of volume fraction to radiation, as seen in Figure 9. Without radiation, the predicted volume fraction is nearly a factor of three higher. The higher soot production with higher temperatures in a diffusion flame is consistent with the phenomenological understanding provided by Glassman (1988). This arises not just from the increased levels of acetylene and benzene shown in Figure 8, but also from the Arrhenius terms in the inception and surface growth expressions. Radiation effects should decrease monotonically with increasing strain rate, as the flames become thinner and there is less residence time for radiation. This very strong sensitivity of radiation on soot predictions is consistent with results of Sivathanu and Gore (1993). Thus accurate calculations of radiation phenomena is a key ingredient in the prediction of soot profiles in flames. Most of the radiative gas cooling is actually due in this case to gas bands, because the soot radiation temperature is relatively low. In cases with higher soot volume fraction, soot radiation would play a greater role (see, for example, Figure 16).

In the radiative power density formulation, Equation 7, the soot radiative constant C and the integrated gas band intensities (particularly that of the 4.3 micron CO_2 band) were made consistent with Grosshandler (1993). The long-wavelength H_2O and CO_2 bands were ignored. The low strain rate flames are thick enough (Figure 6) that self-absorption effects might be significant (Hall, 1994). The analysis of such optical thickness effects is computationally intensive, however, and has been deferred to future studies.

Figure 9 also shows the importance of oxidation. Suppressing it entirely results in the increase in volume fraction shown. Oxidation in the soot growth region is mainly due to molecular oxygen. Suppressing thermophoresis results in increased soot, as also shown. Thermophoresis lowers the residence time in the growth region, and thus reduces soot yield. Without thermophoresis, there is no spilling of particles to the fuel side of the stagnation plane. While thermophoresis plays an important role, it appears that ordinary diffusion does not; setting the sectional diffusivities equal to zero results in very little change.

Figures 10 and 11 show the analogous effects on particle number density and average size. Because the rate of inception is strongly affected by temperature, removing radiative loss results in much higher levels of particles, at least towards the inception region. Near the stagnation plane, there is less difference in number density, presumably due to a loss of sensitivity to *initial conditions* in a coalescence-dominated regime. Number density is decreasing toward the stagnation plane, of course, because of coalescence. Figure 11 shows interesting effects on the average particle size, which is the optical diameter D_{63} discussed earlier. More rapid surface growth resulting from removal of radiation, and faster coalescence from higher number densities results in much larger particles, as seen. The particles that do penetrate to the fuel side of the stagnation plane evidently do not further coalesce; the number densities and collision frequencies are too low for this to proceed on a reasonable time scale. Without thermophoresis, the particles have more time to grow to a larger size at the stagnation plane, as seen.

Variation of strain rate leads to the set of curves shown in Figure 12. Plotted versus the reduced coordinate, the total volume fractions seem to have the form of a similarity solution. It has been mentioned that the peak temperatures are relatively flat with strain rate because of the effects of radiation. Decreasing benzene and increasing oxygen with increasing strain rate are factors in the fall-off of volume fraction, but the main factor is probably residence time. There is simply less time for surface growth to occur at high strain rate. The combined effect is to produce an order of magnitude less soot with a variation of strain rate of about six.

Qualitative comparisons with the data of Zhang, Atreya, and Lee (1992) are quite satisfactory, most notably in the way the model reproduces the profile of the volume fraction profile, and the accumulation of soot at the stagnation plane. Quantitative comparisons have not been attempted because non-zero temperature gradients at the boundary in the experiment is inconsistent with the modeling assumptions.

Because the surface growth rate is uncertain, a set of variations in which the nominal HW rate was multiplied by factors of 2^n, where n takes on positive and negative values. This is seen in Figure 14. For very large enhancements of the base rate, the predicted soot yield begins to saturate because the conversion of fuel carbon to soot becomes large. This may be a trivial effect, reflecting just the depletion of the available carbon pool. There is much more relative sensitivity at lower rates. This is further exhibited in Figure 15. If scrubbing of acetylene is removed, the soot volume fraction grows by a large factor. In the large surface growth limit, the predicted volume fraction also loses sensitivity to inception rate, as shown by the curve in which the base inception has been divided by the same factor. In this case, the number density is markedly reduced in the inception region, but, together with average size, is not much different at the stagnation plane. The latter effect possibly is also attributable to a loss of sensitivity to initial conditions in a coalescence-dominated limit. The loss of sensitivity to inception rate in high growth systems is consistent with the result of Kennedy, et al. (1990). Lower surface growth rates show much more sensitivity to inception rate; since, in such cases, predicted soot volume fractions are nearly proportional to inception rates.

The effect on temperature of many of these effects that have been discussed is shown in Figure 16. The elevation of peak temperature by removal of radiation discussed earlier is shown. Enhancement of base surface growth results in further temperature reduction because soot formation and thus soot radiation are enhanced. Repeating the enhanced surface growth calculation without the gas phase scrubbing results in further temperature reduction because of even higher soot levels and higher radiation. The cooling in the no-scrubbing case is mitigated to some degree by removal of the exothermic surface growth process.

Enhanced surface growth with scrubbing of gas phase species leads to the significant reduction in the concentrations of benzene and acetylene shown in Figure 17. Removal of scrubbing allows these species to restore themselves, although these 'restored' values are less than what they would have been if temperature suppression caused by increased radiation was not included. The oxygen profile shows similar dramatic effects. Enhanced surface growth leads to enhanced surface area, and depletion of oxygen relative to its no scrubbing profile. Suppression of scrubbing restores oxygen to values higher than its base (non-enhanced surface growth) profile, because of lower temperatures due to enhanced soot radiation. Comparisons in Figures 15, 16 and 17 provide mple of the complex interaction and interdependency of gas-phase species, particulates, bulk temperature, and radiation. Solutions of one parameter, without taking into account effects due to other processes, can be in error significantly.

The sectional representation is highly efficient at predicting soot volume fraction, usually the soot parameter of most interest, with just a few sections. Figure 18(a) shows how the base case volume fraction profile varies with number of sections. For $M > 3$, there is no significant sensitivity to M! (Strictly speaking, $M = 2$ may not be a good choice since one would probably be violating the requirement that significant soot mass not accumulate in the highest section). The solutions for $M \geq 5$ are virtually indistinguishable. Since most of the soot mass is due to surface growth, this means that total soot surface area is being accurately represented by just a few sections, as well. The extra calculational burden imposed by M sectional equations is not significant, and the sectional coefficient calculations do not impose a significant burden regardless of the value of M. Run time to convergence has more to do with the accuracy of the starting solution than with the number of sections. Accurate values of average particle size or number density cannot be expected from so few sections, however, as shown for the average size in Figure 18(b). Fifteen to twenty sections are required to converge on size or number density. This result is consistent with studies on premixed flames (Colket and Hall, 1994).

IV. Conclusions/Summary

A new tool for studying soot formation in opposed jet diffusion flames has been developed by coupling the dynamical sectional equations for spheroid growth with the conservation equations and complex chemistry of counterflow diffusion flames. The particle kinetics include inception, surface growth and oxidation, and coalescence within the framework of the discrete size spectrum, or sectional representation. The results of this analysis indicate that the particle growth dynamics and transport, gas phase chemistry, flame radiation and flow hydrodynamics are all strongly coupled. Particle inception and surface growth oxidation are calculated from local values of the major growth/oxidation species benzene, acetylene, oxygen, and hydroxyl radical which have been calculated from complex chemical mechanisms. Scrubbing of gaseous species by the particles is included in the species and energy conservation equations, to account for effects of soot growth and oxidation. Particle transport by thermophoresis and diffusion with an effective sectional diffusion coefficient have been included. Non-adiabatic radiative loss by gas and particle emission is also coupled to the flow energy equation. Qualitatively, predictions are in good agreement with observations of soot growth in these flames; soot is predicted to appear first on the fuel rich side of the flame near the benzene/acetylene peak, and to accumulate in the vicinity of the stagnation plane. Application of the program to methane-air flames has shown a strong coupling of thermal radiation and soot growth as gas cooling reduces the concentrations of benzene and acetylene, and affects Arrhenius factors in the inception and surface growth expressions. For strong surface growth, predicted soot parameters become somewhat insensitive to inception. Thermophoresis is shown to reduce local soot yields by reducing particle residence time in high surface growth regions. For high surface growth, depletion of gas phase growth species is shown to be important for quantitative prediction of soot growth. For nominal surface growth rates, oxidation is shown to play a non-negligible role. The algorithm is shown to be highly efficient for predictions of soot volume fraction, with accurate solutions obtained for as few as two or three size classes. Accurate predictions of average particle size or number density require larger numbers of sections. The work marks the first time that the sectional growth equations widely used in aerosol science have been coupled to the solution algorithms for counterflow diffusion flames that are important in combustion science. The code will provide a framework for evaluation of proposed surface growth and inception models as well-posed experimental data become available.

ACKNOWLEDGEMENTS

This work has been supported in part by the Air Force Office of Scientific Research (AFSC) under Contract Nos. F49620-88-C-0051 and F49620-91-C-0056. The United States Government is authorized to reproduce and distribute reprints for governmental purposes notwithstanding any copyright notation hereon. The encouragement and support by Dr. J. Tishkoff is greatly appreciated. Computational assistance from Mr. W. Proscia and Ms. H. Hollick facilitated completion of this work. The authors are indebted to Ms. K. Wicks for her substantial efforts in manuscript and figure preparation.

Most important, the guidance, inspiration, and support from Professor I. Glassman as a teacher, as a mentor and finally as a colleague are warmly recognized.

Appendix A. Boundary Value Problem Solution Algorithm

Complete specification of the problem posed by Equations 1-7 requires that boundary conditions be imposed at each end of the computational domain $0<z<L$. At $z=0$ (the fuel jet), we have

$$V = \rho_f v_f \tag{A1}$$

$$U = 0 \tag{A2}$$

$$Y_k = Y_{kf}, \ k = 1,2,\ldots,K \tag{A3}$$

$$Y_k = 0, \ k = K+1, K+2, \ldots, K+M \tag{A4}$$

$$T = T_f \tag{A5}$$

and at $z=L$ (the oxidizer jet), we have

$$V = \rho_{ox} v_{ox} \tag{A6}$$

$$U = 0 \tag{A7}$$

$$Y_k = Y_{k_{ox}}, \ k = 1,2,\ldots,K \tag{A8}$$

$$Y_k = 0, \ k = K+1, K+2, \ldots, K+M \tag{A9}$$

$$T = T_{ox} \tag{A10}$$

where T_f and T_{ox} are the specified temperatures in the fuel and ozidizer streams; Y_{k_f} and $Y_{k_{ox}}$ are the specified mass fractions in the fuel and oxidizer streams and $\rho_f v_f = V_{edge}$ and $\rho_{ox} v_{ox} = V_{wall}$ are the mass ejection rates from the fuel and oxidizer jets. By specifying the value of V at the two jet surfaces the problem is overspecified since the continuity equation is first-order in space. To maintain a well posed problem the equation

$$\frac{dJ}{dz} = 0 \tag{A11}$$

is introduced and J solved for as an eigenvalue. It is worthwhile to note that in the above formulation the strain rate does not appear explicitly in the governing equations. The magnitude of the reduced pressure gradient J is related to the "stretch" in the flame due to the imposed flow. As the magnitude of J increases, so does the strain rate. As a result, in the discussion that follows, the two quantities are used interchangeably. Strictly speaking, the strain rate could be computed directly from derivatives of the axial or radial velocity fields.

Equations 1-7, A1-A11 form a nonlinear two-point boundary value problem. The solution procedure employs a combination of time-integration and an adaptive finite difference method to obtain profiles for the dependent variables. The method has been discussed in detail elsewhere (see, e.g., Smooke (1982) and Smooke et al. (1983,1986)) and only the essential features are outlined here. The goal is to obtain a discrete solution of the governing equations on the mesh $\mathcal{M}$

$$\mathcal{M} = \{0 = z_0 < z_1 < \ldots < z_m = L\} \tag{A12}$$

When the continuous differential operators are replaced by finite difference expressions, the problem of finding an analytic solution of the governing equations is converted into one of finding an approximation to this solution at each point of the mesh $\mathcal{M}$. Upon writing the discrete equations in residual form, we seek the solution U^* of the nonlinear system of difference equations

$$F(U) = 0 \tag{A13}$$

Assuming we can obtain an initial solution estimate U^0 that is sufficiently "close" to U^*, the system of equations in (A13) can be solved by Newton's method. We write

$$J(U^k)\,(U^{k+1} - U^k) = -\lambda_k F(U^k), \quad k = 0, 1, \ldots \tag{A14}$$

where U^k denotes the k^{th} solution iterate, λ_k the k^{th} damping parameter (Deuflhard, 1974) $(0 < \lambda \leq 1)$ and $J(U^k) = \partial F(U^k)/\partial U$ the Jacobian matrix. A system of linear block tridiagonal equations must be solved at each iteration for corrections to the previous solution vector. As we found in the solution of burner-stabilized and freely propagating premixed laminar flames, the cost of forming (we use a numerical Jacobian) and factoring the Jacobian matrix can be a significant part of the cost of the total calculation. In such problems, a modified Newton method is applied in which the Jacobian is re-evaluated periodically. An error estimate that enables one to determined when to form a new Jacobian is contained in Smooke (1983).

The solution of combustion problems, such as the counterflow diffusion flame, requires that the computational mesh be determined adaptively. The mesh $\mathcal{M}$ is equally distributed on the interval $[0, L]$ with respect to the non-negative function W and the constant C. Specifically, the mesh is formed by employing a weight function that equidistributes the difference in the components of the discrete solution and its gradient between adjacent mesh points. Upon denoting the vector of $N = K + 4 + M$ dependent solution components by $\tilde{U} = [\tilde{U}_1, \tilde{U}_2, \ldots, \tilde{U}_N]^T$, we seek a mesh $\mathcal{M}$ such that

$$\int_{z_j}^{z_{j+1}} \left|\frac{d\tilde{U}_i}{dz}\right| dz \quad \leq \quad \delta \left| \max_{0\leq z\leq L} \tilde{U}_i - \min_{0\leq z\leq L} \tilde{U}_i \right| \qquad \begin{array}{c} j = 0, 1, \ldots, m-1 \\ i = 1, 2, \ldots, N \end{array} \tag{A15}$$

and

$$\int_{z_j}^{z_{j+1}} \left|\frac{d^2\tilde{U}_i}{dz^2}\right| dz \quad \leq \quad \gamma \left| \max_{0\leq z\leq L} \frac{d\tilde{U}_i}{dz} - \min_{0\leq z\leq L} \frac{d\tilde{U}_i}{dz} \right| \qquad \begin{array}{c} j = 1, 2, \ldots, m-1 \\ i = 1, 2, \ldots, N \end{array} \tag{A16}$$

where δ and γ are small numbers less than one and the maximum and minimum values of $\tilde{U}_i$ and $d\tilde{U}_i/dz$ are obtained from a converged numerical solution on a previously determined mesh.

Determination of a "good" initial estimate for U^0 can be extremely difficult for counterflow problems. The difficulty is due to the exponential dependence of the chemistry terms on the temperature and to the nonlinear coupling between the fluid and thermochemistry solution fields. To alleviate this situation, we utilize a flame sheet starting procedure in which the equations of mass and momentum are coupled with a Shvab-Zeldovich equation to provide estimates for the mass flux in the transverse direction, the similarity function, the temperature and the stable major gas phase species in the flame (Keyes and Smooke, 1987). Gaussian profiles are used for the minor gas phase species and the soot size classes. This starting estimate is then integrated in time until the solution lies in the convergence domain of Newton's method on the initial grid. The size of the time steps is chosen adaptively by monitoring the local truncation error of the time discretization. Time integration and Newton's method are also employed on subsequently refined grids.

REFERENCES

Barfknecht, T. R. (1983). *Prog. Energy Combust. Sci.* **9**, 199.

Bhattacharjee, S. and Grosshandler, W.L. (1988). Effect of Radiative Heat Transfer on Combustion Chamber Flows, presented at *Western States Sectional Meeting of Combustion Institute,* Salt Lake City.

Bittker, D. (1991). *Comb. Sci. Tech.* **79**, 49.

Chelliah, H.K., Law, C.K., Ueda, T., Smooke, M.D., and Williams, F.A. (1990). *Twenty-third Symposium (International) on Combustion/The Combustion Institute*, pp. 503-511.

Colket, M.B. and Hall, R.J. (1994). *Proceedings of the International Workshop on Mechanisms and Models of Soot Formation* (H. Bockhorn, Ed.), Springer-Verlag, Heidelberg.

Colket, M.B., and Smooke, M.D. (1993). *The Formation of Benzene from Methane,* presentation at joint Central/Eastern States Section of the Combustion Institute, New Orleans, LA.

Dasch, C.J. (1985). *Comb. Flame* **61**, 219.

Deuflhard, P. (1974). *Numer. Math.* **22**, 289.

Fairweather, M., Jones, W.P., and Lindstedt, R.P., (1992). *Combust. Flame* **89**, 45.

Frenklach, M., Clary, D. W., Gardiner, W. C., and Stein, S. E. (1985). *Twentieth Symposium (International) on Combustion/The Combustion Institute*, pp. 887-901.

Frenklach, M., and Warnatz, J. (1987). *Combust. Sci. Tech.* **51**, 265.

Frenklach, M. (1988). *Twenty-Second Symposium (International) on Combustion/The Combustion Institute*, p. 1075.

Frenklach, M. and Wang, H. (1990). *Twenty-third Symposium (International) on Combustion/The Combustion Institute,* p. 1559.

Friedlander, S.K. (1977). *Smoke, Duct and Haze*, Wiley, p. 31.

Gelbard, F. (1982). MAEROS User Manual, NUREG/CR-1391, (SAND80-0822).

Gelbard F. and Seinfield, J. H. (1980). *J. Coll. Int. Sci.* **78**, 485.

Gelbard, F., Tambour, Y. and Seinfield, J.H. (1980). *J. Coll. Int. Sci.* **76**, 54.

Giovangigli, V., and Darabiha, N. (1988). "Vector Computers and Complex Chemistry Combustion," in : Proceedings of the Conference on Mathematical Modeling in Combustion, Lyon, France, NATO ASI Series E140.

Glarborg, P., Miller, J. A., and Kee, R. J. (1986). *Comb. Flame* **65**, 177.

Glassman, I. (1988). *Twenty-Second Symposium (International) on Combustion/The Combustion Institute*, pp. 295-311.

Gomez S. and Rosner, D. (1993). *Comb. Sci. Tech.* **84**, 335.

Grosshandler, W. L. (1993). *RADCAL: A Narrow-Band Model for Radiation Calculations in a Combustion Environment*, NIST Technical Note 1402.

Hall, R.J. (1993). *JQSRT* **49**, 517.

Hall, R.J. (1994). to appear in *JQSRT*.

Hall, R. J. and Bonczyk, P. A. (1991). *Applied Optics* **29**, 4590.

Harris, S. J. and Weiner, A. M. (1983). *Comb. Sci. Tech.* **31**, 155.

Haynes, B. S. and Wagner, H. G. (1981). *Prog. Energy Combust. Sci.* **7**, 229.

Hura, H. S. and Glassman, I. (1988). *Twenty-Second Symposium (International) on Combustion/The Combustion Institute* p. 371.

Kee, R. J., Miller, J. A., Evans, G.H. and Dixon-Lewis, G. (1988). *Twenty-second Symposium (International) on Combustion/The Combustion Institute*, pp. 1479-1494.

Kennedy, I. M., Kollmann, W., and Chen, J. Y. (1990). *Combust. Flame* **81**, 73.

Kern, R. D., Singh, H. J., and Wu, C. H. (1988). *Int. J. Chem. Kin.* **20**, 781.

Keyes, D. E. and Smooke, M. D. (1987). *J. Comp. Phys.*, **73**, 267.

Leung, K. M., Lindstedt, R. P., and Jones, W. P. (1991). *Combust. Flame* **87**, 289.

Lindstedt, R. P. and Skevis, G. (1994). Division of Fuel Chemistry Preprint, annual meeting of the American Chemical Society, San Diego, Mar 13-17, Vol.39 , No. 1, pp.147-151.

Markatou, P., Wang, H., and Frenklach, M. (1993). *Combust. Flame* **93**, 467.

Markstein, G.H. (1984). *Proceedings, Twentieth International Symposium on Combustion/The Combustion Institute*, pp. 1055-1061.

Miller, J. A. and Melius, C. F. (1992). *Combust. Flame* **91**, 21.

Nagle, J. and Strickland-Constable, R.F. (1963). *Proceedings of the Fifth Carbon Conference*, Vol. 1, Pergamon Press, p. 154.

Neoh, K. G., Howard, J. B., and Sarofim, A. F. (1981). *Particulate Carbon: Formation During Combustion* D. C. Seigla and G. W. Smith, eds. Plenum, New York, p. 261.

Sivathanu, Y. R. and Gore, J.P. (1994). *Combust. Flame* **97**, 161.

Smith, O. I., (1981). *Prog. Energy Combust. Sci.* **7**, 275.

Smooke, M. D. (1982). *J. Comp. Phys.* **48**, 72.

Smooke, M. D. (1983). *J. Opt. Theory and Appl.* **39**, 489.

Smooke, M. D., Miller, J. A. and Kee, R. J. (1983). *Comb. Sci. and Tech.* **34**, p. 79.

Smooke, M. D., Puri, I. K. and Seshadri, K. (1986). *Twenty-First Symposium (International) on Combustion/The Combustion Institute,* 1783.

Smooke, M. D. and Giovangigli, V. (1992). *Twenty Fourth Symposium International on Combustion/The Combustion Institute,* 161.

Smooke, M. D., Xu, Y., Zurn, R.M., Lin, P., Frank, J.H. and Long, M.B. (1992). *Twenty-fourth Symposium (International) on Combustion/The Combustion Institute*, p. 813.

Vranos, A. and Hall, R.J. (1993). *Combust. Flame* **93**, 230.

Wagner, H. G. (1979) *Seventeenth Symposium (International) on Combustion/The Combustion Institute*, pp. 3-19.

Waldmann, L. (1966). Thermophoresis and Diffusiophoresis of Aerosols, *Aerosol Science*, (C.N. Davies Ed.), Academic Press, 140.

Warren, D.R. and Seinfeld, J.H. (1985). *Aerosol Sci. Tech.* **4**, 31.

Zhang, C., Atreya, A., and Lee, K. (1992). *Twenty-First Symposium (International) on Combustion/The Combustion Institute*, pp. 1049-1057.

FIGURE CAPTIONS

Figure 1. Coordinate System for Opposed Jet Diffusion Flame.

Figure 2. Species Profiles for Base Case ($a_{max} = 17.2$ sec$^{(-1)}$).

Figure 3. Species Profiles for Highest Strain Rate Case. ($a_{max} = 78$ sec$^{(-1)}$).

Figure 4. Spatial Evolution of Size Classes.

Figure 5. Evolution of Soot Mass Distribution (spatial locations given in table).

Figure 6. Velocity, Strain Rate, and Temperature Profiles for Base Case.

Figure 7. Comparison of Surface Growth Models, with Oxidation Rate for Base Case.

Figure 8. Radiation Effects on Growth and Oxidation Species.

Figure 9. Effect of Radiation, Oxidation, and Thermophoresis on Soot Volume Fractions

Figure 10. Effect of Radiation, Oxidation, and Thermophoresis on Particle Number Density.

Figure 11. Effect of Radiation, Oxidation, and Thermophoresis on Average Particle Size.

Figure 12. Variation of Volume Fraction with Strain Rate.

Figure 13. Experimental Soot Distributions and Number Densities in Methane Opposed jet Flames. Taken from Figure 6 of Zhang, Atreya, and Lee (1992). The different symbols show the effects of diluents. $Z_n = z', \phi = f_v$.

Figure 14. Effects of Surface Growth Augmentation. NX indicates multiplication of base surface growth rate by factor N, inception unchanged.

Figure 15. Effects of Scavenging and Inception Sensitivity at High Surface Growth. NX/M denotes simultaneous multiplication of base surface growth by factor N, and division of base inception rate by factor M.

Figure 16. Effect of Radiation, Enhanced Soot Growth, and Scavenging on Temperature Profile.

Figure 17. Effect of Enhanced Surface Growth and Scavenging on Gas Phase Species.

Figure 18. Sensitivity of Volume Fraction (a) and Average Particle Size (b) to Number of Sections.

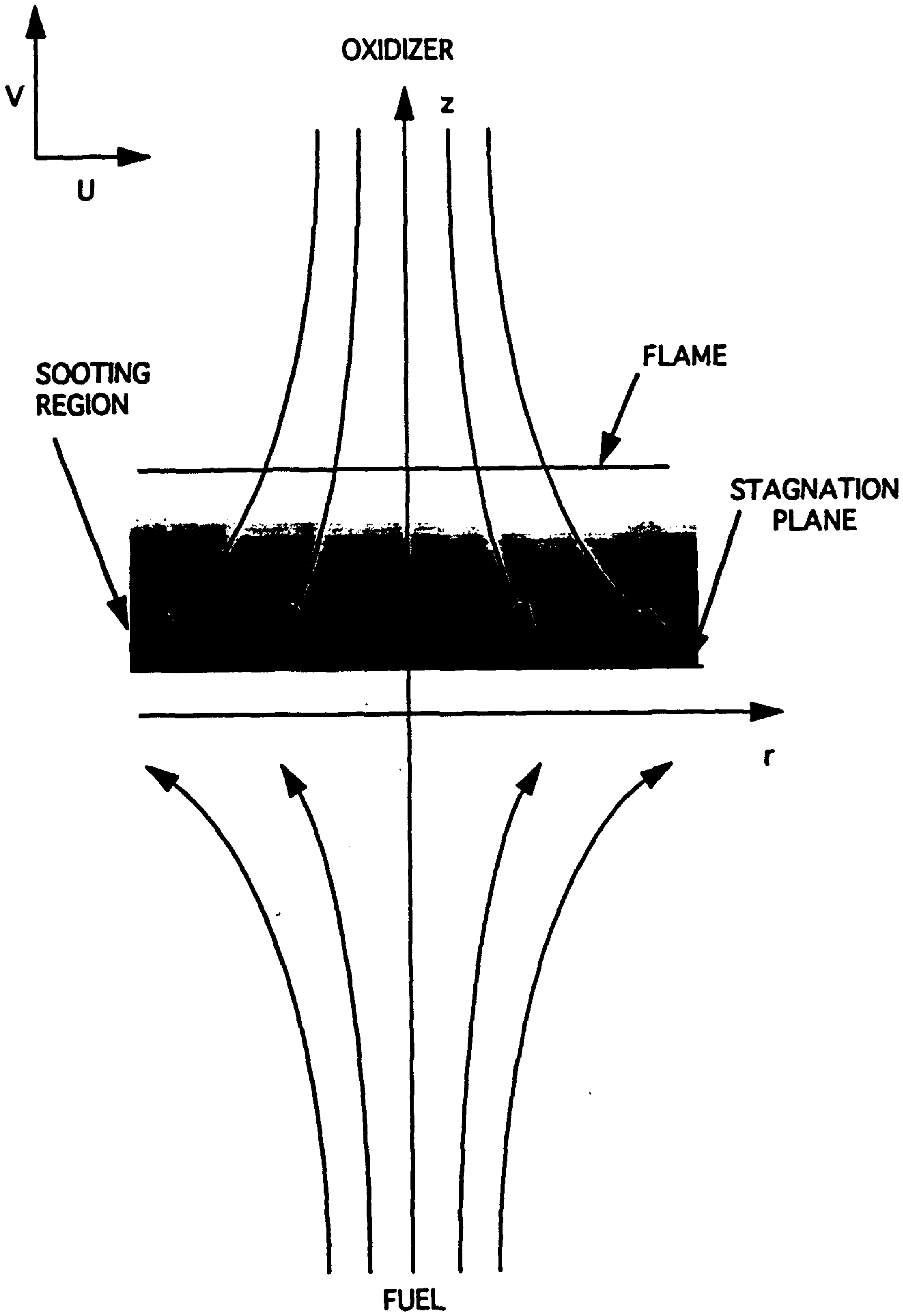
V
U
OXIDIZER
z
FLAME
SOOTING
REGION
STAGNATION
PLANE
r
FUEL

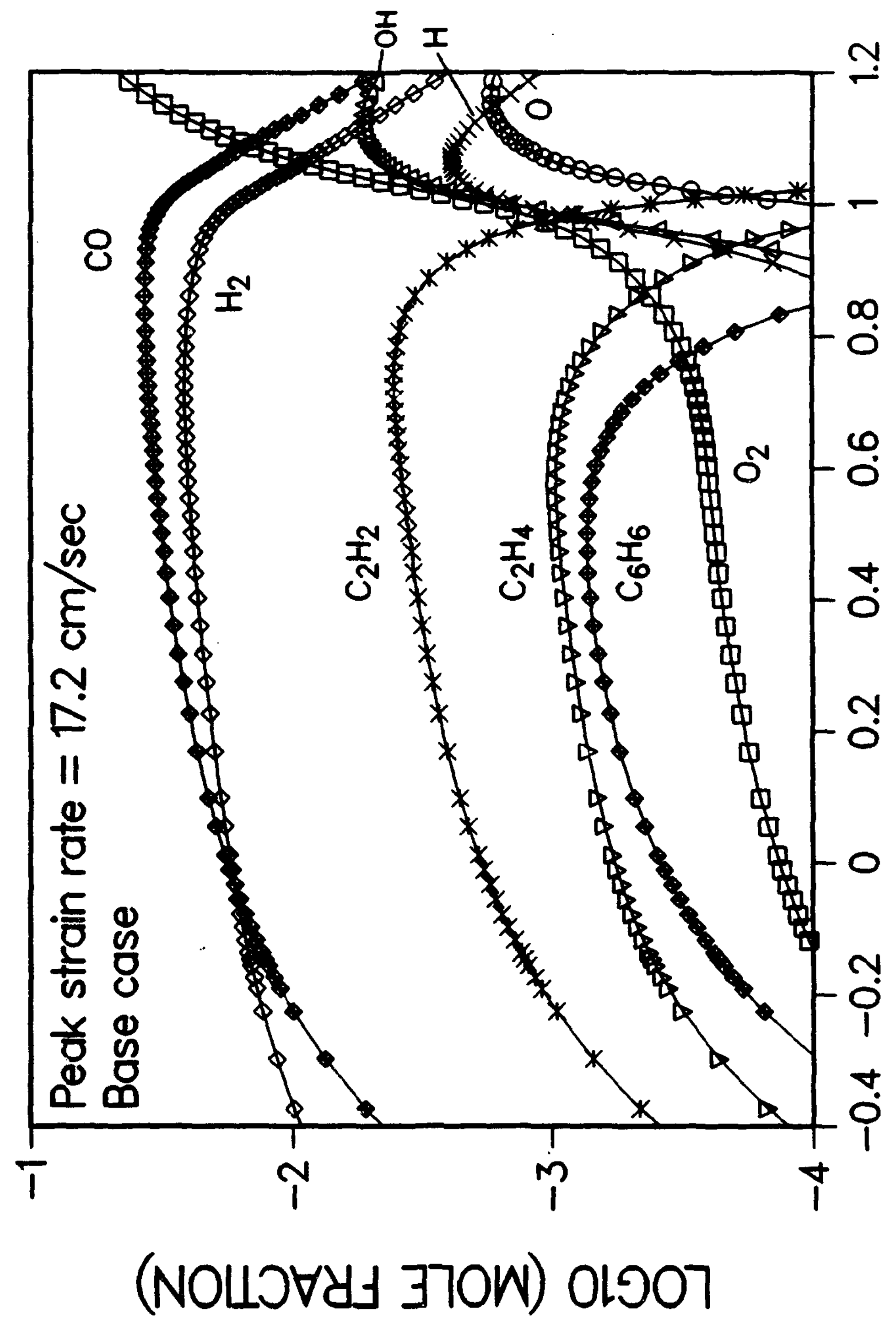
Peak strain rate = 17.2 cm/sec
Base case
CO
H$_2$
C$_2$H$_2$
C$_2$H$_4$
C$_6$H$_6$
O$_2$
OH
H
O
Z'
LOG10 (MOLE FRACTION)
−1
−2
−3
−4
−0.4
−0.2
0
0.2
0.4
0.6
0.8
1
1.2

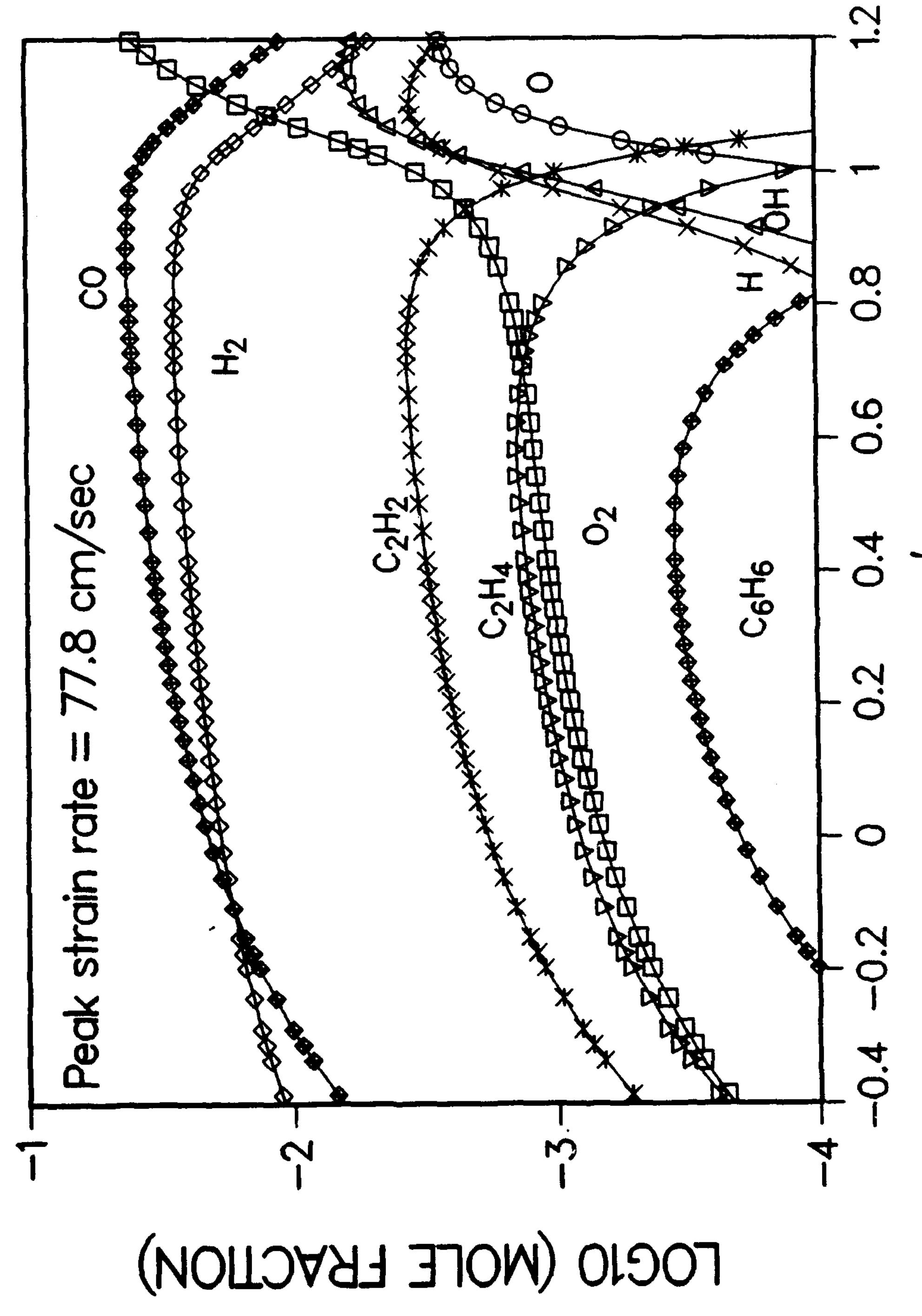

Peak strain rate = 77.8 cm/sec
CO
H$_2$
C$_2$H$_2$
C$_2$H$_4$
O$_2$
C$_6$H$_6$
O
OH
H
-0.4
-0.2
0
0.2
0.4
0.6
0.8
1
1.2
Z'
-1
-2
-3
-4
LOG10 (MOLE FRACTION)

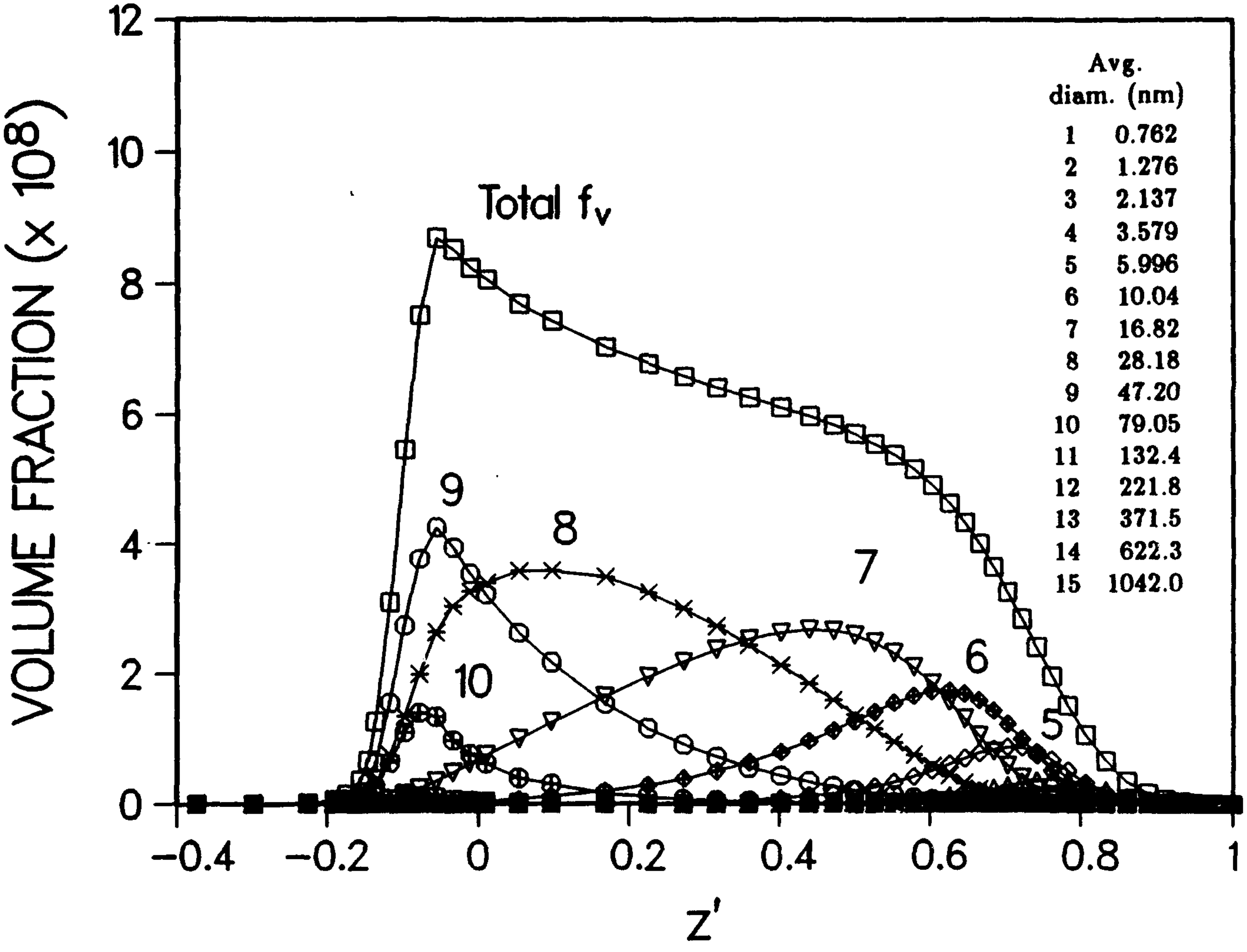
VOLUME FRACTION (x 10^8)
12
10
8
6
4
2
0
-0.4
-0.2
0
0.2
0.4
0.6
0.8
1
z'
Total f_v
9
8
7
6
5
10
Avg.
diam. (nm)
1 0.762
2 1.276
3 2.137
4 3.579
5 5.996
6 10.04
7 16.82
8 28.18
9 47.20
10 79.05
11 132.4
12 221.8
13 371.5
14 622.3
15 1042.0

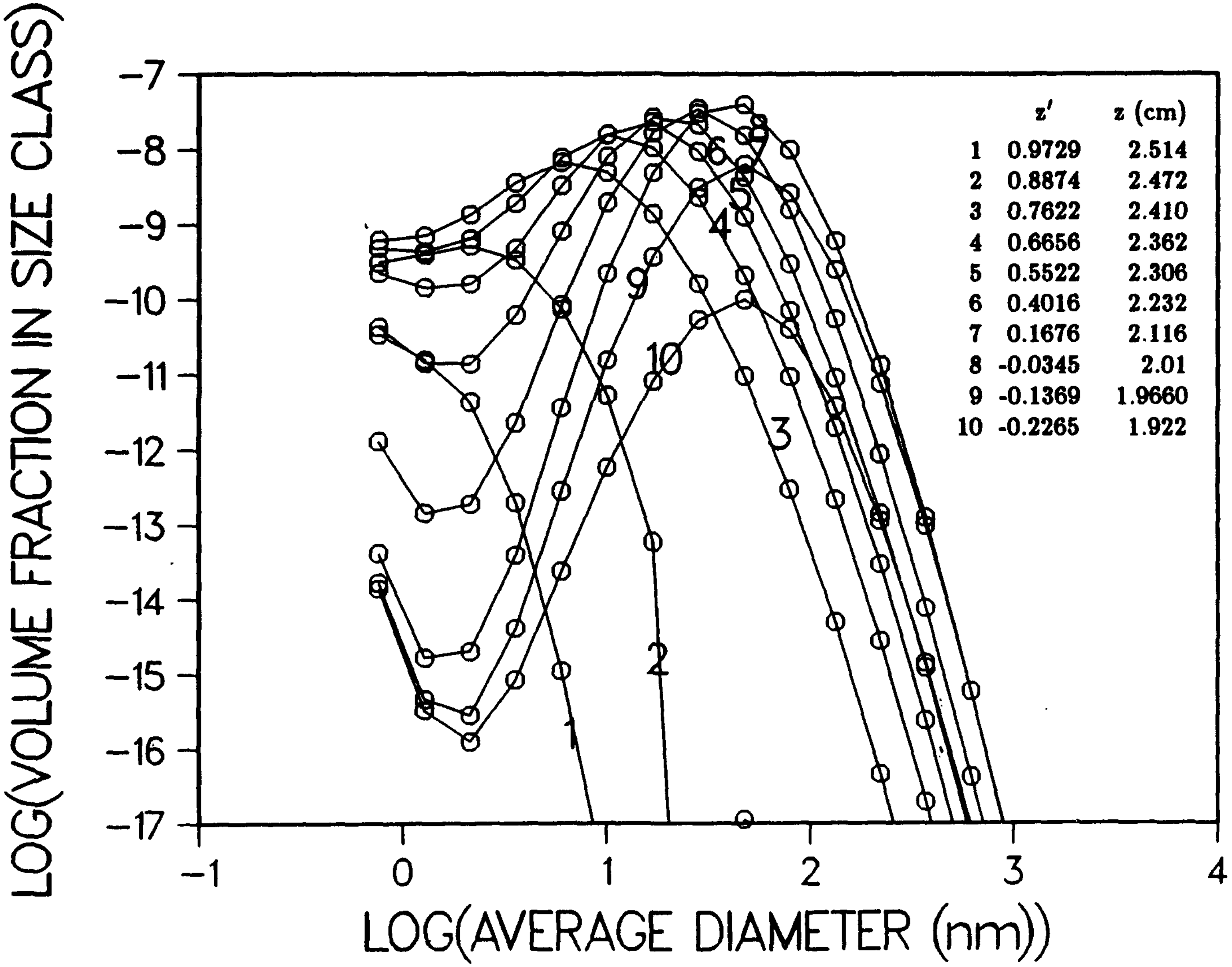

LOG(VOLUME FRACTION IN SIZE CLASS)
LOG(AVERAGE DIAMETER (nm))
−7
−8
−9
−10
−11
−12
−13
−14
−15
−16
−17
−1
0
1
2
3
4
1
2
3
4
5
6
7
8
9
10
z′ z (cm)
1 0.9729 2.514
2 0.8874 2.472
3 0.7622 2.410
4 0.6656 2.362
5 0.5522 2.306
6 0.4016 2.232
7 0.1676 2.116
8 -0.0345 2.01
9 -0.1369 1.9660
10 -0.2265 1.922

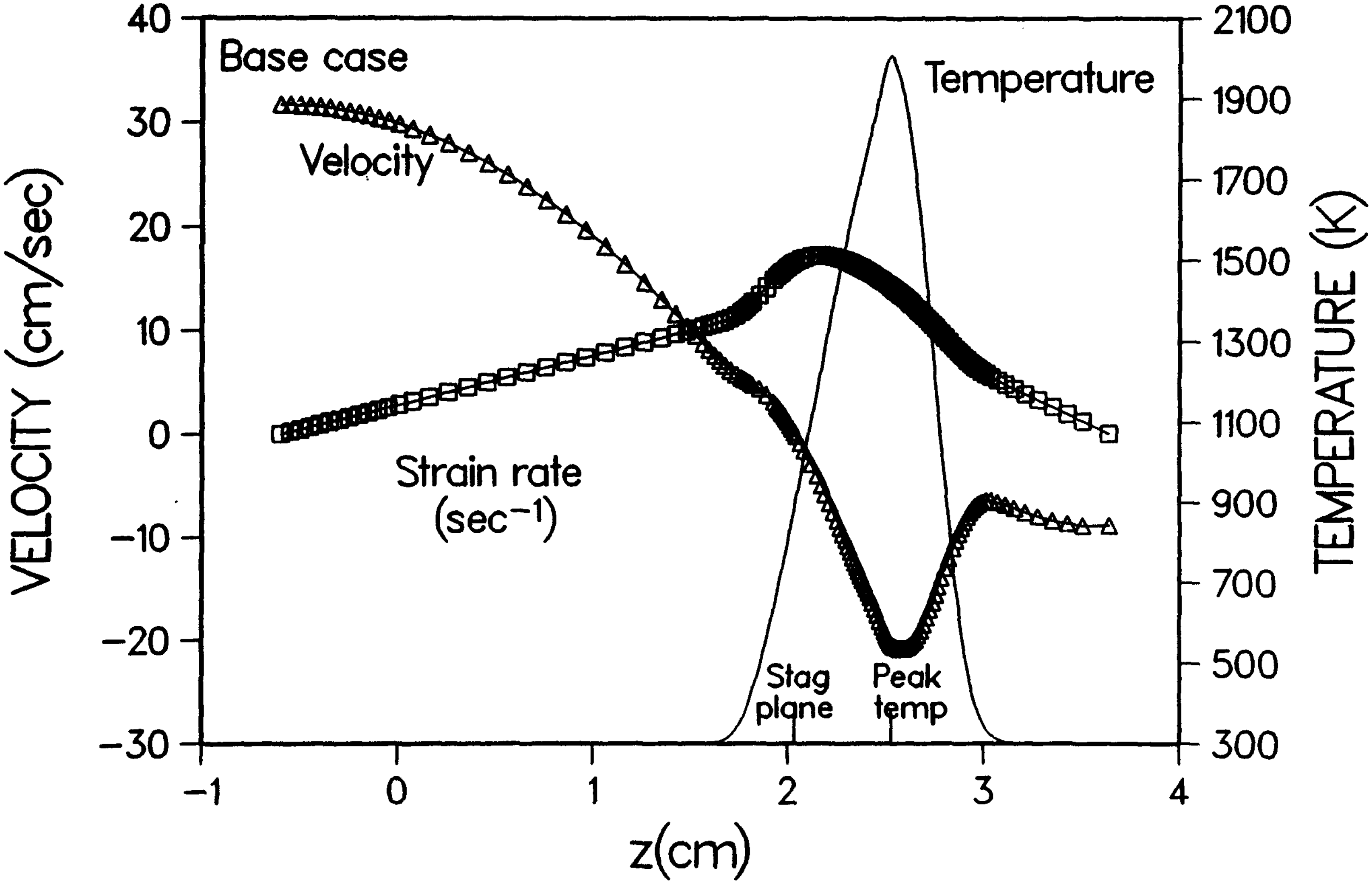
Base case
Velocity
Temperature
Strain rate
(sec^{-1})
Stag plane
Peak temp
VELOCITY (cm/sec)
40
30
20
10
0
−10
−20
−30
TEMPERATURE (K)
2100
1900
1700
1500
1300
1100
900
700
500
300
z(cm)
−1
0
1
2
3
4

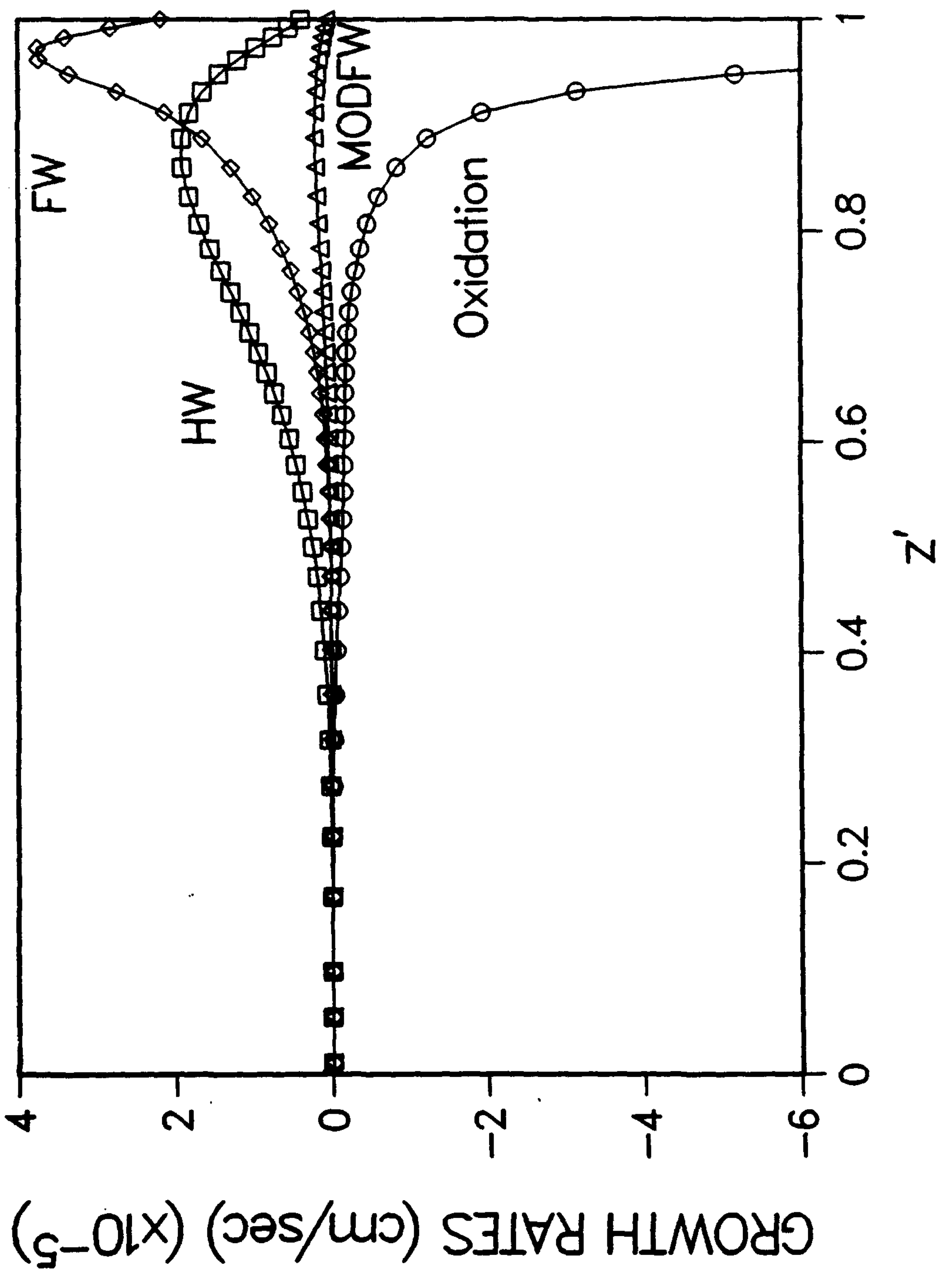
GROWTH RATES (cm/sec) (x10⁻⁵)
4
2
0
-2
-4
-6
0
0.2
0.4
0.6
0.8
1
Z'
FW
HW
MODFW
Oxidation

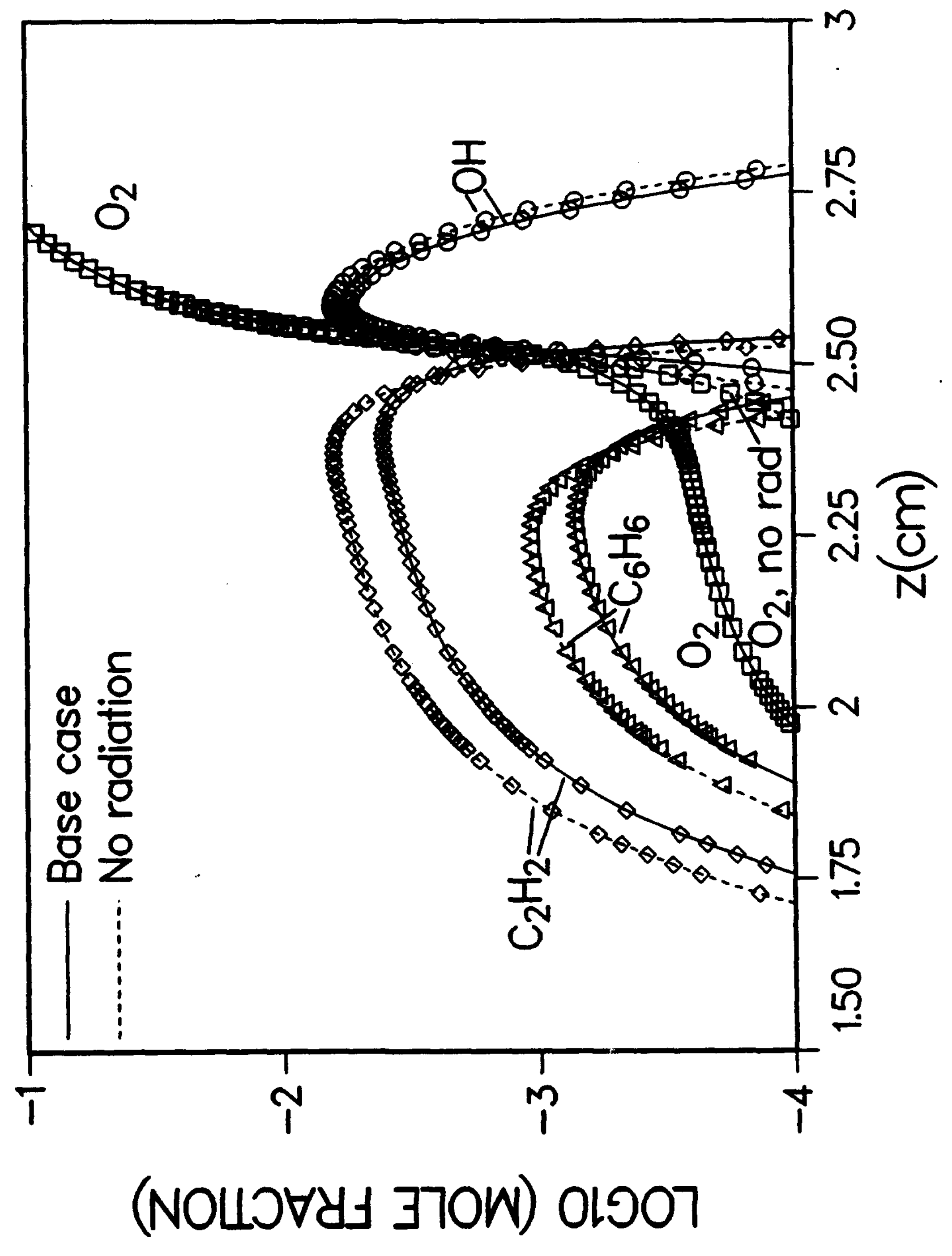

Base case
No radiation
O_2
OH
C_2H_2
C_6H_6
O_2
O_2, no rad
LOG10 (MOLE FRACTION)
-1
-2
-3
-4
z(cm)
1.50
1.75
2
2.25
2.50
2.75
3

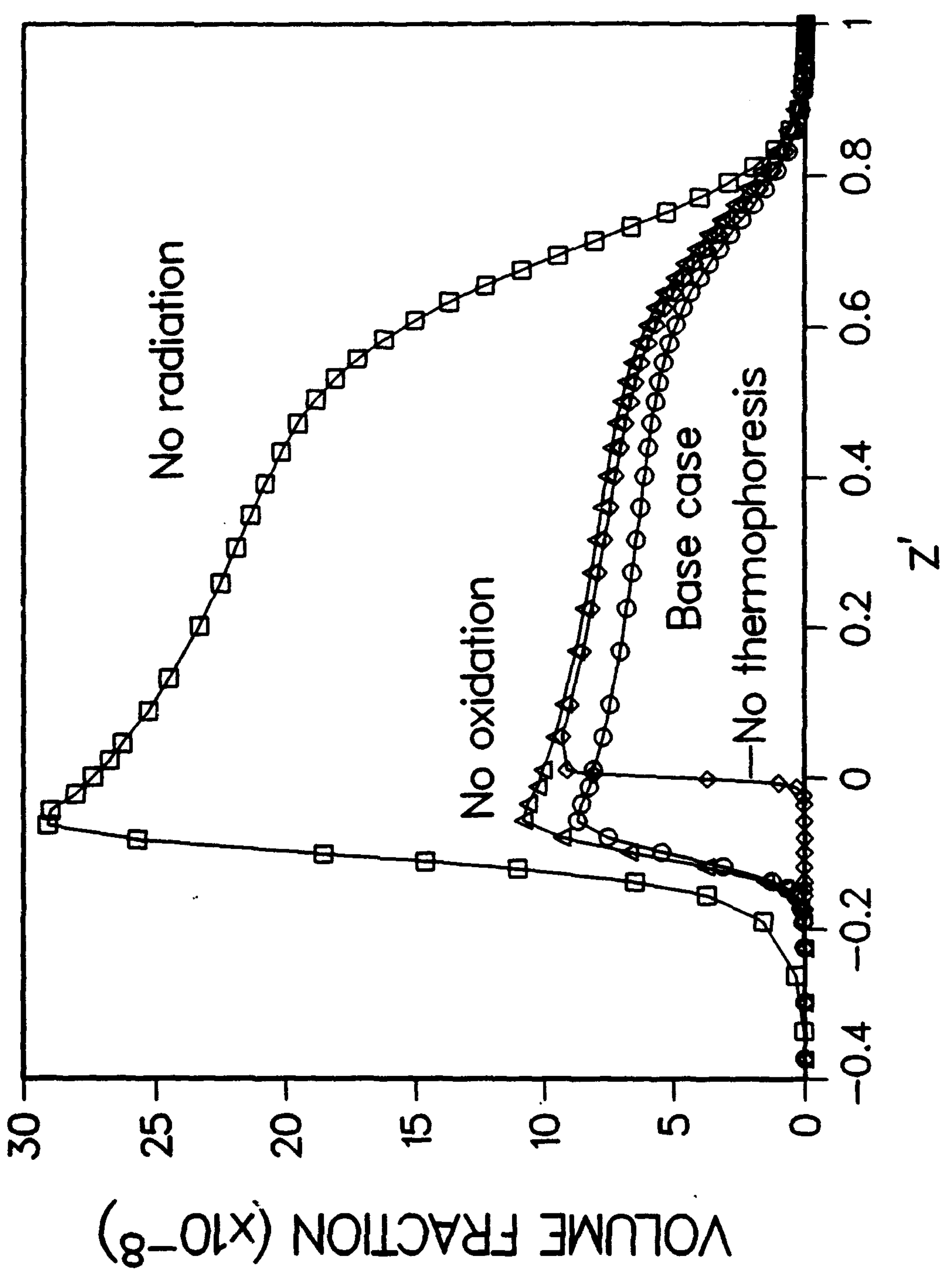

VOLUME FRACTION (x10^-8)
30
25
20
15
10
5
0
-0.4
-0.2
0
0.2
0.4
0.6
0.8
1
z'
No radiation
No oxidation
Base case
—No thermophoresis

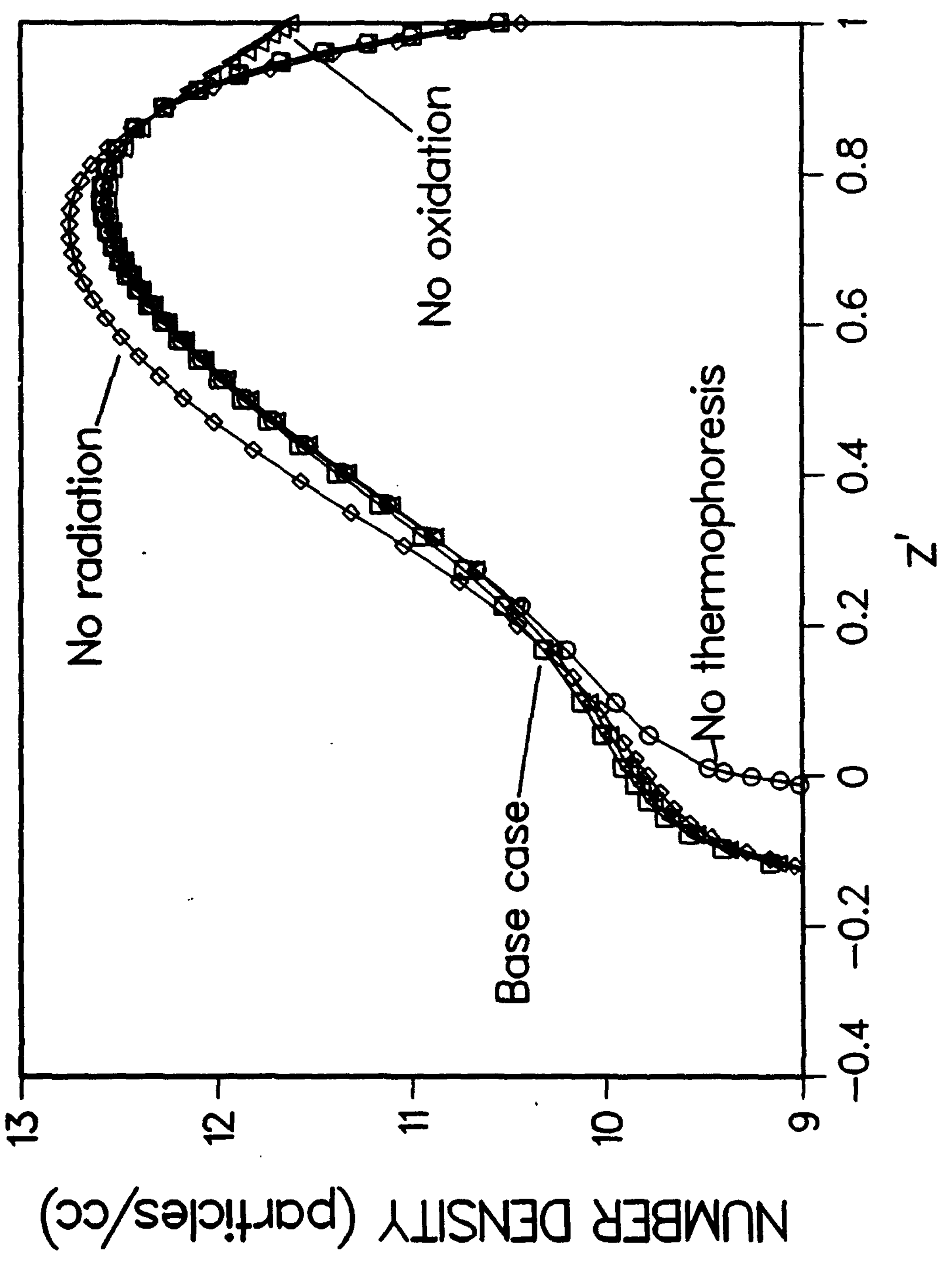
NUMBER DENSITY (particles/cc)
13
12
11
10
9
Z'
−0.4
−0.2
0
0.2
0.4
0.6
0.8
1
No radiation
No oxidation
No thermophoresis
Base case

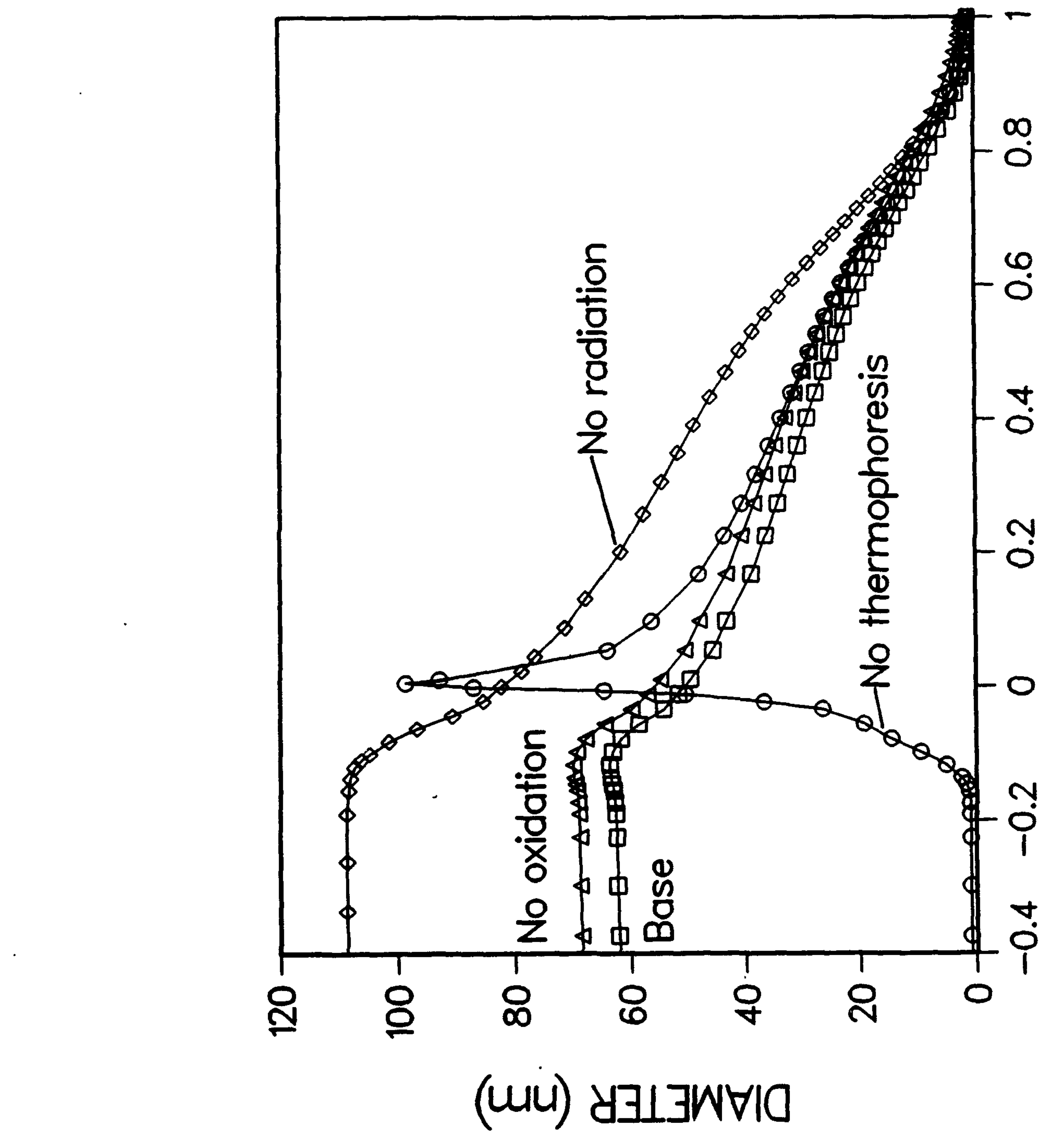
DIAMETER (nm)
120
100
80
60
40
20
0
Z'
−0.4
−0.2
0
0.2
0.4
0.6
0.8
1
No radiation
No oxidation
Base
No thermophoresis

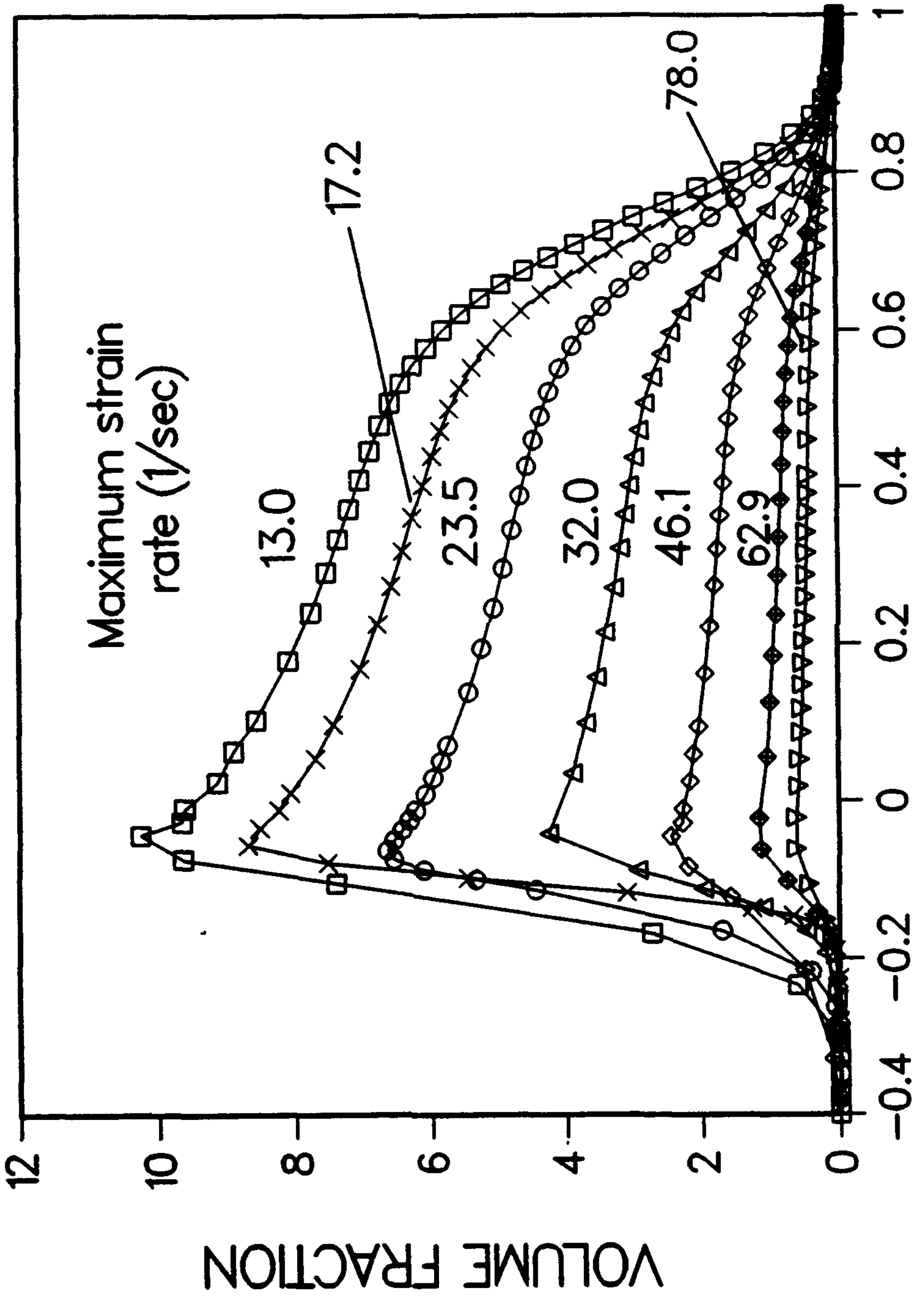
Maximum strain rate (1/sec)
13.0
17.2
23.5
32.0
46.1
62.9
78.0
VOLUME FRACTION
0
2
4
6
8
10
12
z'
-0.4
-0.2
0
0.2
0.4
0.6
0.8
1

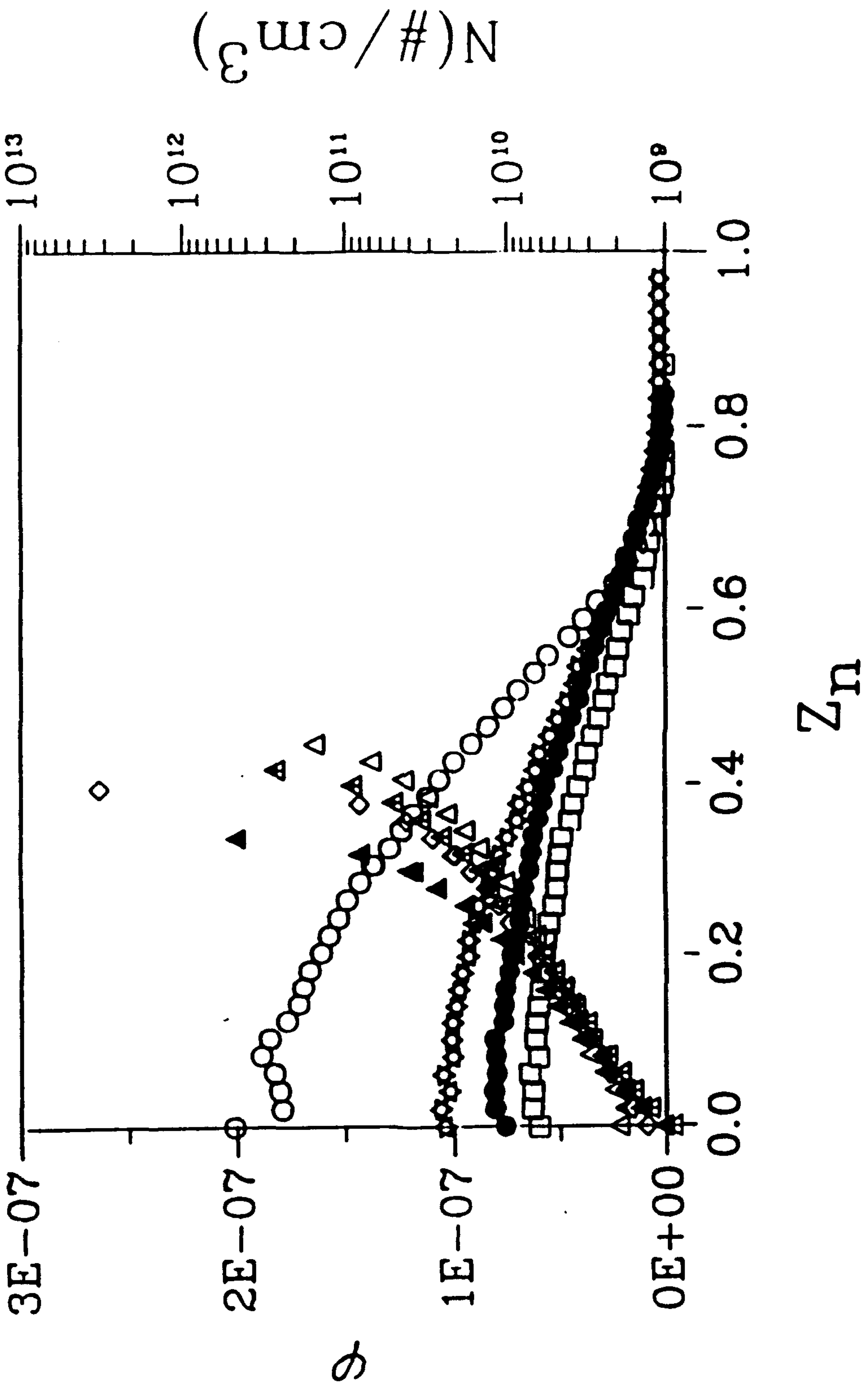
3E-07
2E-07
1E-07
0E+00
φ
0.0
0.2
0.4
0.6
0.8
1.0
Z_n
10^{13}
10^{12}
10^{11}
10^{10}
10^{9}
N(#/cm^3)

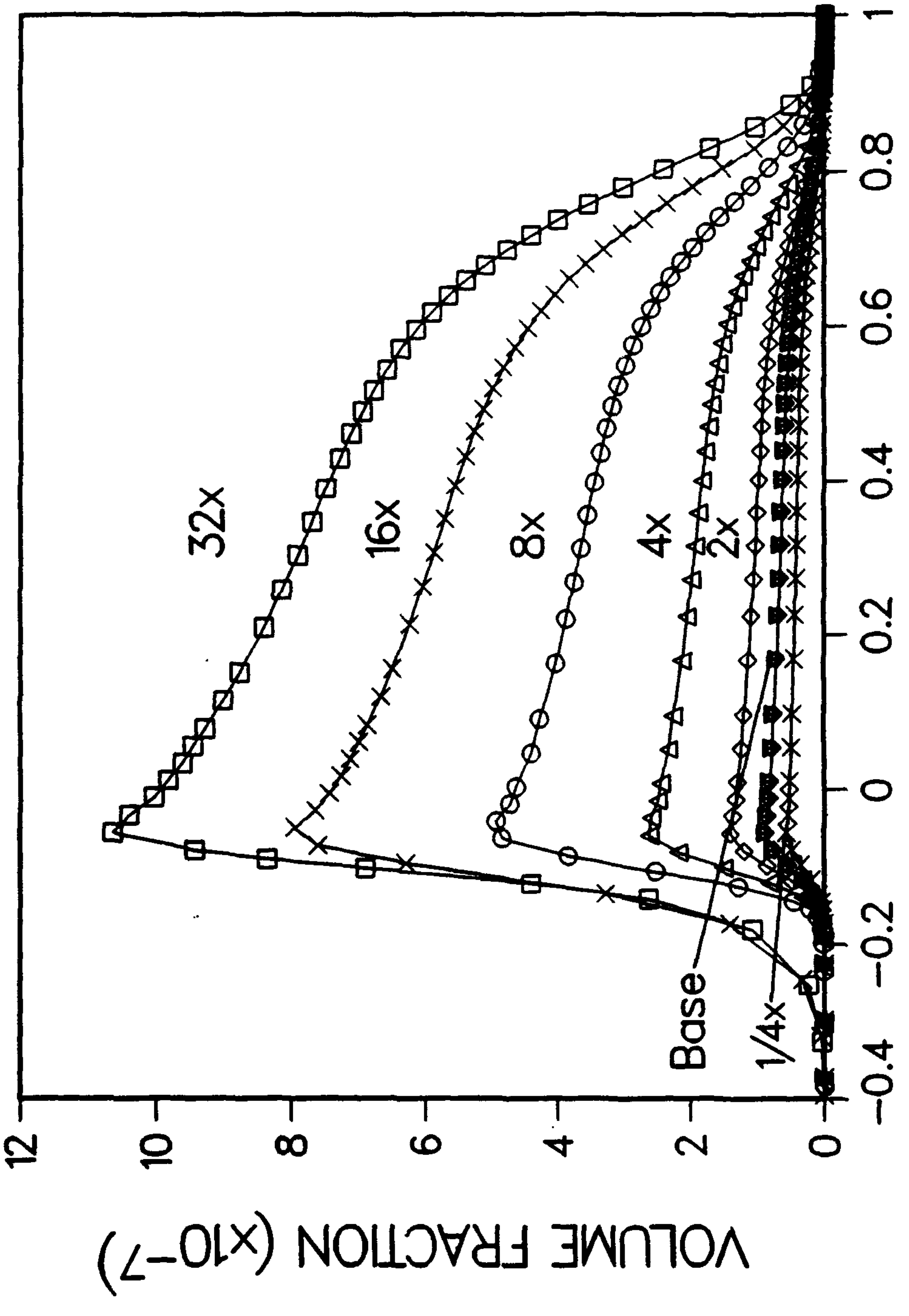
VOLUME FRACTION (x10⁻⁷)
12
10
8
6
4
2
0
z′
−0.4
−0.2
0
0.2
0.4
0.6
0.8
1
32x
16x
8x
4x
2x
Base
1/4x

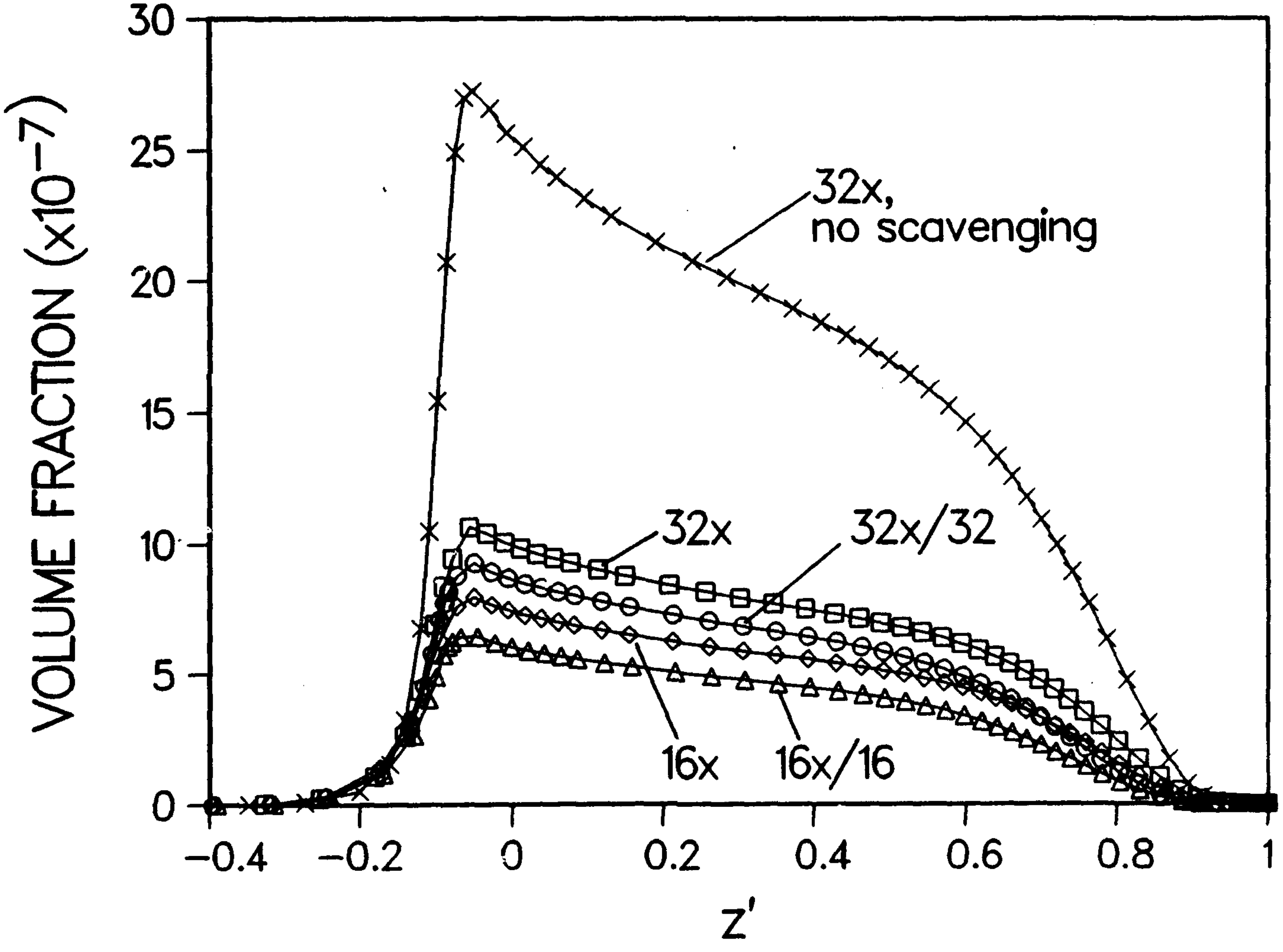
32x,
no scavenging
32x
32x/32
16x
16x/16
VOLUME FRACTION (x10⁻⁷)
0
5
10
15
20
25
30
−0.4
−0.2
0
0.2
0.4
0.6
0.8
1
z'

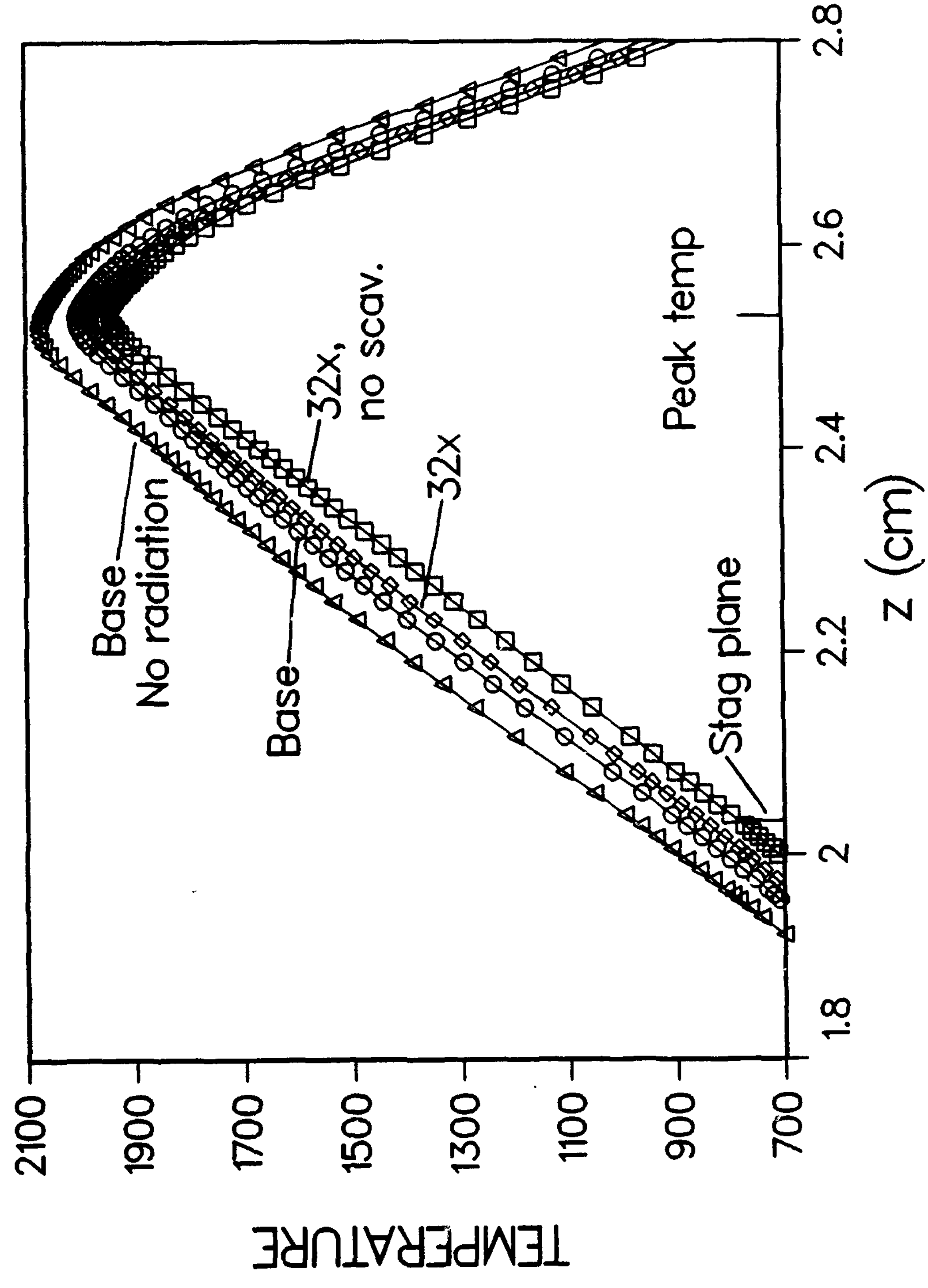
TEMPERATURE
2100
1900
1700
1500
1300
1100
900
700
1.8
2
2.2
2.4
2.6
2.8
z (cm)
Base
No radiation
Base
32x,
no scav.
32x
Peak temp
Stag plane

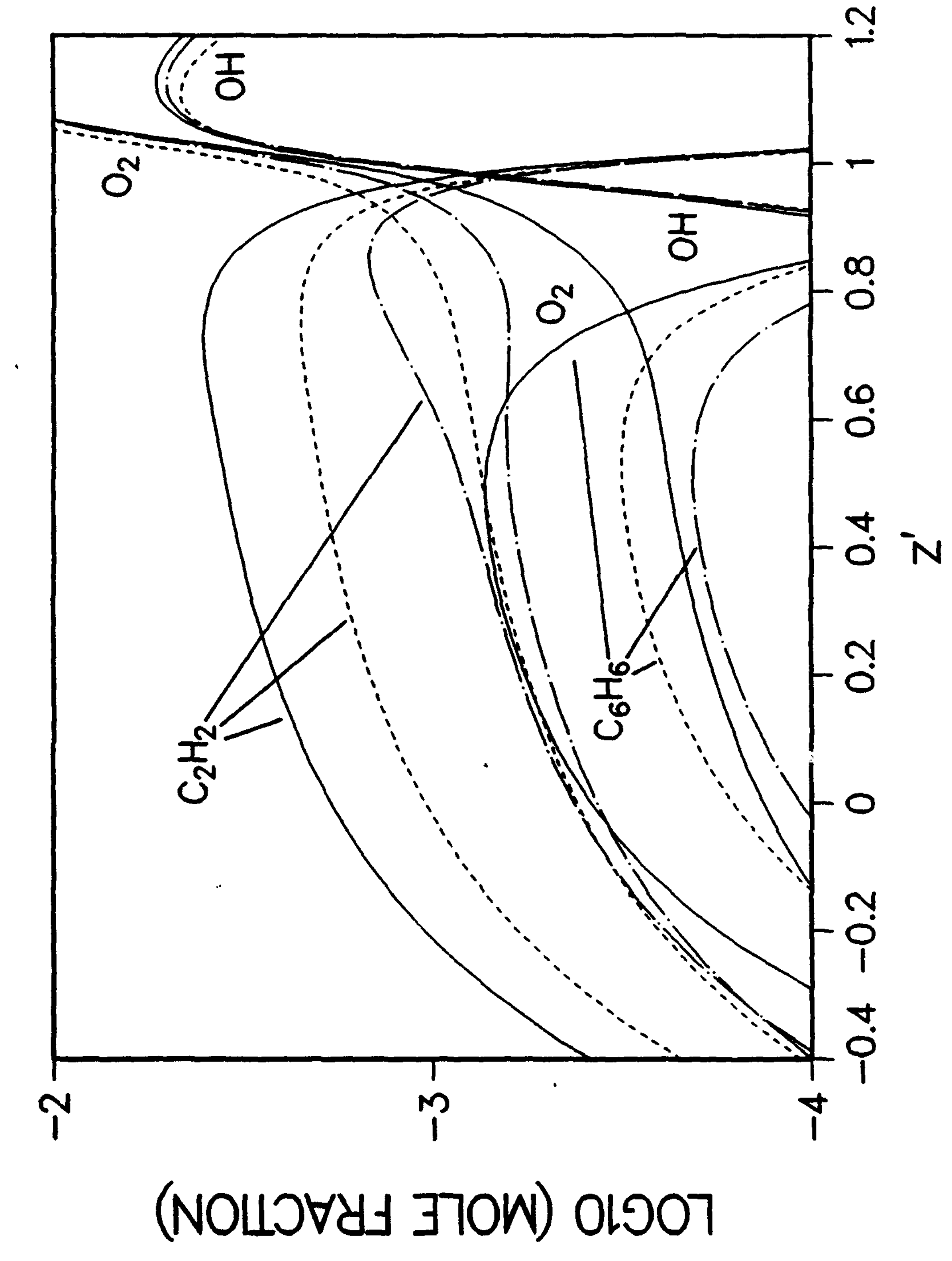

LOG10 (MOLE FRACTION)
-2
-3
-4
Z'
-0.4
-0.2
0
0.2
0.4
0.6
0.8
1
1.2
C_2H_2
C_6H_6
O_2
O_2
OH
OH

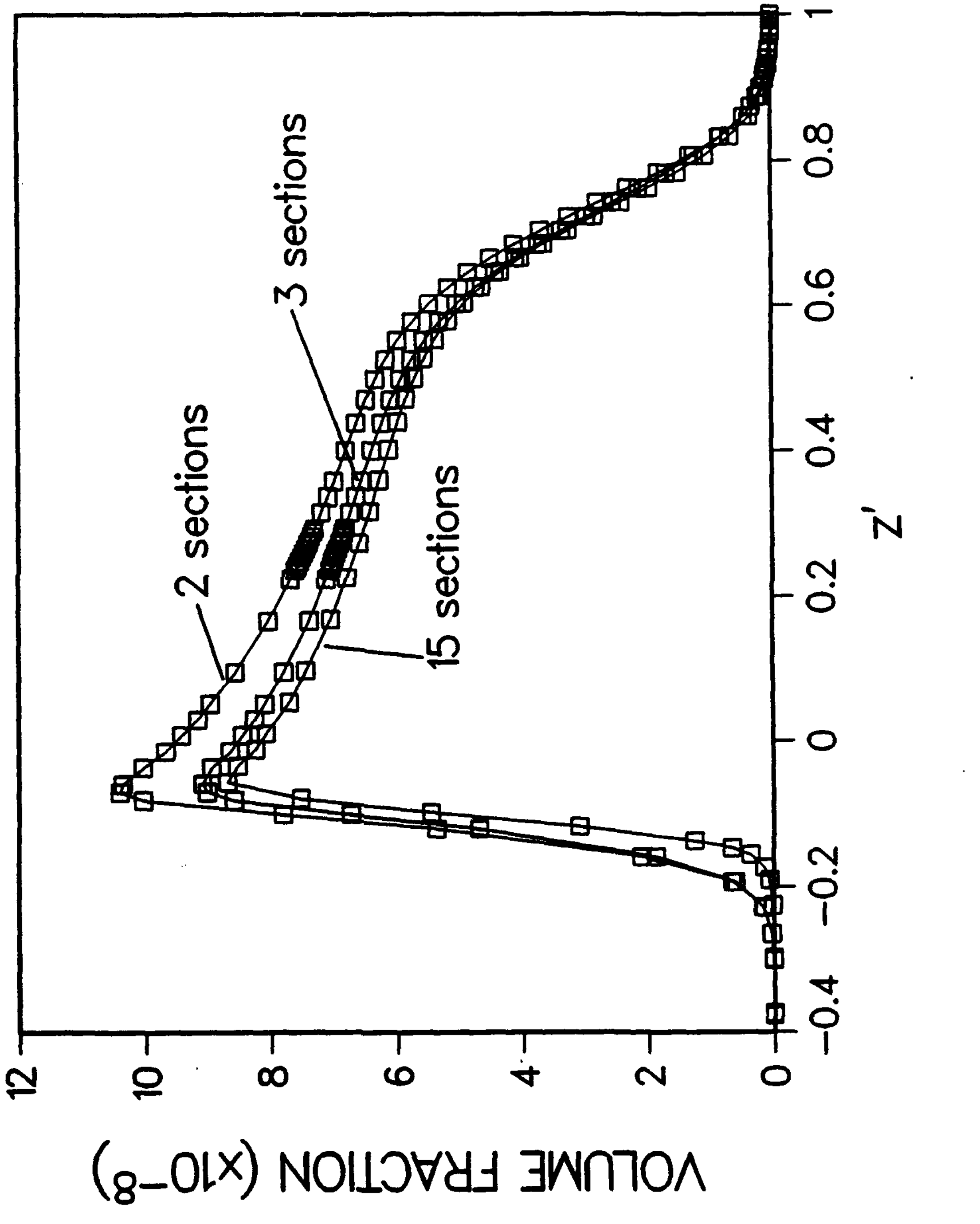
2 sections
3 sections
15 sections
VOLUME FRACTION (x10−8)
0
2
4
6
8
10
12
Z′
−0.4
−0.2
0
0.2
0.4
0.6
0.8
1

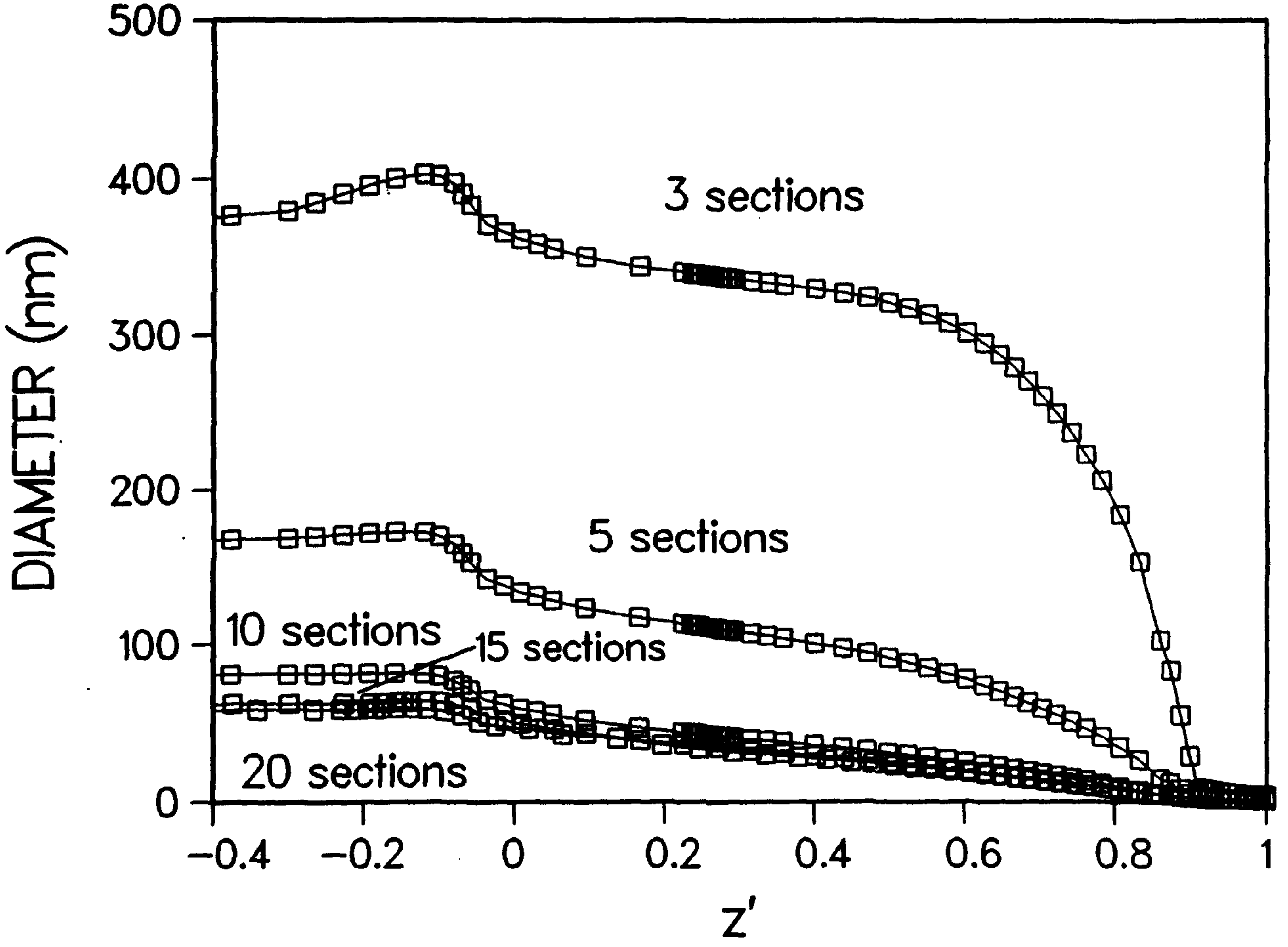
DIAMETER (nm)
500
400
300
200
100
0
−0.4
−0.2
0
0.2
0.4
0.6
0.8
1
z′
3 sections
5 sections
10 sections
15 sections
20 sections

Appendix C.
Radiative Dissipation in Planar Gas-Soot Mixtures

Pergamon

J Quant. Spectrosc. Radiat. Transfer Vol. 51, No. 4, pp. 635-644, 1994
Copyright © 1994 Elsevier Science Ltd
Printed in Great Britain. All rights reserved
0022-4073/94 $7.00 + 0.00

RADIATIVE DISSIPATION IN PLANAR GAS-SOOT MIXTURES

ROBERT J. HALL
United Technologies Research Center, East Hartford, CT 06108, U.S.A.

(Received 12 May 1993)

Abstract—A theoretical expression for the gas cooling rate (radiative dissipation) in planar mixtures of soot and combustion product gases is derived that is valid for all degrees of optical thickness. The absorption terms are reduced to numerical quadrature over the coordinate normal to the flame structure, and describe soot and gas self-absorption, as well as soot-gas spectral overlap effects. Numerical examples illustrating the effect of radiative cooling on NO production in a model, sooting, opposed jet diffusion flame are given.

INTRODUCTION

The coupling of flame radiation and flow is a subject of renewed interest, with an acceptance of the fact that reacting flow models are not complete without radiation effects. The interest goes beyond the ability to predict heat transfer to enclosure walls. It is known, for example, that substantial fractions of flame energy can be converted to radiation,[1] and that the gas cooling resulting from this non-adiabatic loss can affect flame chemistry, leading to inaccuracies in prediction of pollutants like nitric oxide. Neglect of radiation in flame hydrodynamic simulations can also lead to large errors in flow velocity and flame length. These effects are expected to be most extreme in sooting flames, but both gas and soot radiation have to be included in the most general model. Quantitative assessment of these effects requires inclusion of an energy sink term in the flow energy equation. This sink term, the divergence of the net radiative flux, is the difference of an emission term valid in the optically thin limit, and a self-absorption term that becomes important when optical thickness effects need to be accounted for. The expression for the emission term is generally trivial even when both soot and gas band radiation are present, and does not depend on flame geometry because only local properties are required. The self-absorption term is more difficult because a solution for the radiative flux is implicitly required, and integrations over all frequencies and flux propagation directions are required. This term is complicated further when both soot and gas radiators are present because of absorption profile overlaps; the broadband soot absorption and emission profile will overlap those of the relatively narrowband molecular resonances. In this paper, a complete solution for the radiative dissipation is given for the one-dimensional, plane-parallel, or boundary layer flow problem. Both gas band and soot radiation are considered, and the resulting solution is valid for all degrees of optical thickness. The theory will be illustrated by example calculations for a model, high pressure, sooting counterflow diffusion flame. Other applications might include fire radiation from smoke layers,[2] and two-dimensional, turbulent-jet diffusion flames in the boundary layer approximation.[3]

ANALYSIS

Certain aspects of this problem have been treated by other investigators.[4-6] The main features of this analysis are as follows. The absorption terms are derived by taking hemispherical averages of frequency-dependent solutions of the equation of radiative transfer, and integrating them over the absorption bandshapes of both the molecules and the soot. The soot absorption coefficient is assumed to have the Rayleigh form, with scattering ignored. For nonuniform paths, the soot terms can be derived without approximation; for the gas band terms, a form of the mean properties assumption is employed. The gas absorption profiles are assumed to have the wideband model form, and the transmissivities are appropriate to the high pressure-broadening limit. More specifically,

1. It is assumed that the molecular absorption bandshapes are described by wideband models for which the absorption profile is given by[7]

$$K_{aij}(\omega) = \frac{\alpha_{ij}\rho_i}{\Delta\omega_{ij}} \exp\left(\frac{-c_0|\omega - \omega_{ij}^{(o)}|}{\Delta\omega_{ij}}\right) \tag{1}$$

where α_{ij} is the integrated band intensity of the jth resonance of radiating species i (H_2O, CO_2, CO); ρ_i is its mass density; $\Delta\omega_{ij}$ is the bandwidth parameter of the resonance, $c_0 = 1$ for a band with an upper or lower wavenumber head at $\omega_{ij}^{(o)}$ and $c_0 = 2$ for a symmetrical band having a center at $\omega_{ij}^{(o)}$. It will further be assumed that the absorption profiles vary much more rapidly with frequency than other characteristic functions such as Planck function or soot absorption coefficient, so that

$$\begin{aligned}\int_0^\infty K_{aij}(\omega) f(\omega)\,\mathrm{d}\omega &= c_0 \int_0^\infty K_{aij}(\omega) f(\omega)\,\mathrm{d}|\omega - \omega_{ij}^{(0)}| \\ &\doteq \alpha_{ij}\rho_i f(\omega_{ij}^{(0)}).\end{aligned} \tag{2}$$

The molecular transmissivity τ is taken to have the form appropriate to the high pressure-broadening limit for which the integrated absorptance $A_{ij} = \int \mathrm{d}\omega(1 - \tau_{ij})$ has the form[8]

$$\frac{A(a_{ij})}{\Delta\omega_{ij}} = E_1(a_{ij}) + \ln(a_{ij}) + \gamma, \tag{3}$$

where

$$a_{ij} = \frac{\alpha_{ij}\rho_i}{\Delta\omega_{ij}} y,$$

y being the optical path length, E_1 the exponential integral, and γ the Euler–Mascheroni constant. Its derivative with respect to y is thus

$$\frac{\mathrm{d}A_{ij}}{\mathrm{d}y} = \Delta\omega_{ij}(1 - e^{-a_{ij}})/y. \tag{4}$$

The suitability of this approximation for combustion radiation calculations has been discussed previously.[8] It has been found to give good agreement in most cases with more elaborate calculations based on narrowband models even at one atmosphere. Many of the interesting applications will be for high pressure systems, and the approximation should be particularly good for these systems. For nonhomogeneous optical paths, evaluation of the band parameters, which appear in Eqs. (3) and (4), are based on simple, path-averaged temperature and density.[8,9] Overlaps between molecular bands are ignored, but the overlaps between the relatively narrow molecular resonances and the broadband soot absorption–emission profile are included. It will further be assumed that the transmissivity at any frequency will be given by the product of the gas and soot transmissivities, e.g. $\tau(\omega) = \tau_s(\omega)\tau_{ij}(\omega)$.

2. The soot absorption coefficient is taken to have the form appropriate to Rayleigh spheroids

$$K_{as}(\omega) = c_s \omega f_v, \tag{5}$$

where f_v is the particulate volume fraction, ω the frequency in units cm^{-1}, and the constant c_s is taken to be independent of frequency. This is equivalent to neglecting dispersion of the soot index of refraction. The Rayleigh form of the absorption coefficient is suitable to first order for aggregate chains of spheroids as well.[10] Light scattering by soot is assumed to be small.

The generalized form of the radiative source term is given by the double integral over wavelength and direction

$$\int_0^\infty \mathrm{d}\omega \int_{4\pi} \mathrm{d}\Omega K_a(\omega)[I_b(\omega) - I(\Omega, \omega)] = Q_{\mathrm{emiss}} - Q_{\mathrm{abs}} \tag{6}$$

where I_b is the Planck function, $I(\mathbf{\Omega}, \omega)$ is radiation intensity, and $K_a(\omega) = K_{as}(\omega) + \Sigma_{ij} K_{aij}(\omega)$. Consistent with the above assumptions, the first term in Eq. (6) (emission) can be simply expressed as[11,12]

$$4\pi \sum_{ij} \alpha_{ij} \rho_i I_{bij} + 4\pi c_2^{-5} c_1 \int_0^\infty \frac{u^4\, \mathrm{d}u}{\mathrm{e}^u - 1} c_s f_v T^5, \tag{7}$$

where the factorization assumption, Eq. (2), has been used for the molecular resonances *ij*, the soot index dispersion has been ignored as mentioned, and c_1 and c_2 are constants in the Planck function

$$I_b(y, \omega) = c_1 \omega^3 \bigg/ \left(\exp\left(\frac{c_2 \omega}{T(y)} \right) - 1 \right). \tag{8}$$

Thus

$$I_{bij} = c_1 (\omega_{ij}^{(0)})^3 (\exp(c_2 \omega_{ij}^{(0)}/T) - 1)^{-1} = c_1 (\omega_{ij}^{(0)})^3 \sum_{n=1}^{\infty} \exp(-n c_2 \omega_{ij}^{(0)}/T). \tag{9}$$

In the absorptive analysis, a typical molecular resonance *ij* will be assumed to simplify the notation, and a sum over all *ij* performed at the end. The radiation field solution is required as a function of frequency and flux propagation direction to calculate the self-absorption part. Referring to Fig. 1, the sum of the intensities with direction cosines μ and $-\mu$ with respect to the axis y normal to the flame structure can be formally represented as

$$I(\mu, \omega) + I(-\mu, \omega) = \int_{-\infty}^{y} I_b(y', \omega) \frac{\mathrm{d}\tau(y, y')}{\mathrm{d}(y'/\mu)} \frac{\mathrm{d}y'}{\mu} + \int_{y}^{\infty} I_b(y', \omega) \frac{-\mathrm{d}\tau(y', y)}{\mathrm{d}(y'/\mu)} \frac{\mathrm{d}y'}{\mu}, \tag{10}$$

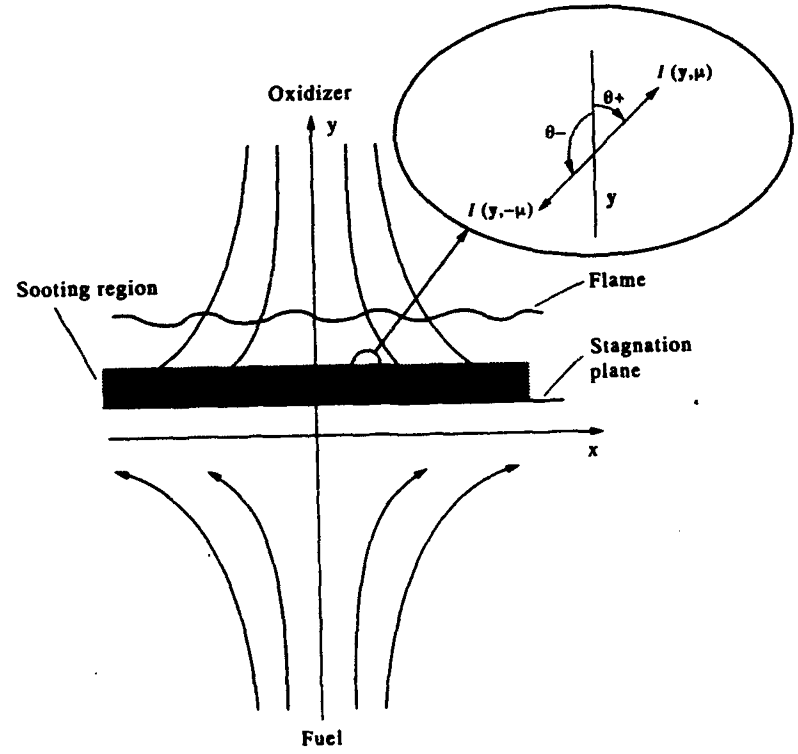

Fig. 1. Coordinate system for radiation analysis and opposed jet flame geometry. $\theta_- = \pi - \theta_+$; $\mu = \cos\theta_+$, $-\mu = \cos\theta_-$.

where

$$\tau(y, y') = \exp\left[-\int_{y'}^{y} K(y'', \omega)\frac{\mathrm{d}y''}{\mu}\right]$$

$$\tau(y', y) = \exp\left[-\int_{y}^{y'} K(y'', \omega)\frac{\mathrm{d}y''}{\mu}\right]$$

The absorption part will thus have terms proportional to $K_{aij}\tau_s(\mathrm{d}\tau_{ij}/\mathrm{d}(y'/\mu))$, $K_{aij}\tau_{ij}(\mathrm{d}\tau_s/\mathrm{d}(y'/\mu))$, $K_{as}\tau_s(\mathrm{d}\tau_{ij}/\mathrm{d}(y'/\mu))$, and $K_{as}\tau_{ij}(\mathrm{d}\tau_s/\mathrm{d}(y'/\mu))$. These represent, respectively, gas absorption of gas emission, gas absorption of soot emission, soot absorption of gas emission, and soot absorption of soot emission. Thus $Q_{abs} = Q_{gg} + Q_{gs} + Q_{sg} + Q_{ss}$. Since the gas and soot transmissivities have the form, respectively,

$$\tau_{ij}(\omega) = \exp(-\bar{K}_{aij}(\omega)|y - y'|/\mu) = \exp(-az/\mu), \tag{11}$$

and

$$\tau_s(\omega) = \exp(-c_s\omega\bar{f}_v(y; y')|y - y'|/\mu) = \exp(-b/\mu), \tag{12}$$

where

$$a = a_{ij} = \frac{\bar{\alpha}_{ij}\bar{\rho}_i}{\overline{\Delta\omega_{ij}}}|y - y'|,$$

$$z = z_{ij} = \exp(-c_0|\omega - \omega_{ij}^{(0)}|/\overline{\Delta\omega_{ij}}),$$

$$b = b_{ij} = c_s\omega_{ij}^{(0)}\bar{f}_v(y; y')(y - y'),$$

$$\bar{f}_v(y, y') = (y - y')^{-1}\int_{y'}^{y} f_v(y'')\,\mathrm{d}y'',$$

all of the terms contributing to Q_{abs} will be proportional to

$$\exp(-(az + b)/\mu). \tag{13}$$

The overbars in Eqs. (11) and (12) denote path-averaged quantities.[8,9] The contribution from all directions of propagation is given in terms of the hemispheric integrals

$$\int_{4\pi} \mathrm{d}\boldsymbol{\Omega}|I(\omega, \boldsymbol{\Omega})| = 2\pi\int_0^1 \mathrm{d}\mu\ \text{[Eq. 10]}. \tag{14}$$

Thus, the exponential integral E_1 will be a factor in all terms from the relation

$$2\pi\int_0^1 \exp(-(az + b)/\mu)\frac{\mathrm{d}\mu}{\mu} = 2\pi E_1(az + b). \tag{15}$$

The frequency integrations are generally carried out using $\int_0^\infty \mathrm{d}\omega \rightarrow (\overline{\Delta\omega}/c_0)\int_0^1 \mathrm{d}z/z$.

Starting from the assumed forms for the absorption coefficients and transmissivities, and making use of the foregoing assumptions, the following expressions for the terms contributing to the absorption part are derived.

$$Q_{gg} = 2\pi\sum_{ij}\left(\frac{\alpha\rho}{\Delta\omega}\right)_{ij}\int_{-\infty}^{\infty} \mathrm{d}y' I_{bij}(y')\overline{(\alpha\rho)}_{ij}U\left(\frac{\overline{\Delta\omega}}{\Delta\omega}, a, b\right) \tag{16}$$

$$Q_{gs} = 2\pi c_s\sum_{ij}\omega_{ij}^{(0)}\left(\frac{\alpha\rho}{\Delta\omega}\right)_{ij}\int_{-\infty}^{\infty} \mathrm{d}y' f_v(y')\overline{\Delta\omega}_{ij}(y')I_{bij}(y')U\left(\frac{\overline{\Delta\omega}}{\Delta\omega} - 1, a, b\right) \tag{17}$$

$$Q_{sg} = 2\pi c_s f_v(y)\sum_{ij}\omega_{ij}^{(0)}\int_{-\infty}^{\infty} \mathrm{d}y'\overline{\Delta\omega}_{ij}(y')I_{bij}(y')|y - y'|^{-1}[E_2(b) - E_2(a + b)] \tag{18}$$

where $a = a_{ij}$ and $b = b_{ij}$ are as given in Eqs. (11) and (12), E_2 is the exponential integral of second order, and

$$Q_{ss} = 2\pi c_s^2 c_1 f_v(y) \int_{-\infty}^{\infty} \mathrm{d}y' f_v(y') \int_0^{\infty} \mathrm{d}\omega\omega^5 \sum_{n=1}^{\infty} \mathrm{e}^{-nc_2\omega/T(y')} E_1(az(\omega) + c_s\omega\tilde{f}_v|y - y'|)$$

$$= 2\pi c_s^2 c_1 f_v(y) \frac{5!}{(c_2)^6} \int_{-\infty}^{\infty} \mathrm{d}y' f_v(y') T^6(y') \sum_{n=1}^{\infty} n^{-6}$$

$$\cdot \left[\ln\left(1 + \frac{P_n(y')}{Q(y')}\right) - \sum_{k=1}^{5} \frac{1}{k} \left(\frac{P_n(y')}{P_n(y') + Q(y')}\right)^k \right]$$

$$- 2\pi c_s^2 c_1 f_v(y) \sum_{ij} (\omega_{ij}^{(0)})^5 \int_{-\infty}^{\infty} \mathrm{d}y' f_v(y') \overline{\Delta\omega}_{ij}(y') \sum_{n'=1}^{\infty} \mathrm{e}^{-n'c_2\omega_{ij}^{(0)}/T(y')}$$

$$\cdot (E_1(a + b) - E_1(b)) \tag{19}$$

with

$$P_n(y') = nc_2/T(y')$$

$$Q(y') = c_s\tilde{f}_v|y - y'|.$$

Q_{ss} and Q_{sg} both require the integral

$$U(p, a, b) = \int_0^1 \mathrm{d}zz^p E_1(az + b). \tag{20}$$

Series expansions for this integral are given in the Appendix. The two terms for Q_{ss}, representing the pure soot absorption plus a correction for gas attenuation, respectively, are derived by setting

$$E_1(az + b) = E_1(b) + [E_1(az + b) - E_1(b)] \tag{21}$$

and assuming that

$$\int \mathrm{d}\omega[E_1(az + b) - E_1(b)] \simeq \sum_{ij} \overline{\Delta\omega}_{ij}(E_1(a + b) - E_1(b)), \tag{22}$$

where, again, a and b are as in Eqs. (11) and (12). Aside from the factorization assumption of Eq. (2), Eq. (22) is the only mathematical approximation made. It is possible to derive an exact series representation of this term for $b > a$, which confirms the validity of this approximation.

Thus all terms contributing to field absorption are expressed in semi-analytic form in terms of single integrals over the coordinate normal to the flame structure. These running integrals are, however, a computational burden. The economy of the calculation is improved by restricting attention to the strongest molecular lines (H_2O 6.3 and 2.7 micron, CO_2 4.3 and 2.7 micron, CO 2.35 micron), which account for most of the radiation. Limiting the terms in the Planck function expansion, Eq. (9), to $n = 2$ is usually an adequate approximation at high temperature as well. This type of analysis does not lend itself to inclusion of non-black wall boundary conditions. For black walls, however, additional terms in the expression for the absorption can be calculated. As an example for a single wall at temperature T_w, the following term is added to the absorption expression for the pure soot case.

$$2\pi c_1 c_s f_v(y) 4! \sum_{n=1}^{\infty} \left\{ (P_{nw} + Q_w)^{-5} - 5Q_w/P_{nw}^6 \cdot \left[\ln(1 + P_{nw}/Q_w) - \sum_{k=1}^{5} \frac{1}{k} \left(\frac{P_{nw}}{P_{nw} + Q_n}\right)^k \right] \right\}, \tag{23}$$

where

$$P_{nw} = nc_2/T_w$$

$$Q_w = c_s\tilde{f}_v|y - y_w|.$$

The net radiative flux to the wall is, for pure soot,

$$q_R = 2\pi c_s c_1 \int_{-\infty}^{y_w} dy' \int_0^{\infty} d\omega\omega^4 \sum_{n=1}^{\infty} e^{-nc_2/T(y')} E_2(c_s\omega \bar{f}_v |y' - y_w|) f_v(y')$$

$$= 2\pi c_s c_1 \int_{-\infty}^{y_w} dy' f_v(y') \sum_{n=1}^{\infty} \left\{ \frac{4!}{(P_n(y') + Q(y')^5} - \frac{5!Q(y')}{P_n(y')^6} \cdot \right.$$

$$\left. \cdot \left[\ln\left(1 + \frac{P_n(y')}{Q(y')}\right) - \sum_{k=1}^{5} \frac{1}{k} \left(\frac{P_n(y')}{P_n(y') + Q(y')}\right)^k \right] \right\} \tag{24}$$

where

$$P_n(y') = nc_2/T(y'),$$

$$Q(y') = c_s \bar{f}_v |y' - y_w|.$$

Corrections to Eqs. (23) and (24) for attenuation by gas band absorption would be derived by proceeding as in Eqs. (21) and (22), but with E_1 replaced by E_2.

The gas band contributions to net radiative wall flux may be expressed as

$$q_R = 2\pi \sum_{i,j} \int_{-\infty}^{y_v} dy' I_{bij}(y') \overline{\Delta\omega}_{ij}(y') |y_w - y'|^{-1} [E_3(b) - E_3(a + b)]. \tag{25}$$

SAMPLE CALCULATIONS

Sample calculations have been performed for a model opposed jet diffusion flame as shown in Fig. 1. The configuration consists of two opposed fuel and oxidizer jets, leading to a one-dimensional structure in a region near the stagnation streamline where application of this one-dimensional radiation analysis is appropriate. Methane fuel has been assumed, and the flame properties were calculated using a widely used opposed jet solver.[13] The flame was modified by adding the expression for the radiative source term derived here to the one-dimensional energy equation. The clean flame calculations are described in more detail in Ref. 14, where they formed the basis for a flamelet approach to predicting NO_x concentrations in an aircraft gas turbine combustor. The fuel temperature was adjusted to give a peak flame temperature approximating that of jet fuel, and the pressure of 10.5 atm is representative of such a combustor at the cruise condition. In order to assess the possible role of soot in the radiative transfer, a sooting region

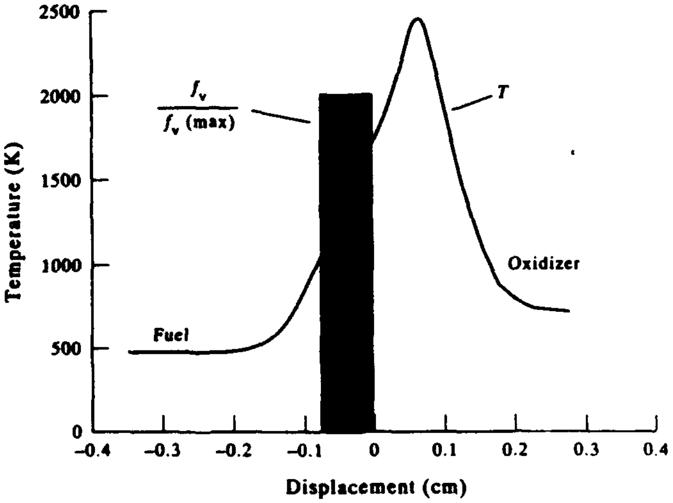

Fig. 2. Adiabatic temperature profile in model opposed jet and assumed location of sooting region. Strain rate = 20 sec^{-1}.

has been synthetically added to the clean flame solution as shown in Figs. 1 and 2. Soot will tend to form on the fuel side of the flame, and will build up at the stagnation plane due to thermophoretic transport.[15,16] Calculation of the actual soot profile, of course, requires a soot kinetics and transport model, but this was not available for this study. Thus, a simple picture of the soot profile is assumed in which it has been assumed to be uniformly distributed between the stagnation plane and a point on the fuel side where nucleation might be expected to be intense. Following Ref. 17, we assume that nucleation will occur at an elemental carbon mixture fraction of 0.1, where the adiabatic temperature is about 1675 K. This results in the soot profile located as shown in Fig. 2; the effective radiation temperature of the soot is about 1550 K, nearly 900 K lower than the peak gas temperature. The average soot volume fraction is then treated parametrically. The synthetic nature of this calculation must be emphasized; with methane fuel at this temperature the flame, in reality, would be expected to be relatively clean. The intent here is to gain some idea of the relative importance between soot and gas band radiation for reasonable ranges of the soot volume fraction. The soot is coupled to the gas flame solution only through temperature reduction resulting from the radiation; in reality, the gas cooling due to radiation could affect the pyrolysis, nucleation, and surface growth processes that grow the soot. An accurate treatment of this problem requires that temperature-dependent soot growth processes be added to the chemical kinetics mechanism. The base gas kinetics mechanism used here, where the effect of radiation on NO concentration is of interest, is a variation of that proposed by Glarborg et al.[18] The 213 reactions and 57 species of that mechanism have been culled to 126 and 30, respectively. The data set is limited to C_2 chemistry, and NO_2 kinetics have been ignored.

Opposed jet solutions are characterized by the strain rate (denoted here by the symbol a), which is a measure of the velocity gradient normal to the flame structure. It is an indication of how fast reaction products are pulled away in the direction parallel to the flame sheet. High values of strain rate correspond to short gas residence times, thinner flame structures, and somewhat lower peak temperatures, leading to reduced importance of radiation. Low values of strain rate are characterized by the opposite attributes, and it will consequently be these that are examined here. In particular, a base case value of 20 $\sec^{-1}$ is used for this study; the adiabatic temperature profile is that shown in Fig. 2. For low values of strain rate, chemical equilibrium radiating species profiles will be a reasonable approximation, and lower values of strain rate can be simulated by stretching the coordinates in proportion to $a^{-1/2}$. Figures 3 and 4 are based on fixing the adiabatic solution for $a = 20 \sec^{-1}$, stretching the coordinates in this way, and calculating the radiative dissipation according to Eqs. (7) and (16)–(19). Figure 3 shows how calculated absorption and emission vary with strain rate for a clean flame condition. It can be seen that optical thickness effects are important even for the $a = 20 \sec^{-1}$ case, where the characteristic flame thickness is about 1–2 mm. Figure 4 shows the analogous results for a sooting flame where a soot volume fraction of $10^{(-5)}$ has been assumed. At this value of volume fraction, the soot contributions start to dominate the radiation process at this pressure.

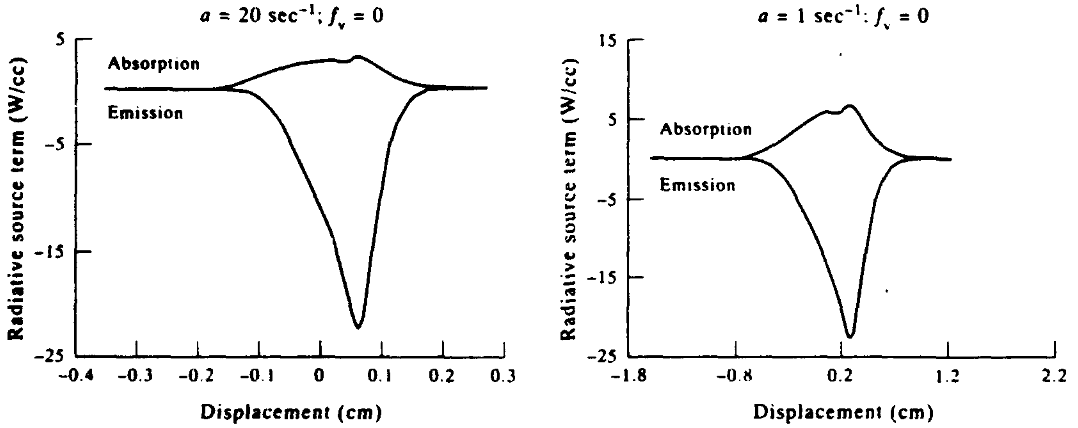

Fig. 3. Variation of radiative dissipation profiles with strain rate for non-sooting case.

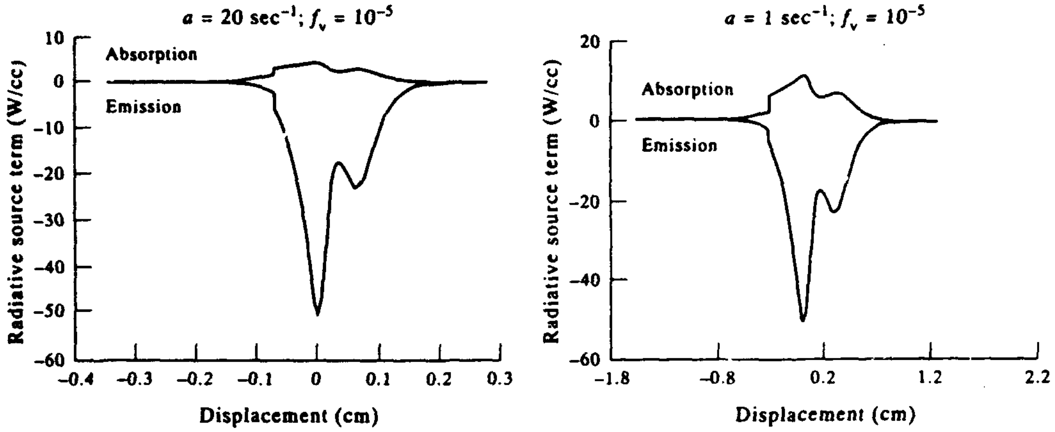

Fig. 4. Variation of radiative dissipation profiles with strain rate for soot loading of $10^{(-5)}$.

Inclusion of Eqs. (7) and (16)-(19) as a power sink term in the energy equation of the opposed jet solver leads to the predicted variation of radiative loss fraction with soot volume fraction shown in Fig. 5. As stated, soot radiation starts to dominate for volume fractions in excess of about $10^{(-5)}$, with predicted loss fractions rising to about 20% for the highest values of volume fraction that could be reasonably expected. Soot self-absorption becomes important at the highest volume fraction. Radiative loss fraction is here defined as the volume integrated net radiative power density divided by the volume integrated chemical enthalpy release rate. These curves are, of course, highly sensitive to the assumed thickness and effective radiation temperature of the soot zone. Calculations at other values of strain rate are qualitatively similar, with the overall radiative loss fraction decreasing with increasing strain rate.

The gas cooling effects resulting from the radiative loss are shown in Fig. 6. The percentage decrease in flame temperature will generally be much less than the radiative loss percentage because the heat capacity is nonlinear, and because reductions in temperature will be offset to some extent by recombination of radicals. In the case of soot radiation, the soot will be radiating from a lower temperature region, and the effect on the temperature there is shown in Fig. 6 for the maximum value of volume fraction considered. Cooling of the flame zone will then occur by thermal

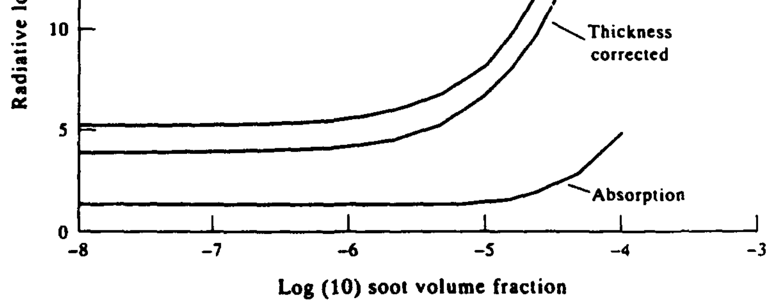

Fig. 5. Variation of predicted radiative loss fraction with soot loading for optically thin and thickness-corrected cases.

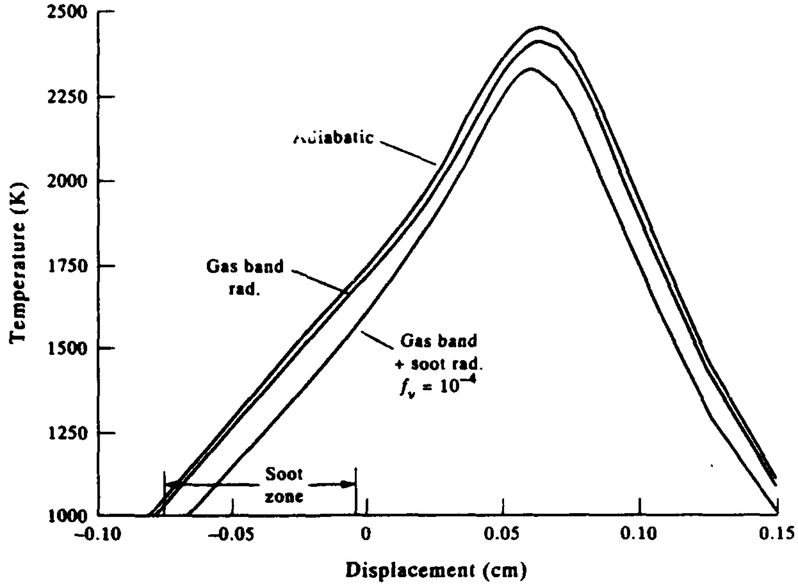

Fig. 6. Temperature profiles for adiabatic, gas band radiation, and gas band plus soot radiation.

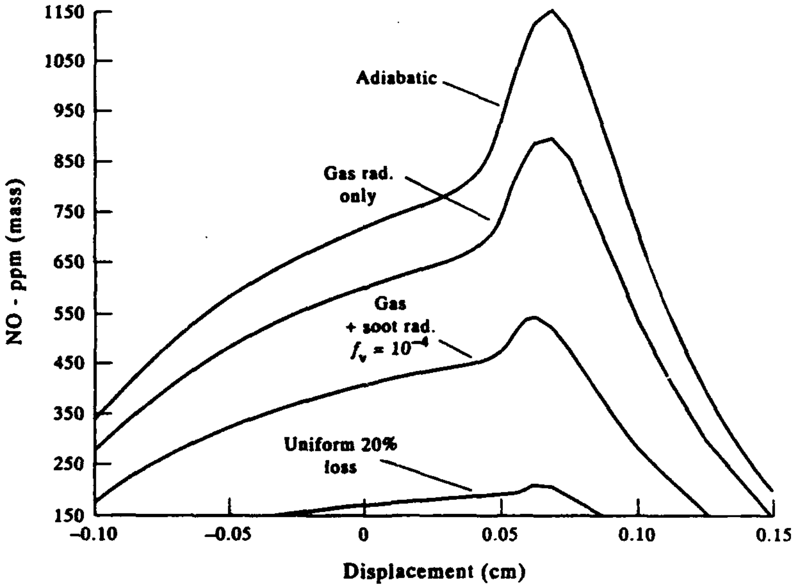

Fig. 7. Predicted effect of radiative cooling on NO profiles.

conduction; the percentage reduction in peak flame temperature is far less than the 20% radiative loss fraction for this case. As stated, however, the temperature reductions in the soot zone are probably large enough to affect the soot growth processes, leading to a complicated coupling between radiation and growth.

The effect of these temperature reductions on the profiles of NO is shown in Fig. 7. The profile resulting from the soot radiative losses can be contrasted with that resulting from assuming a local non-adiabatic loss that is everywhere 20% of the local enthalpy release rate. Because the main effect of the soot is to cool regions where the NO is not at its peak levels, soot radiation has a much smaller effect on NO reduction in these flames.

Acknowledgements—This work has been partially funded by AFOSR under Contract F49620-91-C-0056. I wish to thank K. A. Wicks and H. H. Hollick for their assistance in preparation of this manuscript.

REFERENCES

1. G. H. Markstein, "Relationship Between Smoke Point and Radiant Emission from Buoyant Turbulent and Laminar Diffusion Flames", in *Twentieth Symp. (Int) on Combustion*, The Combustion Institute, pp. 1055–1061 (1984).
2. L. Orloff, A. T. Modak, and G. H. Markstein, "Radiation from Smoke Layers", in *Seventeenth Symposium (Int) on Combustion*, The Combustion Institute, pp. 1029–1038 (1978).
3. R. K. James and D. K. Edwards, *J. Heat Transfer* **99**, 221 (1977).
4. D. K. Edwards and A. Balakrishnan, *JQSRT* **12**, 1379 (1972).
5. J. D. Felske and C. L. Tien, *J. Heat Transfer* **99**, 458 (1977).
6. S. Tabanfar and M. F. Modest, *JQSRT* **30**, 555 (1983).
7. D. K. Edwards and A. Balakrishnan, *Int. J. Heat Mass Transfer* **16**, 25 (1973).
8. A. T. Modak, "Nonluminous Radiation from Hydrocarbon-Air Diffusion Flames", Factory Mutual Rsearch Technical Report 22355-1 (1974).
9. J. D. Felske and C. L. Tien, *JQSRT* **14**, 35 (1974).
10. M. V. Berry and I. C. Percival, *Opt. Acta* **33**, 577 (1986).
11. R. J. Hall, *Appl. Opt.* **27**, 809 (1988).
12. R. J. Hall, *JQSRT* **49**, 517 (1993).
13. M. D. Smooke, I. K. Puri, and K. Seshadri, "A Comparison Between Numerical Calculations and Experimental Measurements of the Structure of a Counterflow Diffusion Flame Burning Diluted Methane in Diluted Air", *Twenty-first Symp. (Int) on Combustion*, The Combustion Institute, pp. 1783–1792 (1986).
14. A. Vranos and R. J. Hall, *Combust. Flame* **93**, 230 (1993).
15. R. L. Axelbaum, W. L. Flower, and C. K. Law, *Combust. Sci. Technol.* **61**, 51 (1988).
16. C. Zhang, A. Atreya, and K. Lee, "Sooting Structure of Methane Counterflow Diffusion Flames with Preheated Reactants and Dilution by Products of Combustion", *Twenty-fourth Symp. (Int) on Combustion*, The Combustion Institute, pp. 1049–1057 (1992).
17. I. M. Kennedy, W. Kollmann, and J. Y. Chen, *Combust. Flame* **81**, 73 (1990).
18. P. Glarborg, J. P. Miller, and R. J. Kee, *Combust. Flame* **65**, 177 (1986).
19. M. Geller, "Tables of Integrals Involving Powers, Exponentials, Logarithms, and the Exponential Integral", Cal. Tech. Jet Propulsion Lab. Report 32-469 (1963).
20. M. Abramowitz and I. Stegun (eds.), *Handbook of Mathematical Functions*, Chap. 6, 9th Edn. Dover Publications, New York, NY (1970).

APPENDIX

The integral

$$U(p,a,b) = \int_0^1 \mathrm{d}z z^p E_1(az+b) = \int_0^1 \mathrm{d}z z^p \int_1^\infty \mathrm{d}t \frac{\mathrm{e}^{(-az+b)t}}{t} \tag{A1}$$

has the following series representations:

$$\begin{aligned} \int_0^1 \mathrm{d}z z^p E_1(az+b) &= E_1(a+b)/(p+1) \qquad (p > -1) \\ &+ \begin{cases} \mathrm{e}^{-(a+b)} \sum_1^\infty \left(\frac{a}{a+b}\right)^n \frac{\alpha_{n-1}(a+b)}{(p+1)_{n+1}} & (b > a) \\ \frac{\mathrm{e}^{-1}\Gamma(p+1)\gamma^*(p+1,a)}{(p+1)} - \frac{\mathrm{e}^{-(a+b)}}{(p+1)}\left(\frac{b}{b+a}\right)\sum_1^\infty \left(\frac{a}{a+b}\right)^n \frac{\alpha_n(a+b)}{(p+1)_{n+1}} & (b < a) \end{cases} \end{aligned} \tag{A2}$$

where

$$(u)_{n+1} = \Gamma(u+n+1)/\Gamma(u)$$

$$\alpha_n(u) = n!(1+u+u^2/2!+\cdots u^n/n!)$$

and Γ and γ^* are the gamma function and a form of the usual incomplete gamma function, γ, respectively.

The first series is derived by performing the z-integration in Eq. (A1) first, using[19]

$$\int_0^1 \mathrm{d}z z^p \mathrm{e}^{-azt} = A_1(p, at, 1) = \frac{\gamma(p+1, a+1)}{(at)^{p+1}}. \tag{A3}$$

γ is now expanded in a power series,[20] and the t-integral is done term-by-term. The second series is derived by using Eq. (A3) and integration by parts, followed by term-by-term integration over t.

Appendix D.
Modeling of Soot Aerosol Formation in Opposed Jet Diffusion Flame
(abstract)

To be submitted for presentation at Fourth International Aerosol Conference, Los Angeles, August 28-September 2, 1994.

MODELING OF SOOT AEROSOL FORMATION IN OPPOSED JET DIFFUSION FLAMES. R. J. Hall, United Technologies Research Center, East Hartford, CT 06108, M. D. Smooke, Department of Mechanical Engineering, Yale University, New Haven, CT 06250, and M. B. Colket, United Technologies Research Center, East Hartford, CT 06108.

Sectional dynamical equations for spheroid growth have been coupled to conservation equations for opposed jet diffusion flames with complex chemistry and transport to provide an analytical tool for studies of soot formation. The aerosol dynamical equations use the sectional method of Gelbard and Seinfeld (1980), with inception, surface growth/oxidation, and coalescence. Particle transport by thermophoresis and diffusion is included. The free molecule regime is appropriate to atmospheric pressure flames, affording simplification of the dynamical and transport coefficients. The particulate species conservation equations are coupled to the hydrodynamic and gas-phase species conservation equations of the opposed jet or counterflow solver of Smooke, Puri, and Seshadri (1986). Particle inception is based on an expression involving calculated local concentrations of acetylene and benzene derived from complex chemical mechanisms. Surface growth occurs at a rate that is governed by temperature and local concentration of the major growth species acetylene, and likewise oxidation is governed by concentrations of oxygen and hydroxyl radical. Thermal radiation by particles and gas phase species is represented by a sink term in the hydrodynamic energy equation. Scrubbing of gas phase species by particle growth and particle thermochemistry are also treated. The result is a strongly coupled gas-particulate system. This work marks the first time that the sectional growth equations widely used in aerosol science have been coupled to the solution schemes for counterflow diffusion flames that are important in combustion science.

Comparisons of model predictions with experimental data are presented. Both theory and experiment show soot inception to occur on the fuel side of the flame, with a monotonic increase of volume fraction or suspended aerosol mass as thermophoresis and convection push the particles back in the direction of the fuel stream. Maximum volume fraction occurs theoretically at the stagnation plane, with few particles able to cross to the fuel side, as observed experimentally. Extensive parametric variations exhibiting the importance of thermal radiation, particulate scrubbing of gaseous species, thermophoresis, and oxidation will be presented.

Gelbard, F. and Seinfeld, J. H. (1980). J. Coll. Int. Sci. 78:485-501.

Smooke, M. D., Puri, I. K. and Seshadri, K. (1986). Twenty-First Symposium (International) on Combustion, The Combustion Institute, p. 1783-1792.

Research sponsored by AFOSR

Appendix E.
Predictions of Soot Formation in Counterflow Diffusion Flames
(abstract)

To be submitted for presentation at Twenty-Fifth International Symposium on Combustion, Irvine, CA, July 31-August 5, 1994.

PREDICTIONS OF SOOT FORMATION IN COUNTERFLOW DIFFUSION FLAMES. M. D. Smooke, Department of Mechanical Engineering, Yale University, New Haven, CT 06250, R. J. Hall, United Technologies Research Center, East Hartford, CT 06108, and M. B. Colket, United Technologies Research Center, East Hartford, CT 06108.

Dynamical equations for spheroid growth have been coupled to conservation equations for opposed jet diffusion flames with complex chemistry and transport to provide an analytical tool for studies of soot formation. The aerosol dynamical equations use the discrete size spectrum or sectional method of Gelbard and Seinfeld (1980), with inception, surface growth/oxidation, and coalescence. Particle transport by thermophoresis and diffusion is included in the sectional transport equation. The analysis is carried out in the free molecule regime appropriate to atmospheric pressure flames, affording simplification of the dynamical and transport coefficients. The particulate species conservation equations are coupled to the hydrodynamic and gas-phase species conservation equations in elliptic form (Smooke and Giovangigli, 1992). Particle inception is based on an expression involving calculated local concentrations of acetylene and benzene derived from complex chemical mechanisms. Various surface growth models have been evaluated, and oxidation by oxygen and hydroxyl radical is included. Optically thin thermal radiation by particles and gas phase species is represented by a sink term in the hydrodynamic energy equation. Scrubbing of gas phase species by particle growth and particle thermochemistry are also treated. The result is a strongly coupled gas-particulate system in which there can be significant perturbation of the gas phase chemistry by particulate growth and radiation.

The model predictions, which are in good qualitative agreement with methane flame experiments, show the importance of thermal radiation, particulate scrubbing of gaseous species, and thermophoresis. Parametric variations of surface growth and inception rates will be presented which provide information on the sensitivity of soot yield to these growth parameters. The sectional algorithm is shown to be highly efficient, yielding accurate soot volume fractions with as few as three sections.

Gelbard, F. and Seinfeld, J. H. (1980). J. Coll. Int. Sci. 78:485-501.

Smooke, M. D., and Giovangigli, V. (1992). Twenty-Fourth Symposium (International) on Combustion, The Combustion Institute, p. 161.

Research sponsored by AFOSR

Dist: A

REPORT DOCUMENTATION PAGE

Form Approved
OMB No. 0704-0188

Public reporting burden for this collection of information is estimated to average 1 hour per response, including the time for reviewing instructions, searching existing data sources, gathering and maintaining the data needed, and completing and reviewing the collection of information. Send comments regarding this burden estimate or any other aspect of this collection of information, including suggestions for reducing this burden, to Washington Headquarters Services, Directorate for Information Operations and Reports, 1215 Jefferson Davis Highway, Suite 1204, Arlington, VA 22202-4302, and to the Office of Management and Budget, Paperwork Reduction Project (0704-0188), Washington, DC 20503.

1. AGENCY USE ONLY (Leave blank)

2. REPORT DATE 20 July 1994

3. REPORT TYPE AND DATES COVERED Final Technical Report

4. TITLE AND SUBTITLE

Mechanistic Models of Soot Formation (U)

5. FUNDING NUMBERS

PE - 61102F
PR - 2308
SA - BS
C - F49620-91-C-0056

6. AUTHOR(S)

Meredith B. Colket, III, Robert J. Hall and
Mitchell D. Smooke

7. PERFORMING ORGANIZATION NAME(S) AND ADDRESS(ES)

United Technologies Research Center
411 Silver Lane
East Hartford, CT 06108

8. PERFORMING ORGANIZATION REPORT NUMBER

UTRC94-28

AEOSR-TR- 94 0519

9. SPONSORING/MONITORING AGENCY NAME(S) AND ADDRESS(ES)

AFOSR/NA
110 Duncan Avenue, Suite B115
Bolling AFB DC 20332- 0001

10. SPONSORING/MONITORING AGENCY REPORT NUMBER

11. SUPPLEMENTARY NOTES

12a. DISTRIBUTION/AVAILABILITY STATEMENT

Approved for public release; distribution is unlimited

A

12b. DISTRIBUTION CODE

13. ABSTRACT (Maximum 200 words)

A detailed chemical kinetic mechanism for the pyrolysis of toluene and the formation of polyaromatic hydrocarbons has been developed. This chemical kinetic model is consistent with shock tube data with mass spectral identification of intermediate species. This kinetic analysis provides a better understanding of how aromatic rings decompose and how polyaromatic species grow. In addition, a previously developed soot formation code, based on a sectional aerosol model for predicting soot inception, growth, and oxidation in a premixed flame has been fully integrated into an opposed-jet, diffusion flame code. The new code includes effects due to radiation from both gaseous species and particulates as well as scavenging of species by soot. The code treats particle transport including thermophoresis. Predictions from a low strain rate, lightly-sooting, methane-fueled, opposed-jet, diffusion flame are included in this report. Perturbation studies demonstrate the importance of fully integrating soot production, radiation, and scavenging in order to reasonably predict bulk parameters (cont'd)

14. SUBJECT TERMS soot formation modeling, chemical kinetics of toluene pyrolysis, formation mechanisms and thermodynamics of polyaromatic hydrocarbons, soot formation in opposed jet flames

15. NUMBER OF PAGES 115

16. PRICE CODE

17. SECURITY CLASSIFICATION OF REPORT	**18. SECURITY CLASSIFICATION OF THIS PAGE**	**19. SECURITY CLASSIFICATION OF ABSTRACT**	**20. LIMITATION OF ABSTRACT**
Unclassified	**Unclassified**	**Unclassified**	UL

NSN 7540-01-280-5500

Standard Form 298 (890104 Draft)
Prescribed by ANSI Std. 239-18
298-01

Abstract (Continued)

such as temperature, as well as species concentrations, sooting levels and radiation loads.

END
FILMED

DATE: 9-94

DTIC